2 mip

X-811-74-62
PREPRINT

VARIABLE-BEAMWIDTH MONOPULSE ANTENNAS

R. F. SCHMIDT

MARCH 1974

PRICES SUBJECT TO CHANGE

GODDARD SPACE FLIGHT CENTER
GREENBELT, MARYLAND

For information concerning availability
of this document contact:

Technical Information Division, Code 250
Goddard Space Flight Center
Greenbelt, Maryland 20771

(Telephone 301-982-4488)

X-811-74-62
Preprint

VARIABLE-BEAMWIDTH MONOPULSE ANTENNAS

R. F. Schmidt

March 1974

Goddard Space Flight Center
Greenbelt, Maryland

ia

VARIABLE-BEAMWIDTH MONOPULSE ANTENNAS

R. F. Schmidt
Network Engineering Division

ABSTRACT

This document discusses in detail the merits of nine methods for "zooming" microwave amplitude-sensing monopulse antenna patterns. Of these, six are directly related to the TDRSS (Tracking Data Relay Satellite System) and are compatible with a deployable-mesh pseudo-paraboloidal main reflector. The remaining three methods utilize radically different geometrical configurations that depart considerably from the TDRSS parameters existing at this time. Preservation of the monopulse postulates given by D. R. Rhodes is considered to be of prime importance for any variable-beamwidth candidate, however, it is allowed that approximate satisfaction of the postulates should be accepted for practical reasons. All of the methods discussed herein admit free choice of the polarization state, and the zooming function is never predicated on polarization. The principles underlying five of the methods discussed are frequency independent.

Exploration of the zooming techniques was carried out almost entirely by means of the Kirchhoff-Kottler vector diffraction program developed at Goddard Space Flight Center. The program generates electric and magnetic field intensity, associated phase, and time-average Poynting vector power flow in the intermediate near-field and far-field zones in both receive and transmit modes of operation. A few of the concepts have been verified experimentally with excellent agreement between theory and practice.

CONTENTS

ILLUSTRATIONS

GLOSSARY OF NOTATION

Symbol	Meaning
F, F*	focus, conjugate focus
$\sigma_{max.}$, σ_0	radial extent of reflector
λ	wavelength
f	frequency
A, C, a, c	hyperboloid and ellipsoid constants
LI	integration sampling interval in wavelengths
P(I), P(J), P(K)	components of polarization moment
$\overline{\rho}_\epsilon$	feed displacement vector $(x_\epsilon, y_\epsilon, z_\epsilon)$
N_i	feed directivity factor in $E_i = S_i \cos^{Ni} \Theta$
S_i	feed strength or weight factor
ψ_i	initial phase of source
CPU time	central processor unit time
GHz	giga-Hertz
Σ, Δ	sum and delta monopulse modes
γ_i	reflecting surface
α, β, γ	Euler angles
$\langle \overline{P} \rangle$	time-average Poynting vector
r, θ, ϕ	radial and angle variables of spherical coordinate system
ACQ	acquisition mode
TRK	tracking mode, or data mode

BW	beamwidth
Θ, Φ	angle-variables for feed system
δ, Δ	a perturbation or difference
R, r	radius or range
D, d	diameter
M	magnification factor
ϵ	eccentricity
$G_D(\theta, \phi)$	directive gain
$\bar{E}$, $\bar{H}$	electric and magnetic field vectors
A	area
a	spiral growth-rate parameter
n	spiral mode parameter
β, k	wave number designations
$F(\theta)$	spiral-pattern amplitude function
$P(\theta)$	spiral-pattern phase function
ln	natural logarithm

VARIABLE-BEAMWIDTH MONOPULSE ANTENNAS

INTRODUCTION

Antennas with highly directive gain (BW < 1°, say) are well-suited for high-precision monopulse angle-tracking, but have an inherent acquisition problem. There would be a distinct advantage to annexing a step-wise or continuously variable "zoom" capability, particularly if that capability could be achieved with the original antenna structure. Frequency is an obvious degree of freedom. For these cases where frequency cannot be changed it is necessary to look for other means, such as the reduction of the effective diameter of the main reflector aperture of the system, to increase the beamwidth of the radiation patterns. Optical "zoom" systems traditionally effect a change of focal-length to vary the field of view. Iris techniques, defocussing, and a host of other approaches have also been proposed. The present discussion is restricted to methods which (1) satisfy the monopulse postulates,[1] at least in a practical context, and (2) allow freedom of choice with regard to the system polarization state, usually circular, and specifically do not utilize polarization techniques to achieve zooming. It is implicit that an increase in beamwidth results in a reduction in directivity gain and therefore system gain. The subsequent development will show that, in general, the system gain will be reduced even further due to spillover losses, defocussing losses, circuit element losses, and other miscellaneous losses associated with zooming. Violation of the monopulse postulates will impose additional penalties at the receiver and this in turn will affect overall system performance.

This interim report is intended to illustrate some basic approaches for achieving variable beamwidth Ku-band monopulse antenna designs, but makes no attempt to optimize any of these with regard to sidelobe levels, gain, etc. The following table is provided to identify the nine geometrical configurations treated in detail, together with some of their general characteristics pertinent to the TDRSS.

CASSEGRAIN (DISPLACED HYPERBOLIC ANNULUS)

Figure 1 shows the geometry used to probe the possibilities of zooming a Cassegrain system by displacement of a hyperboloidal annulus away from a hyperboloidal cap. The objective, initially, was to obtain approximately 50% increase of beamwidth. Ideally, one would prefer to truncate the hyperboloid

[1] Ref. 1, pages 21-23 (a) angle sensing has a group inverse, (b) angle information forms as a ratio (c) the angle output function is an odd real function of the angle of wave arrival.

Geometry	Type of Zooming	Beamwidth Increase†	Mode of Operation	Ku/S-Band Dichroic Subreflector
1. Cassegrain* with Displaced Hyperbolic Annulus	discrete-step	50 to 75%	electro-mechanical	required
2. Gregorian with Truncated Ellipsoid	fixed ratio	100% with S-band 200% without S-band	electro-mechanical	not required
3. Cassegrain with** Nested Paraboloids	fixed ratio	400 to 600%	electrical	required
4. Defocussed Cassegrain* with Displaced Hyperboloid	continuously variable	100 to 300%	electro-mechanical	required
5. Conical Gregorian with Spiral Feed	discrete-step	150% (error channel)	electrical	not required
6. Dual Parabolic Cylinder	bi-directional continuously variable	nominally 100%	electro-mechanical	not required
7. Telescoping Paraboloid	continuously variable	nominally 100%	electro-mechanical	not required
8. Defocussed Cassegrain* with Displaced Feed	fixed ratio	100 to 200%	electrical	required
9. Defocussed Gregorian* with Displaced Feed	fixed ratio	100 to 200%	electrical	not required

*Frequency dependent

**This approach could also be used to satisfy a scan requirement since it is possible to gimbal the nested paraboloid.

† Upper and lower bounds have not been established for the different methods.

of an unaltered Cassegrain, but it is necessary to physically dispose of the truncated portion. In fact, the vector diffraction simulation [1] used in these studies developed a truncated approach at the outset since the displaced hyperboloidal annulus problem required a composite surface capability which was not available. The hyperboloid is regarded as a disjoint composite surface for the acquisition case, and a contiguous composite surface for the tracking case, by the program in a special subroutine.[2]

The hyperboloidal annulus was deliberately driven away from the paraboloid so that it would enter an umbral region. If, conversely, the hyperboloidal annulus were driven toward the paraboloid, an interference situation would be set up whereby portions of the annulus would tend toward phase stationarity in the aperture plane while other portions of the annulus would tend toward non-stationary results. Furthermore, this situation would change drastically as the annulus was displaced along the system (Z) axis. The question of "optimum" displacement was studied in detail with the following conclusion.

Twenty different displacements of the hyperboloidal annulus ($0\lambda \leq \delta \leq 10\lambda$) indicated that the amount of zooming was considerably less than the desired 50% increase for $0 \leq \delta \leq \lambda$, considerably greater than 50% and highly erratic for $\lambda \leq \delta \leq 3.75\lambda$, and between 40% and 70% for $3.75\ \lambda \leq \delta \leq 10\lambda$. In the latter region, the behavior was still oscillatory (±10%), but not violently so. It was also noted that the resulting radiation pattern sidelobe levels were poor in the region $\lambda \leq \delta \leq 3\lambda$, but were about -20 db in the region $3\ \lambda \leq \delta \leq 10\lambda$ with $N = 8$ in the source pattern $E = S \cos^N \Theta$, corresponding to -10 db. edge-taper on the original hyperboloid. The displacement $\delta = +4\lambda$ was chosen for subsequent studies since it was the minimum physical displacement consistent with reasonable performance (43% zooming) using a pencil beam only at this stage of the development.

Approximately 200 radiation patterns were then computed using vector Kirchhoff-Kottler diffraction theory to develop this approach to zooming the monopulse patterns. The findings are summarized as follows.

Subsystem patterns at a distance $R = F$ were computed for the normal system (unmodified hyperboloid), a truncated hyperboloid, and a displaced hyperboloidal annulus ($\delta = +4\lambda$). The normal system showed an edge taper of about -10 db, due to subsystem backscattered pattern directivity alone, directed toward the edge of the paraboloidal main reflector. The associated phase characteristic was that of a typical virtual point source at F (ψ = constant ±10 electrical degrees).

[1] Ref. 2

[2] Hyperboloid truncation is predicated on $BW = 70\ \lambda/D_e$ for the paraboloid without regard to illumination distribution initially. BW is selected, D_e is determined, and ray-optics provides the intercept on the hyperboloid.

Not surprisingly, the idealized truncated subsystem showed an edge taper of about -25 db at the paraboloid due to the backscattered pattern, but the wave front was not characteristic of a spherical wave over the region of interest, $116° \leq \Theta \leq 180°$. A nearly phase linear gradient ranging over about 300 electrical degrees was observed in the region $116° \leq \Theta$ 145° with an oscillation of ±20 electrical degrees over the region $145° \leq \Theta$ 180°. Finally, the displaced hyperboloidal annulus case showed only -15 db edge taper at the paraboloid with ±5 db oscillations over the entire range of interest. A nearly linear phase gradient ranging over about 500 electrical degrees was observed in the region $116° \leq \Theta$ 145° with an oscillation of ±30 electrical degrees over the region $145° \leq \Theta$ 180°. These diffraction results give considerable insight concerning the mechanics of zooming, and indicate a stronger dependence on phase stationarity than might be determined from ray-tracing alone.

An analysis of the Airy disc and bright-ring structure was carried out for this Cassegrain configuration. The magnification factor of the system is

$$M = \frac{\epsilon + 1}{\epsilon - 1},$$

where

$$\epsilon = [1 + (a/c)^2]^{1/2},$$

for the original set of parameters (i.e. before truncation or displacement of the hyperboloidal annulus). From a ray-tracing argument alone, under-illumination of a paraboloidal annulus should result in a smaller effective main aperture diameter and, therefore, a larger Airy disc diameter. In the event that the acquisition mode is actually attained by phase incoherence (non-stationary contributions) at the edge of the paraboloid, the conclusion is the same.

The size of the focal bright-spot or Airy disc for a paraboloid is given by

$$R_{AD} = 1.22\, F\lambda/D = 0.488\lambda$$

for a 12.5-foot diameter reflector with 5.0-foot focal length. Since the magnification factor (M) for the system is approximately equal to 2.6, by the formula above or graphically by the equivalent-parabola approach for dual-reflector systems, the Airy disc radius should be about

$$2.6\ R_{AD} = 1.27\ \lambda.$$

The vector Kirchhoff-Kottler diffraction program yielded a value of about 1.4λ for the R_{AD} of the unmodified Cassegrain configuration with the spatial divergences and illumination distributions determined by the parameters listed with Fig. 1. Truncation of the hyperboloidal annulus, the idealization for zooming by the present method, and the practical displacement of the hyperboloidal annulus by $\delta = +4\lambda$, yielded Airy disc radii of 2.25λ and 2.20λ respectively.

The implications of the preceding calculations for Airy disc size are (1) an increased requisite capture area under reception and reciprocally (2) an increased feed directivity under transmission, which is an equivalent statement. It is common knowledge that the magnification factor of dual reflectors always imposes this situation, but the further increase brought about by introduction the acquisition mode is of importance. The antenna feeds should be capable of satisfactory performance in both acquisition and tracking modes of operation.[1] It is noted that the ratio of far-field radiation pattern beamwidth and the ratio of Airy-disc radii are approximately equal for this approach to zooming,

$$\frac{BW_{(acquistion)}}{BW_{(track)}} = \frac{1.43}{1.00} \approx \frac{R_{AD(acquisition)}}{R_{AD(track)}} = \frac{2.20}{1.40} = 1.57$$

providing a crude empirical rule to feed design.

A few monopulse results are now presented from a large amount of numerically-derived data. Only the $\phi = 90°$ principal-plane data is given even though $\phi = 45°$ and $\phi = 0°$ patterns were computed and plotted for the sum (Σ) and error (Δ_1, Δ_2) channels. Main and cross-polarization components were obtained in all cases as transverse fields. The directivity of the individual source-elements of the monopulse four-cluster was set by choosing N = 8, the value used previously with pencil-beams. The feed displacements in the (conjugate) focal-plane were

$$|\bar{\rho}_\epsilon| = (|x_\epsilon|^2 + |y_\epsilon|^2)^{1/2} = \sqrt{2}\,\frac{\lambda}{4}$$

[1] A decision concerning feed efficiency must be made here. Presumably one would favor the long duration tracking or data mode over the short duration acquisition mode of operation.

where $|x_\epsilon| = |y_\epsilon|$ also. On the basis of the system magnification factor, this is not an optimum choice. Nevertheless, the zooming effect can be displayed very effectively. Monopulse feed clusters with 12 and 16 sources, variously displaced, and with different directivity (N) were used in the simulation, however, this work was not completed because of the numerous combinations that need to be explored.

Figure 2 gives the $\phi = 90°$ cut on the Σ channel (main-pol. component). Attention is directed to the constant phase of the monopulse reference channel of the angular domain $0° \leq \theta \leq 0.4°$, which is well beyond the maximum tracking angle. Now this is the reference pattern for the track mode of operation. The corresponding error channel, Δ_1, is given by Fig. 3, and again, attention is directed to the phase of that channel over the angular domain $0 \leq \theta \leq 0.4°$. It can be seen that the simulation verifies, with excellent numerical fidelity, the monopulse postulates for this amplitude-sensing system, showing a phase jump of 180 electrical degrees upon traversing the boresight axis.[1]

Figure 4 gives the $\phi = 90°$ cut on the Σ channel for the acquisition mode of operation for idealized truncation of the hyperboloidal subreflector, and Fig. 5 gives the corresponding Δ channel. Once again, it can be seen that a "clean" discontinuous 180 electrical degree phase jump exists at boresight. It should also be noted that phase is constant over the domain $0° \leq \theta \leq 0.4°$ which is the limit of tracking based upon the error channel maximum for this (idealized) set of acquisition patterns.

Figure 6 gives the $\phi = 90°$ cut on the Σ channel for the acquisition mode of operation for the more practical case with a displaced hyperboloidal annulus, and Fig. 7 gives the corresponding Δ channel. For this situation the same "clean" discontinuous 180 electrical degree phase is observed, however, the phase of the Σ and Δ channels is now constant over the angular domain $0° \leq \theta \leq 0.4°$ to within ± 5 electrical degrees or so, which is a negligible perturbation on the tracking receiver. It is not definite, at this writing, whether the ± 5 degree phase variation is artificially induced by the integration sampling interval on the main- and sub-reflector ($LI_1 = LI_2 = 0.5$ wavelengths), or an actual property of the zoomed antenna. In any event, the effect is a minor one. Further work can always be done to verify the stability of the numerical evaluation by selecting successively smaller LI intervals.

The subject of system gain is an important consideration in the selection of a beam-zooming technique. Zooming inherently implies a reduction in directivity and, therefore, system gain. In the present case, however, there is an additional loss due to spillover at the edge of the hyperboloidal cap for large physical displacements of the hyperboloidal annulus away from the paraboloid, and some defocussing loss for very small physical displacements of the annulus. For the

[1] All phases are modulo 360 electrical degrees.

set of monopulse patterns discussed in this document, first indications based on the computed monopulse sum (Σ) pattern levels indicate a loss of 6.1 db and 5.5 db for the truncated and displaced annulus cases, respectively. This can be contrasted with a 3.1 db loss predicated on a 48% beamwidth increase. The implication is that approximately 3.0 db and 2.4 db of loss is incurred by spillover and defocussing effects for the preceding idealized and practical cases respectively. It is not known whether the computed raw levels of the patterns are a reliable measure for relative (or absolute) gain determination in all cases under superposition. It is known that an integration of the secondary pattern in complete generality, leads to the correct gain figures providing the integration is carefully executed and the computed pattern is valid for large angles away from boresight. The latter integration capability is now being annexed to the programs being used for zoom calculations.

In conclusion, this first method for zooming is mechanical in nature, can achieve discrete steps of zooming by utilization of several annular hyperboloidal sections, can provide about 50% of beamwidth increase, has poor spillover characteristics (η_{SO}), and requires a dichroic hyperboloid if S-band is to coexist with Ku-band on the TDRSS.[1]

GREGORIAN (TRUNCATED ELLIPSOID)

Figure 8 shows the geometry used to probe the possibilities of zooming a Gregorian system by truncation of an ellipsoidal subreflector. The objectives, dictated primarily by TDRSS requirements, were extended to include 100% to 200% increase of beamwidth, electrical instead of mechanical means of operation, Ku-band zooming compatible with S-band tracking functions, and rapid switching between wide-angle (acquisition) and narrow-angle (tracking) modes. It has already been stated that free choice of polarization state, usually circular, was prerequisite, together with satisfaction of the monopulse postulates. Continued study of the zoom problem has resulted in more stringent objectives. Ideally the sum and difference patterns should zoom without null filling, the π-radian discontinuous phase jumps should be preserved, sidelobe characteristics should not be overly degraded, error-channel slope should exhibit monotonic characteristics, an approach to "fail-safe" design should be evolved, antenna temperature characteristics should conform to the mode of operation, and elimination of the dichroic element (for achieving S-band capability together with Ku-band zoom capability) should be considered. Finally, means should be sought to eliminate, or at least minimize, spillover loss associated with the zooming process so that system or link gain is reduced by the directivity gain factor alone if possible.

[1] Ref. 3

The logic for achieving zooming by truncation of the ellipsoidal member of a standard Gregorian configuration is elementary.[1] Ray-tracing through confocal systems results in 1:1 mappings, or isomorphisms, excepting the final m:1 mapping to the conjugate focus (F*). Under-illumination of an annulus of the main (paraboloid) reflector of a Gregorian arrangement will result in zooming. Tracing rays through the system in the receive-mode of operation truncates the subreflector in accordance with the desired amount of zooming or effective diameter postulated for the paraboloid. In this way, the focus F* becomes available for the acquisition mode, and the focus F becomes available for the track mode of operation. Compatibility with the S-band function sets constraints on the range of parameters that can be employed for the ellipsoid since an S-band tracking feed, also at focus F and nested with the Ku-band tracking feed, obscures a significant portion of the ellipsoid. The ellipsoid cannot be increased arbitrarily to relieve the situation, however, since it in turn obscures a significant portion of the paraboloid. Figure 8 represents a particular compromise in which about 3 percent of the ellipsoid and 5 percent of the paraboloid are obscured (blocked) before truncation. Obviously, with such an arrangement, wide-beam designs will reduce obscuration of the paraboloid while increasing obscuration of the ellipsoid. It is noted that some degradation of the acquisition-mode beams would probably be tolerable since the percentage of time allocated to acquisition is presumably much less than that allocated to data collection in the track-mode of operation.

The modified Gregorian configuration of Fig. 8 satisfies the objectives, discussed above, to a very high degree. It can be seen that redundant electrical switching can be provided for rapid change-over between acquisition and tracking functions. No polarization constraints are introduced to achieve zooming. Ray-optics alone essentially guarantees satisfaction of the monopulse postulates, however, this was verified by vector Kirchhoff-Kottler diffraction analysis and is discussed later in this report. It is also noted that the antenna noise temperature for the data or tracking mode will tend to be lower than for the acquisition mode since spillover from F is more apt to be directed at the cold sky, whereas spillover from F* around the subreflector is more apt to "see" the hot earth. There are, then, at least two reasons for having a high edge-taper for the acquisition feed: (1) antenna noise temperature reduction, and (2) minimization of gain loss due to truncation of the ellipsoid to achieve zooming. A dichroic subreflector is not required, even with S-band tracking functions on board since, for a Gregorian configuration, the feed points or foci are between the reflecting elements. It is necessary that the tracking feed arrangement be such as to permit energy to impinge on the ellipsoid during the acquisition phase. Retracting that feed is an obvious mechanical approach, but presents practical difficulties. Utilization of

[1] Ref. 4

feed point F also has the disadvantage of placing electronics at a large distance from the main reflector. Radiation pattern characteristics for the Ku-band zoom mode of operation as determined by the analytical/numerical Kirchoff-Kottler simulation, are now discussed in detail.

Subsystem patterns at a distance R = F were computed for the normal system (unmodified ellipsoid, $\sigma_{max.} = 1.4'$) and for a range of radii representing different-size ellipsoids and, therefore, different zooming ratios. The following discussion summarizes some of the findings. Reduction of the size of the ellipsoid resulted in progressively larger edge-taper on the main or paraboloidal reflector. An isotropic amplitude pattern ($E = S \cos^N \Theta$, $N = 0$) was used as a prime feed function, even though this is a pessimistic approach in terms of spillover (η_{SO1}) at the subreflector. It was noted that the wave backscattered from the ellipsoid was a classical virtual spherical wave with regard to both amplitude and phase at the outset for zero increase of beamwidth. As progressively smaller ellipsoidal subreflectors were introduced, the geometrical bound over which a spherical wavefront could be observed became more restricted. In the vicinity of the paraboloid limbs, the phase was no longer a constant, as for the spherical wave, but exhibited a nearly linear gradient ranging over some 1600 electrical degrees for the extreme case (truncated ellipsoid, $\sigma_{max.} = 0.4'$). The phase oscillations in the angular domain were also increased as higher zoom ratios were approached. The phase of the spherical wave associated with the unmodified system was constant to within ±20 electrical degrees over the angular domain $116° \leq \Theta \leq 180°$. These oscillations increased to ±40 electrical degrees for the extreme case of zooming cited above. The mechanics of zooming by the present method were identified as a simultaneous reduction of backscattered field strength, as predicted by ray-optics, and the introduction of phase incoherence with respect to the aperture-plane of the paraboloid. Both effects therefore tended to make an annulus of the paraboloid ineffective (an umbral region), thereby reducing the effective diameter of the main reflector and inducing the increase of beamwidth, or zooming, desired.

The Airy disc and bright-ring structure in the vicinity of the conjugate focus was not mapped, for Gregorian configuration, using the intermediate near-field capability of the program. It has been shown previously, for the Cassegrain configuration, that the effects are somewhat predictable once the magnification factor of the dual reflector system has been computed. For the Gregorian, the magnification factor is

$$M = \frac{\epsilon + 1}{\epsilon - 1},$$

where

$$\epsilon = [1 - (a/c)^2]^{1/2}$$

for the original set of parameters (i.e. before truncation of an ellipsoidal annulus.) There may be some merit to plotting the Airy diffraction structure for the zoomed case, particularly where a system is to be built and certain characteristics are to be optimized. This report was concerned with the feasibility of zooming, and first-principles only. It therefore utilized abstractions such as $N = 0$ for the prime-feed functions, etc. In addition, it was thought that it was more profitable to search for other approaches to the TDRSS zooming problem than to dwell on the optimization of any one method at this time.

The zoom phenomena for the modified Gregorian configuration was observed initially for pencil-beams (one source, $i = 1$). Uncontrolled spillover loss (η_{SOI}) exists here. Approximately 200% beamwidth increase appears attainable, however, only 100% beamwidth increase appears likely if simultaneous Ku-band and S-band operation is a condition. This situation, incidentally, leads to approximately 4% of obscuration of the paraboloid by the truncated ellipsoid, and 4% of obscuration of the truncated ellipsoid by the S-band feed. Figure 9 is a composite plot illustrating beam width for various ellipsoidal subreflectors. The beam levels are those resulting from the Kirchhoff integration, a linear superposition process. No attempt was made here to verify the integration levels with the definition of directive gain, although this feature is being annexed to the programs used for zoom-technique investigation.

In the future, an adequate number of azimuthal far-field radiation pattern cuts will be taken on each pattern so that the integral

$$G_D(\theta, \phi) = \frac{E^2(\theta, \phi)}{\frac{1}{4\pi} \iint_S E^2(\theta, \phi) \sin\theta \, d\theta \, d\phi}$$

can be evaluated meaningfully to determine directive gain. For the present, the raw integration levels are available as an estimate of relative field strength for various conditions of zooming. The implication is that the signal level changes of Fig. 9 are a measure of directivity gain loss and spillover loss at the ellipsoidal subreflector for an isotropic source at the conjugate focus (F*).

Monopulse patterns, under ideal conditions, exhibit discontinuous π-radian phase jumps at their radiation pattern amplitude nulls in the angular (θ) domain. At least this is true for those systems which have biplanar symmetry (four feeds or four groups of feeds). Certain exceptions exist. For the case at hand, commonly referred to as three-channel monopulse (Σ, Δ_1, Δ_2), the relative phase

between the sum and error channel signals is important at the detector. Figure 9 did not illustrate phase for the pencil beams, however, these curves were plotted and found to exhibit acceptable phase for satisfactory monopulse operation under zooming.

In order to demonstrate monopulse performance, by means of the simulation, two sets of patterns were computed.[1] A reference set for an unmodified Gregorian system was obtained with $\sigma_{max.} = 1.4'$ for the radius of the ellipsoidal subreflector. Figure 10 and Figure 11 give the sum and difference patterns, respectively. A wide-beam set for a modified Gregorian system was also obtained with $\sigma_{max.} = 0.74'$ for the radius of the ellipsoidal subreflector. The truncation was based on the earlier 100% beamwidth increase pencil-beam prediction. Figure 12 and Figure 13 give the sum and difference patterns, respectively, for the truncated case. Four isotropic, linearly-polarized sources were disposed symmetrically, in a conventional manner, at a radial distance $\sqrt{2}\lambda/4$ in the conjugate focal plane. The sum channel beamwidth was increased by 100 percent for monopulse operation by the preceding approach, with respect to the reference pattern, Fig. 10. Figure 10 and Figure 11 are not actual "tracking patterns" since, for an operational Gregorian system with truncated ellipsoid, the feed point F would be utilized instead of F* to illuminate the entire paraboloidal main reflector. This was simulated also, and found to produce almost identical results, when compared with Fig. 10 and Fig. 11, but is not reproduced here. The omission is deliberate since there cannot be a 1:1 correspondence between patterns derived via excitation at F and F*, and comparison is facilitated by generating the zoomed and unzoomed cases using F* only.

The computations underlying Fig. 10 through Fig. 13 were carried out principally to verify phase relationships between the sum and error channels and to demonstrate satisfaction of the monopulse postulates. It can be seen that the phase characteristics for this modified Gregorian system are excellent for monopulse operation out to the limits of track, where the error channel amplitude becomes multivalued with respect to spatial angle (θ). The slight phase gradient observed in the wide-beam computations, amounting to a total deviation of approximately 12 electrical degrees at the maximum tracking angle, is insignificant from a practical standpoint. It is possible that this gradient may have been artifically induced in the mathematical treatment since $LI_1 = 5\lambda$ and $LI_2 = 0.5\lambda$ were chosen for the integration sampling intervals on the paraboloidal and ellipsoidal reflectors, respectively. Obscuration of the main reflector by the subreflector was included in these computations.

[1] Actual measurement on a subsystem truncated for 100% and 200% zooming have been made and verify the computations of the diffraction program.

In conclusion, good noise temperature characteristics, control of spillover losses, deletion of a dichroic subreflector and approximately 100% beamwidth increase are attainable with this system, but mechanical difficulties associated with retracting the feed and placing electronics at focal point F are disadvantages.

CASSEGRAIN (NESTED PARABOLOIDS)

Figure 14 is a typical "nested paraboloid" arrangement which could conceivably be adapted to utilization on the TDRSS. The geometry was contrived so that the main paraboloid suffers a 6.4 percent obscuration by the smaller paraboloid which, in turn, is obscured in the same degree by the hyperboloidal (dichroic) subreflector. Although the support cone was originally a continuous metallic surface, it is probably feasible to employ structural members only at its base so that the radiation pattern of the acquisition feed can view the smaller paraboloid. The F/D ratio was made equal for both the acquisition and track paraboloids, but need not necessarily be set in this way. The arrangement shown in Fig. 14 could probably be achieved for the dual-mesh TDRSS reflector by adjusting the ties between the meshes. In the present application, the TDRSS link will not allow much more than 200 percent of beamwidth increase. Obscuration of the acquisition paraboloid by the hyperboloidal (dichroic) subreflector becomes increasingly important as the acquisition antenna size is reduced.

The following figures show the acquisition and tracking patterns of the nested system. In all cases, obscurations are taken into account. For the acquisition case, the hyperboloid of the Cassegrain arrangement consititutes an obscuration of the small acquisition paraboloid. The spillover of the acquisition feed is incident on the main or tracking paraboloid, and this effect is also taken into account. See Fig. 15. If there were only the obscuration due to the hyperboloid, the acquisition patterns would appear as in Fig. 16. These two figures are not greatly different, which is to be expected since the law of curvature of the main parabola (as seen from the focal point of the acquisition feed) will lead to phase incoherent contributions. In addition, these individual contributions, resolved to an LI of 2.0 (wavelengths), are weak since an edge taper of -10 db was employed for the acquisition paraboloid.

When the tracking pattern is formed, the small acquisition paraboloid acts as a boss or "deformation" of the main paraboloid. A composite surface subroutine was used here to accommodate the two parabolic laws of curvature when the antenna was used as a Cassegrain configuration. The "deformation" is, of course, partially obscured by the hyperboloid. Figure 17 shows the results for TDRSS parameters. If the small acquisition paraboloid were not present, and only the obscuration due to the hyperboloid were taken into account, the results would be as shown in Fig. 18. A few rather small effects, then, are attributable

to the disturbing influence of the acquisition antenna. Figure 17 reveals a reduction in axial gain of about 1.3 db, and a slight narrowing of the beam. The latter can be accounted for since the adverse law of curvature introduced by the acquisition antenna is effectively only a large obscuration of the central region of the main or tracking paraboloid, which leads to weak interferometric effects (i.e. beam narrowing and a 7 db increase in sidelobe levels).

In conclusion, the nested paraboloid approach is straightforward and provides a significant beamwidth increase with no gain degradation due to surface-truncation. The penalty for nesting paraboloids is a mutual degradation of the acquisition and tracking or data collection functions.

CASSEGRAIN (DEFOCUSSED HYPERBOLOID)

Figure 19 shows the geometry used to investigate monopulse zooming with the parameters of the TDRSS main reflector. The hyperboloid was displaced toward the main reflector according to a known principle,[1] which avoids increased spillover loss when zooming to wide beam operation. A continuously variable zoom ratio would appear to be obtainable via mechanical displacement of the subreflector. It was found, for the parameters used in the present simulation at least, that the zooming action is sluggish with respect to the amount of hyperboloid displacement used until one wavelength of displacement has been reached. Thereafter several hundred percent of zoom can easily be attained, but the phase relationships between the monopulse sum and difference patterns must be verified to obtain an optimum working system. In the event that the phase of the sum (Σ) channel is arbitrarily distinct from the phase of the difference (Δ_1) channel at boresight, compensation can be made. A fixed length of line at the antenna, or a phase adjustment at the monopulse receiver, will correct the situation. In the event that the phase variation with angle (θ) from boresight for the channels is given by functions $\psi_\Sigma(\theta)$ and $\psi_{\Delta_1}(\theta)$, then

$$|\psi_\Sigma(\theta) - \psi_{\Delta_1}(\theta)| = \Delta\psi(\theta)$$

must be no greater than about 30 electrical degrees since there appears to be no simple means of removing a theta-dependent phase variation.

Investigation of this defocussed Cassegrain configuration tended to show that the zooming capability was highly dependent on the directivity associated with the monopulse source elements, somewhat dependent on the source separation, and independent of the amount of hyperboloid displacement if the preceding parameters were not conducive to zooming. For example, for radial feed displacements of $\sqrt{2}\lambda/4$ in the conjugate focal plane, a directivity obtained via

[1] Ref. 5, Ref. 6

$N = 50$ in the feed function $E = S \cos^N \theta$ failed to produce beam widening of the quality desired even for displacements $Z = -10\lambda$ for the hyperboloid. A value of $N = 100$ produced good to excellent results for hyperboloid displacements as small as $\Delta Z = -3\lambda/2$ and $\Delta Z = -2\lambda$.

A separate detailed study of the subsystem with displaced hyperbola yielded some insight concerning the mechanics of zooming by the method under discussion. This study was actually motivated to improve the methods of gain calculation, which entailed computing the energy incident on the paraboloid when the hyperboloid is displaced. The reasoning was that the energy could be counted easily within the framework of the existing program by displacing the entire defocussed Cassegrain system providing a virtual spherical wave could be identified for the defocussed subsystem. It was found that such a displaced virtual spherical wave did in fact exist, for all practical purposes, and that it appeared to emanate at a point in space that was displaced toward the paraboloid. The amount of the displacement was approximately equal to the hyperboloid displacement for those cases studied. Displacement of the hyperboloid in the Cassegrain system is, therefore, equivalent to an axial displacement of a directive point source in a front-fed paraboloid. It was noted that the edge-taper at the hyperboloid limb was sensibly unaffected in achieving zooming by this method, which is indicative of the fact that phase incoherence underlies this zooming technique. This may be contrasted with the previously discussed Gregorian system which was modified by truncation of the ellipsoidal subreflector. In that approach to zooming, subsystem pattern amplitude played the dominant role.

Two sets of far-field monopulse patterns are now presented, depicting the situation when $N = 77.3$ and $N = 100$, for radial feed displacements of $\sqrt{2}\lambda/4$ in the focal plane. These correspond to feed tapers of -17 db and -20 db, respectively, at the hyperboloid edge before displacement of that subreflector. Figure 20 is the reference pattern with $N = 77.3$ and shows the sum and difference pattern amplitudes and phases. Figure 21 and Figure 22 show the same patterns when the hyperboloid has been displaced toward the main reflector by an amount $\Delta Z = -3/2\lambda$ and -2λ. It is noted that for the lower value of edge-taper (-17 db) at the hyperboloid edge, the amplitude of the difference pattern exhibits a region where the slope is monotonically increasing but close to zero ($0.25^\circ \leq \theta \leq 0.40^\circ$) when $\Delta Z = -3/2\lambda$. This is not desirable. The relative phase between sum and difference channels in Figure 21 is acceptable for acquisition. Increasing the hyperboloid displacement to -2λ, Fig. 22, results in a poor relative phase relationship between the sum and difference channels, one which is not easily compensated, and the onset of bifurcation can be observed in the sum channel. A region of undesirable error-channel slope ($0.5^\circ \leq \theta \leq 0.25^\circ$) is still in evidence, but has contracted somewhat relative to the preceding example.

The second set of patterns, obtained with increased edge-taper (-20 db) at the hyperboloid edge showed better monopulse characteristics. Figure 23 represents the reference pattern. Figure 24 and Figure 25 correspond to displacements of $\Delta Z = -3/2\lambda$ and $\Delta Z = -2\lambda$. The first of these is excellent for acquisition. There is no bifurcation of the sum pattern, the error slope is good over the domain $0° \leq \theta \leq 0.5°$, and the relative phase between the sum and error channels can be compensated by a single fixed phase-delay element. The amount of zooming or beamwidth increase, inferred from the -3db level of the sum channel is slightly in excess of 150 percent for $\Delta Z = -3/2\lambda$. Increasing the amount of hyperboloid displacement to $\Delta Z = -2\lambda$ produces approximately 275 percent of beamwidth increase of the sum channel, the error channel slope is even better than for $\Delta Z = -3\lambda/2$, but the relative phase characteristic is seriously degraded.

The gain degradation of the radiation patterns for the cases cited above is of interest in connection with the TDRSS link grain. As noted previously, a rigorous definition of directive gain is obtained by an integration of the power pattern of a directive beam over all space, in general. It is noted that the field patterns were obtained via a linear superposition of electric or magnetic fields under Kirchhoff-Kottler diffraction theory. Maxwell's equations are linear in $\vec{E}$ and $\vec{H}$. The time-average Poynting vector and other power representations are quadratic in terms of $\vec{E}$ and $\vec{H}$. Gain is a power concept, and therefore relates to the square of field values, ordinarily. It does not seem completely obvious that raw pattern levels can therefore be assumed consistent with energy conservation principles for all classes of diffraction problems, particularly the defocussed Cassegrain example being considered here. It is noted that the gain degradation, as read from the most viable solution presented, $N = 100$, $\Delta Z = -3\lambda/2$, is -8.4 db relative to the reference pattern with a beamwidth increase of 150 percent. If initial beamwidth is BW_0, then the final beamwidth $BW = BW_0 + 1.50\ BW_0 = 2.50\ BW_0$. Further, if

$$BW = \frac{70\lambda}{D}$$

were applicable here, which it is not (since nulls have been filled, and the beam characteristics for which the approximation formula usually applies are no longer present), then

$$D_{effective} = \frac{D_0}{2.5}$$

But aperture is proportional to the square of the linear dimension, so that

$$A_{effective} = \frac{A_0}{6.25}.$$

Then it would follow that this beamwidth increase results in a directive gain degradation

$$\Delta G = 10 \log_{10} \frac{A_0}{(A_0/6.25)} \approx 8.0 \text{ db.}$$

Since the computer program listings show a degradation of 8.4 db, the inference is that 0.4 db is attributable to defocus loss, over and above the intentional directivity loss incurred by wide-beam selection. In any event, the total gain degradation due to both sources should be verified by integration. It is also noted that zooming by the aberration approach can be made continuously variable (analogue) and achieves large zooming ratios, but does depart from the monopulse postulates with regard to the relative phase between the sum and error channels.

CONICAL GREGORIAN (SPIRAL FEED)

Figure 26 shows the Conical-Gregorian reflector configuration developed by the Jet Propulsion Laboratory and others, a patented concept, well-documented in the literature.[1, 2] An attempt was made to obtain zoomed monopulse operation with this geometry using a single spiral feed capable of being excited in various higher-order modes for the error-channel. Since the lowest mode of operation represents the sum channel, there appears to be no obvious means for zooming the sum channel except, possibly, via a parameter which affects the growth-rate of the spiral itself. Even this was unsuccessful, according to the simulation which assumed that the means being explored could be implemented physically. Zooming was achieved for the error channel based on the assumption that the requisite number of spiral arms for generating the higher-order error channel modes could be etched on a circuit-board and that the necessary radio-frequency switching, etc. could be accomplished.

An equiangular spiral feed was selected with fields derived from a stationary-phase analysis.[3]

$$E_\phi\Big|_{\beta r \to \infty} \approx \cos\theta (1 + j a \cos\theta)^{-1-j\, n/a} \csc\theta \tan^n \frac{\theta}{2} e^{j[n(\phi+\pi/2)-\beta r]}/\beta r$$

$$E_\theta = -\, j E_\phi$$

[1] Ref. 7
[2] Ref. 8.
[3] Ref. 9.

From the preceding it can be shown that, concerning the θ dependence alone, the magnitude and phase of E_ϕ are given by

$$|F(\theta)| = \frac{\cos\theta \tan^n\left(\frac{\theta}{2}\right) e^{n/a \tan^{-1} a\sin\theta}}{(1 + a^2 \sin^2\theta)^{1/2} \sin\theta}$$

and

$$P(\theta) = \tan^{-1} a \sin\theta + \frac{n}{2a} \ln(1 + a^2 \sin^2\theta),$$

respectively.

Ordinary monopulse operation with such a driving function is then achieved by simultaneously exciting the sum mode (n = 1) and a higher-order mode (n > 1). Both sum (Σ) and error channel (Δ) modes have amplitudes which are axially symmetric (ϕ independent). Their phase characteristics are distinct linear functions of the azimuthal angle (ϕ), however, so that the phase difference between Σ and Δ channels is unique for each value of ϕ. In this way the azimuthal coordinate is resolved in a tracking application. The remaining polar coordinate (θ) is resolved by means of the ratio of the error and sum channel magnitudes. The magnitude of the sum channel is also utilized for telemetry data collection and target illumination in a radar application. It can be seen that the field equations, above, depict an almost circular polarization state.

Intuitively, it would appear that satisfactory monopulse operation with a feed such as the equiangular spiral antenna could be used with front-fed paraboloids, Cassegrain, Gregorian, and other reflector configurations. In particular, the Conical-Gregorian arrangement should also succeed. The properties of the latter geometry and the equiangular spiral can now be combined to achieve zooming of the rotationally symmetric error-channel pattern (Δ). It can be shown via the field equations of the spiral feed that the Δ patterns tend to be asymptotic to an angular bound away from the system axis and, as n increases, the radiation is crowded toward this bound. That is, a solid-angle in the vicinity of the axis contributes less and less energy as higher-order modes are selected. This implies that the central region of the subreflector would also be weakly illuminated for higher-order Δ modes if the spiral source were used with a Conical-Gregorian configuration.

Since one of the unique properties of that reflector arrangement is that central illumination is mapped under ray optics to the peripheral regions of the main reflector, it follows that beam broadening should occur for the larger

values of n associated with the spiral source antenna. That is, the effective diameter of the conical main reflector is reduced to achieve an acquisition beam. It is noted in passing that the singular ray which is directed along the system axis and intersects the subreflector maps to a circle, the outermost rim of the main reflector. The tangents, and therefore normals, of the subreflector are discontinuous at the "vertex" of that surface. Unlike conventional Cassegrain and Gregorian systems, the system of rays between surfaces no longer comprises an isomorphism or 1:1 mapping. From a practical point of view this is of little consequence since energy is not associated with rays, but only ray bundles, and since the final evaluation of the idea was by means of Kirchoff-Kottler diffraction theory which utilizes areas instead of rays.

The idea of zooming the monopulse error-channel by means of a Conical-Gregorian configuration in combination with a single spiral feed, or source, was conceived entirely by ray optics. It turns out that diffraction theory bears out the ray-optics arguments. Figure 27 depicts the primary difference patterns derived from a spiral feed, and illustrates how energy is concentrated near a conical bound as higher-order modes are generated. Figure 28 shows the Σ and Λ tracking patterns, and Figure 29 shows the acquisition Λ pattern. The same sum pattern is to be inferred for Figure 29 since dual-channel or spiral monopulse requires a reference beam to resolve the azimuthal angle (ϕ) and to obtain in the acquisition mode (and a means to illuminate a target in radar applications).

It was thought that the sum pattern beamwidth could be varied by utilizing the spiral parameter (a) which affects spiral growth rate and yields wider primary beams for higher values of (a). Due to the fact that edge taper on the subreflector of the Conical-Gregorian system does not map through as edge taper on the main reflector, and also the fact that the central region is always illuminated in the sum mode, a ray-optics prognosis indicates that success is unlikely. Small (a) implies a good tracking situation, but tends to create an illumination distribution on the main reflector that enhances an already severe interferometer effect. That is, the central region of the main reflector has already been sacrificed due to obscuration by the subreflector. Concentrating sum-mode energy toward the central region of the subreflector causes the significant current distribution values to crowd toward the periphery of the main reflector. The Kirchhoff-Kottler diffraction theory was used to simulate the sum-channel beam for various values of parameter (a). The sum pattern did not broaden, apparently because insufficient energy was directed toward the edge of the subreflector ($\theta_{max.} = 34°$).

In conclusion, this approach was only partially successful since a satisfactory technique for broadening the sum-channel pattern was not found. The approach is unique because it utilizes a geometry which interchanges edge and central

illumination distributions between the main reflector and subreflector, and is therefore distinct from conventional Cassegrain and Gregorian systems.

TELESCOPING DUAL PARABOLIC CYLINDERS

Figure 30 shows a geometry which is capable of independent continuously-variable monopulse zooming in orthogonal planes by mechanical means. The geometry is well-known, but this author has not found any evidence that it has been adapted to either monopulse or zooming.[1] An interesting alternative combination consisting of a parabolic cylinder and hyperbolic cylinder has been found, and appears to be useful for monopulse zooming applications also, but was not examined in detail.[2] The configuration studied in this report is apparently covered by a patent.[3] Most of the work done at Goddard Space Flight Center on the dual parabolic cylinder antenna was carried out for multibeam application, and is discussed in an X-Document.[4] The present report addresses only the monopulse and zooming aspects of the dual parabolic cylinder problem.[5]

A brief review of basic principles leading up to the arrangement given in Figure 30 may be helpful. It can be shown from ray-optics and diffraction theory that a point source and a first parabolic cylinder can be employed to generate a virtual line-source over an angular sector. Such a virtual line source can then be used to excite a second parabolic cylinder. The focal axes of the parabolic cylinders will be orthogonal in space. Reference 9 teaches that feed and subreflector blockage can be eliminated by rotating the entire subsystem 90-degrees about an axis of symmetry of the virtual line source. This is the starting point for the monopulse and zooming discussion.

Several advantages accrue from an arrangement such as Fig. 30. Not only has feed and subreflector obscuration been eliminated but a line-feed has been coalesced to a point feed. This is particularly helpful for multibeam formation in a communications application. It also provides an indication that amplitude-sensing monopulse may be possible. Ray tracing, and a mapping of the focal region fields, wavefronts, and time-average Poynting vectors clarifies the question as to where the feeds should be placed, and how they should be oriented. Since only uniplanar symmetry exists, diamond monopulse becomes a logical choice, and it is apparent at the outset that one of the two error channels will violate the monopulse postulates somewhat.

[1] Ref. 10
[2] Ref. 11
[3] Ref. 12
[4] Ref. 13
[5] Ref. 14

At this stage of the development zooming is not included. By taking advantage of the generating arcs of the two reflectors of the system, zooming can be achieved through the simple expedient of telescoping the non-intersecting end of the subreflector and the two available ends of the main reflector. Since this is a mechanical consideration, surface thickness must necessarily be small when compared with the operating wavelength. In this manner, the beamwidth of the sum channels and error channels of a diamond amplitude-sensing monopulse system can be varied over significant latitudes. It was shown, via the Kirchhoff-Kottler diffraction simulation, that the clues provided by ray optics analysis actually lead to a workable monopulse zooming technique.

A large amount of data was obtained on the dual parabolic cylinder antenna by means of the diffraction simulation. Subjects such as optimum polarization, source directivity and separation, and the interaction effects of simultaneous zooming in orthogonal senses on the monopulse characteristics were treated in detail. Only a few representative patterns are presented in this report to illustrate control over the beamwidth. A 100 percent increase in beamwidth for each pair of monopulse channels was selected arbitrarily. Exceedingly large zooming ratios incur large amounts of spillover at the reflector surfaces and degrade system efficiency prohibitively.

The following figures were derived for parameters not related to TDRSS, but to the U.S. Multibeam Project. Channel I is to be associated with zooming in the xz-plane, and departs from the strict enforcement of the monopulse postulates. Channel II is to be associated with zooming in the yz-plane and satisfies the postulates. A sum and a difference pattern exist for both Channel I and Channel II in this diamond-monopulse scheme. Only the pattern cut which displays the characteristic vee (V) difference pattern is displayed. The orthogonal null cuts were computed, but are omitted since they are of no special interest here.

Figure 31 and Figure 32 are the acquisition patterns of Channel I, and Figure 33 and Figure 34 the acquisition patterns of Channel II when these channels are using their wide-beam capability simultaneously. Figure 35 and Figure 36 are the tracking patterns of Channel I, and Figure 37 and Figure 38 the tracking patterns of Channel II when these channels are using their narrow-beam capability simultaneously. Other permutations, with independent zooming of these channels, were examined in detail and found to give equally good or better results than those shown by the above.

The placement and orientation of the feeds can be varied over fairly wide latitudes without serious effect, but one rule must be observed. Feed placement for Channel I is particularly critical since the Airy disc and bright-ring struc-

ture is inclined approximately 28 degrees with respect to the x-axis in the acquisition mode for 100 percent beamwidth increase. The Airy disc and bright-ring structure is inclined approximately 19 degrees in the tracking mode. As the zooming is varied between these two extremes the angle of the incline varies accordingly, and a suitable mechanism with rotating rf joints can be used to synchronize feed position and orientation with displacement of a movable panel on the subreflector. Feed repositioning for Channel II is far less critical and can be ignored when the feeds associated with that channels are not highly directive.

Figure 39 shows the electric field distribution in the vicinity of the system focus under the 100 percent zoom condition. Figure 40 gives the corresponding wavefronts, and Fig. 41 the time-average Poynting vectors under reception. The object, when positioning the feeds, is to insure that a pair of monopulse feeds for a given channel shares a common wavefront. Figure 42 shows the electric field distribution near the focus when there is no zooming. Figure 43 gives the wavefronts, and Figure 44 the time-average Poynting vectors for the tracking mode of operation. In short, the monopulse feeds should always be situated in the Airy disc, whatever the inclination of the disc under zooming. The solid lines on these six figures for the focal region depict the boundary rays traced through the dual parabolic cylinder system for the tracking mode and can be used as a reference when identifying Airy disc inclination. It is noted that the focal region is more diffuse for the acquisition case, which can affect feed design. The null-to-null radius of the Airy disc can be thought of as being increased by a magnification factor M so that $R_{AD} \approx 1.22\ F\lambda M/D_e$, where D_e is the effective diameter for the traverse being considered.

TELESCOPING PARABOLOID

Figure 45 illustrates a telescoping paraboloid geometry which in principle should achieve zooming by aperture reduction, at the expense of increased spillover loss, in the same manner as the dual parabolic cylinder antenna. The aperture shape was chosen arbitrarily. It could as well have subtended a central angle of 180-degrees, 270-degrees, or some other value, instead of 90-degrees. As with dual parabolic cylinder, the antenna will exhibit only uniplanar symmetry, therefore diamond monopulse is a logical choice here also. Ray-tracing indicates that the Airy diffraction disc and bright-ring structure will be inclined in a manner directly related to the amount of zooming required. Near-field mappings of intensity, wavefronts, and time-average Poynting vectors bear out the ray-tracing conclusion. Feeds are then synchronized mechanically so that the monopulse cluster shares a common wavefront at all times. The folding of the paraboloid could take many forms. For example, a fan-like structure can be envisioned which telescopes the generating arc into

a small sector by mean of an axial rotation. It would appear that this method of zooming a paraboloid is poorly suited to an application where a deployable mesh antenna is employed.

The basis for feed positioning was determined for a TDRSS-related geometry and operating frequency. Figure 46 to 48 are the electric-fields, wavefronts, and time-average Poyting vectors for the 90-degree sector for the acquisition case only since the characteristics of a full-paraboloid or 360-degree sector are well-known. Only ordinary care was exercised in reading the phase information on the wavefront plot to place the Channel I feeds. When time permits, the computer program will be used to optimize this placement to insure that the monopulse feeds share a common wavefront.

Figures 49 and 50 are computed results representing the Channel I sum and difference patterns as seen in the $\phi = 0°$, 180° principal-plane cut. The geometry is asymmetric for this cut, but the quantitative data show only slight asymmetry for the patterns over the range of angle θ studied here. The Channel I sum pattern is given by Fig. 51, and is symmetric in $\phi = 90°$ and $\phi = 270°$. It was found that the corresponding error pattern, ideally a zero-intensity pattern ($E = -\infty$ db), had significantly high values which would render the proposed zooming method nearly worthless. See Fig. 52. At this time the cause of the difficulty is not known. It is possible that inexact placement of the Channel I feeds is responsible. Null depth was only 40 db below sum channel maximum in Figures 49 and 51, indicating some departure from the monopulse postulates.

Figures 53 and 54 are computed results representing the Channel II sum and difference patterns as seen in the $\phi = 90°$ principal-plane cut. Fig. 55 gives the $\phi = 0°$ and $\phi = 180°$ Channel II sum pattern cut. The corresponding error-channel cut is not plotted as it was found to lie about 200 db below the sum-channel maximum. Phase gradients in all $\phi = 0°$ and $\phi = 180°$ cuts are due to the "offset" antenna aperture (with respect to the coordinate origin).

Since the telescoping paraboloid is not well-suited to TDRSS applications, the exploratory effort for this geometry was restricted. It may be that more careful feed placement would show improved monopulse characteristics. Also, 180-degree and 270-degree sectors may exhibit better performance. The 90-degree sector chosen for the present study introduces a fairly severe asymmetry if the antiphase current distribution of the Channel I acquisition case is examined with respect to the $\phi = 0°$ pattern cut. In any event, additional information is needed to define the monopulse zooming characteristics of the telescoping paraboloid.

CASSEGRAIN (DEFOCUSSED FEED)

The geometry for this approach is the same as Fig. 19, and the objective is to obtain amplitude-sensing monopulse acquisition patterns by displacing a first feed cluster in the direction of the subreflector. Ku-band monopulse tracking patterns are then obtained by means of a second feed cluster situated at the conjugate focus (F*) in a conventional manner. The computer simulation was used to determine whether or not a position for the defocussed feed could be found to produce acquisition patterns useful to the TDRSS. Displacements of 2λ, 10λ, 15λ, 20λ, 25λ, 30λ and 40λ were studied in detail to determine the Σ and Δ pattern characteristics. It was found that 30λ and 40λ produced approximately 153 and 286 percent increase in beamwidth with source patterns exhibiting a directivity associated with N = 77.3 and lateral displacements of $\sqrt{2}\lambda/4$. Only the 30λ case is discussed here. It was also found that source directivity could be reduced to N = 50.0 without apparent penalty, and to N = 25.0 with degradation of the shape of the Δ -pattern amplitude and phase characteristics. The amplitude remained monotonic and was free of inflection points that would lead to ambiguous target resolution. The error slope was low over a portion of theta-domain, however, and the phase characteristic departed somewhat from that of the sum channel for the larger values of theta (θ) with N = 25.0 for the source pattern.

A set of monopulse acquisition patterns for N=77.3, $|\overline{\rho}_\epsilon| = \sqrt{2}\lambda/4$, and $\Delta\overline{\rho}_\epsilon$ (feed displacement) = 30λ is presented as Figures 56 and 57. Conventional monopulse, in which all four feeds enter into the formation of each error channel, was employed. (The associated set of monopulse tracking patterns, developed earlier, is given by Fig. 10 and Fig. 11.) It is noted that the phase and amplitude patterns are excellent for both the Σ and Δ channels, approaching the ideal under the monopulse postulates, but this was obtained at the expense of displacing the feed 30λ. (Previously, it was shown that a hyperboloid need be displaced only 2λ to achieve a comparable amount of beamwidth increase or zooming.) At this stage of the investigation, only raw levels from the integration via Kirchhoff theory were available in lieu of rigorous gain calculations. The indication was that subreflector displacement resulted in about one-half decibel of defocus loss, whereas feed displacement resulted in about two and one-half decibels of defocus loss, based on raw level data only. It also remains to verify that the acquisition feed at F*' and the tracking feed at F* can co-exist without serious adverse effects. Both utilize the hyperboloidal subreflector, and the former partially obscures the latter, but apparently not significantly. If S-band monopulse is required on TDRSS, the hyperboloid can be made dichroic, but this does not affect the preceding discussion for th Ku-band acquisition and tracking functions.

GREGORIAN (DEFOCUSSED FEED)

The geometry for this approach is that of Fig. 8, but the subreflector is not truncated. Ku-band monopulse tracking patterns are obtained by means of a feed situated at conjugate focus (F*) in a conventional manner. The computer simulation was used to determine a position for a defocussed feed to produce acquisition patterns useful to TDRSS. A feed displacement of 40λ in the direction of the subreflector produced the following results using N = 41.7 for the source elements and $|\overline{\rho}_\epsilon| = \sqrt{2}\lambda/4$ for lateral feed displacement. Figures 58 and 59 show the acquisition sum and difference patterns. These can be compared with the tracking patterns given by Figures 10 and 11. The characteristics of the acquisition patterns appear useful. The raw levels of the two sets of figures cited above should not be compared since the former were obtained by a different method (subsystem backscatter data injection), and the values of N were different between these computer runs. The difference in N will drastically affect the level of the results, but the shape of the patterns is relatively insensitive to this parameter for a dual reflector system.

A partial obscuration of the tracking feed by the (defocussed) acquisition feed will result. It remains to show that these two feeds can co-exist without serious adverse effects. Probably the best way to optimize feed location for defocussed-feed, confocal-surface arrangements is by obtaining a mapping of the focal region fields, wavefronts, and time-average Poynting vectors as this eliminates the cut-and-try approach via far-field transmit-pattern results. This work is now being undertaken. It is also noted that the S-band tracking function can be accommodated here by nesting the S-band and Ku-band track feeds at the conjugate focal plane (F*). The defocussed Gregorian does not have the disadvantage of the truncated Gregorian system since there is no physical object at the focal-plane (F) of the paraboloid. Also, a dichroic subreflector is not required with the defocussed Gregorian. The defocussing loss is not known for the latter at this time, but will be determined via a secondary pattern integration.

CONCLUSION

The results of this interim document show that at least ten methods of zooming microwave reflector antennas can be identified.[1] Phased array techniques were specifically ruled out, although it is known that these afford a highly flexible approach. It appears that some of the methods studied in this report inherently involve a reduction in directivity gain, and a reduction in

[1] Ref. 5, page 415

spillover efficiency, or a defocussing loss. On occasion both of the latter losses are a consequence of zooming. The spillover losses appear to be very high when beamwidth increases of 200 percent or more are required of those systems that mechanically alter the main or subreflector dimensions. When mechanical motion is ruled out as a means of achieving zooming, the nested paraboloid approach is attractive. The Cassegrain and Gregorian systems which utilize feed defocussing also become attractive when mechanical displacement of elements is disallowed, however, the analogue nature of the zooming is lost with the latter.

Whatever system is studied, satisfaction of the monopulse postulates is an important consideration, and it is inadvisable to analyze the zooming of a pencil beam only. Geometrical asymmetry, and departure from confocal arrangements, were found to be nearly synonymous with violation of the postulates, but often resulted in useful, practical systems. Mapping of the focal region fields was found to be an indispensable aid in determining monopulse feed location for variable beamwidth designs. The defocussed Cassegrain and Gregorian systems should be examined in greater depth with regard to parameters governing source directivity, lateral displacement, and axial displacement using the three near-field maps (isophotes, wavefronts, and time-average Poynting vectors). Finally, the frequency-independent aspects of zooming should be considered. Although the TDRSS requirements which motivated much of the present effort did not anticipate significant frequency changes, it is noted that departure from confocal geometry implies that frequency change will require complete redesign of the zoom system. This should be contrasted with the nested paraboloid approach, where both acquisition and tracking functions are wideband.

A search in the Patent Office, Washington, D. C. appears to bear out the commentary of another investigator[1] that "there has not been sufficient information available to evaluate greatly defocussed antennas for monopulse tracking operation." Related patents of interest have been collected and are identified here.

This is an interim report. Work is continuing on the exploration of basic methods for achieving variable beamwidth or zoom capabilities for microwave antennas. Among these is the idea of utilizing the first Airy bright ring of a dual reflector system to obtain a set of low-gain monopulse acquisition patterns. Another approach is to "borrow" energy from the periphery of the Airy disc of a system with a large magnification factor for acquisition purposes, and then restore this energy, by switching, to the tracking or data mode of operation after acquisition has been achieved. The results of these efforts are directed toward relieving the acquisition problems on TDRSS, Space Shuttle, and other user spacecraft.

[1] Ref. 15

ACKNOWLEDGMENTS

The author acknowledges the use of background material in textbooks and journal articles in addition to the following. All Fortran programming used in connection with the Kirchhoff-Kottler simulation was performed by R. Miezis and W. Bartley of Programming Methods, Inc. under contract to NASA, Goddard Space Flight Center. The author acknowledges the many helpful technical discussions with A. F. Durham, Branch Head, Antenna Systems Branch Network Engineering Division. Valuable input was also provided by L. R. Dod and L. F. Deerkoski concerning the Tracking Data Relay Satellite System (TDRSS) and various aspects of microwave zooming and associated diffraction phenomena. W. Williams of the Antenna Systems Branch provided valuable measured results which increased the level of confidence in the computations, and led to a better understanding of the techniques under study. J. Pullara and M. Uhara of Martin Marietta Aerospace, also under contract to NASA, provided extensive system studies, and motivated interest in the defocussed approach to micowave zooming. Their measured results were also helpful in establishing loss estimates due to defocussing. Finally, the author acknowledges the effort put forth by R. Sandler of the Goddard Space Flight Center Office of Patent Counsel in conducting a search of existing art.

REFERENCES

1. Rhodes, D. R., "Introduction to Monopulse," McGraw-Hill Book Company, Inc., 1959.

2. Goddard Space Flight Center Documents:
   X-525-68-201, X-525-68-315, X-525-70-293,
   X-811-71-392, X-811-73-221

3. Patent Disclosure NASA Case Number GSC-11,760-1.

4. Patent Disclosure NASA Case Number GS-11,783-1

5. Redlien, H. W. Jr., "Monopulse Operation with Continuously Variable Beamwidth by Antenna Defocussing," IEEE Transactions on Antennas and Propagation, Vol. AP-16, No. 4, July 1968.

6. Hannan, Patent Number 3,364,490.

7. Ludwig, A. C., "Conical Reflector Antenna," IEEE Transactions on Antennas and Propagation, Vol. AP-20, Number 2, March 1972, pp. 146-152.

8. Goddard Space Flight Center Document X-811-72-392

9. Cheo, B., "A Solution to the Equiangular Spiral Antenna Problem," Electronics Research Laboratory, Department of Electrical Engineering. University of California, Contract No. DA 36-039 SC-84923, Nov. 1960.

10. Spencer, Holt, Johanson, and Sampson," Double Parabolic Cylinder Pencil-Beam Antenna," IRE Transactions-Antennas and Propagation, January 1955.

11. Kelleher, Patent Number 3,365,720.

12. Spencer, Patent Number 2,825,063.

13. Goddard Space Flight Center Document X-811-73-221.

14. Patent Disclosure NASA Case Number GSC-11,862-1.

15. Related patents:

Laibson, et al.	3,383,692
Kott	3,396,397
Bohnert, et al.	2,570,197
Tipton	3,176,302
Brunner	3,276,022
Hersch	3,594,804
White	3,230,538
Williams, et al.	3,394,378
Kelleher	3,354,461
Van Staaden	2,991,473
Ruben	3,504,368
Thourel	2,913,723

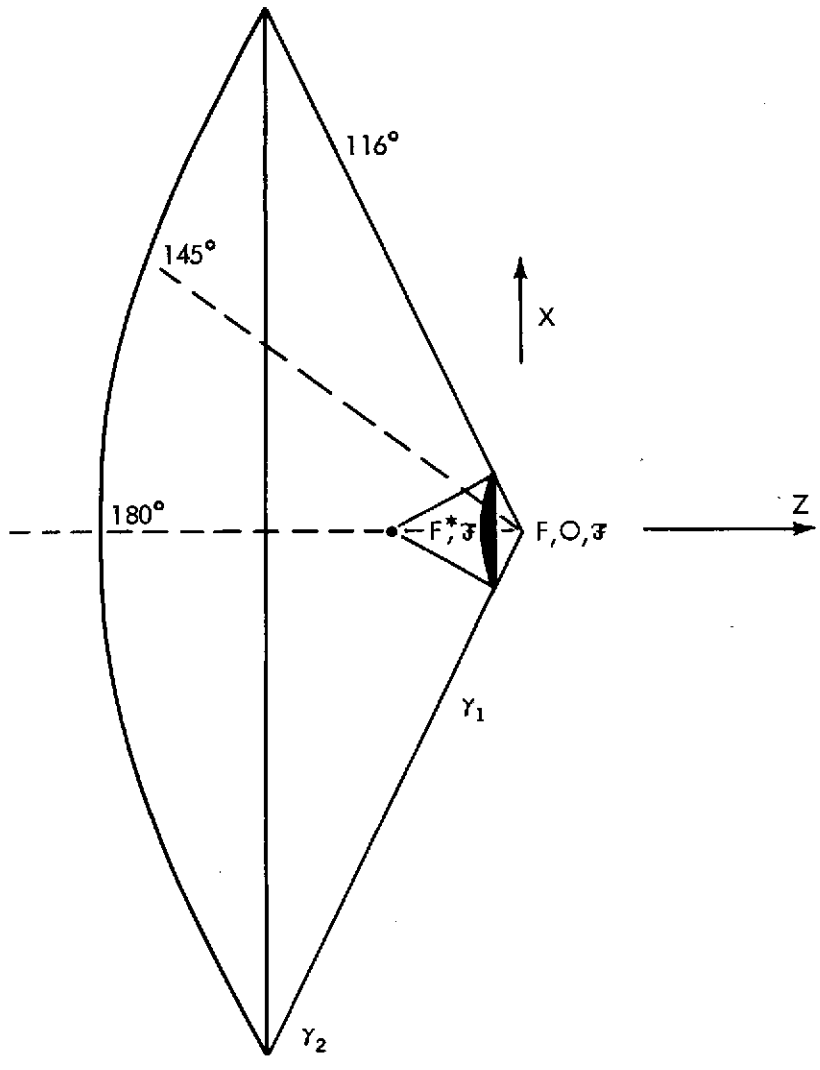

f = 15.0 GHz
λ = 0.06557'
σ_{02} = 6.25'
F/D = 0 4
F = 5.0'
σ_{01} = 0.625'
a = 0.688'
c = 0.344'
FF* = 2Cϵ = 1.54'
$\epsilon = (1 + a^2/c^2)^{1/2} = \sqrt{5}$
N = 8.0
Z_1 = -F
P(I) = 1.0
P(J) = P(K) = 0.0
$\alpha = \beta = \gamma = 0.0°$
$|x\epsilon| = |y\epsilon| = \gamma/4$ (i =4)
Zϵ = - FF*

PARABOLOID

$$Z = \frac{\sigma^2}{4F} + Z_1$$

HYPERBOLOID

$$Z = C\,(1 + \sigma^2/a^2)^{1/2} - FF^*/2$$

LI_1 = 0.5
LI_2 = 5.0

Figure 1. Cassegrain geometry with displaced hyperboloidal annulus.

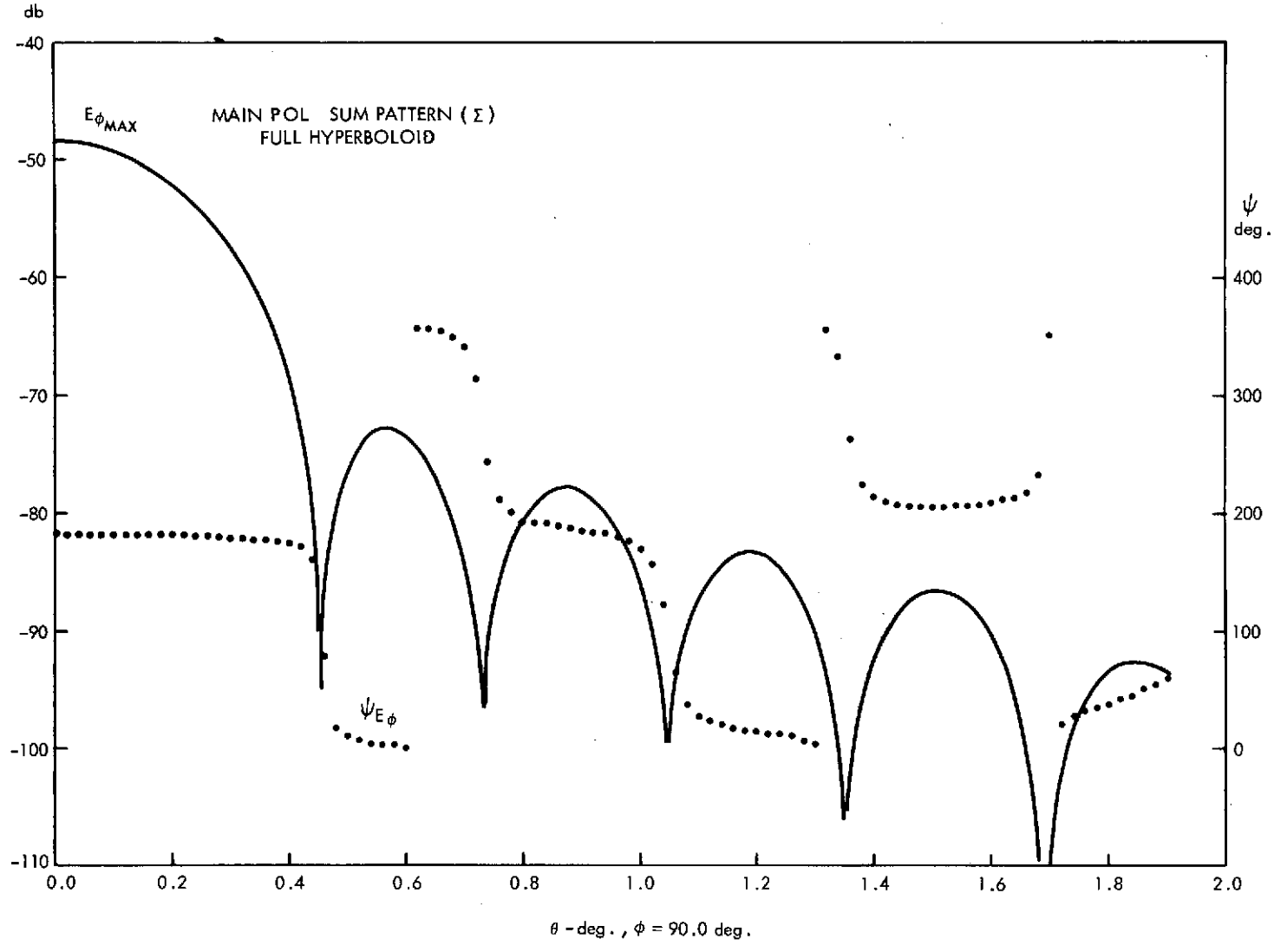

Figure 2. Tracking pattern, Σ-mode.

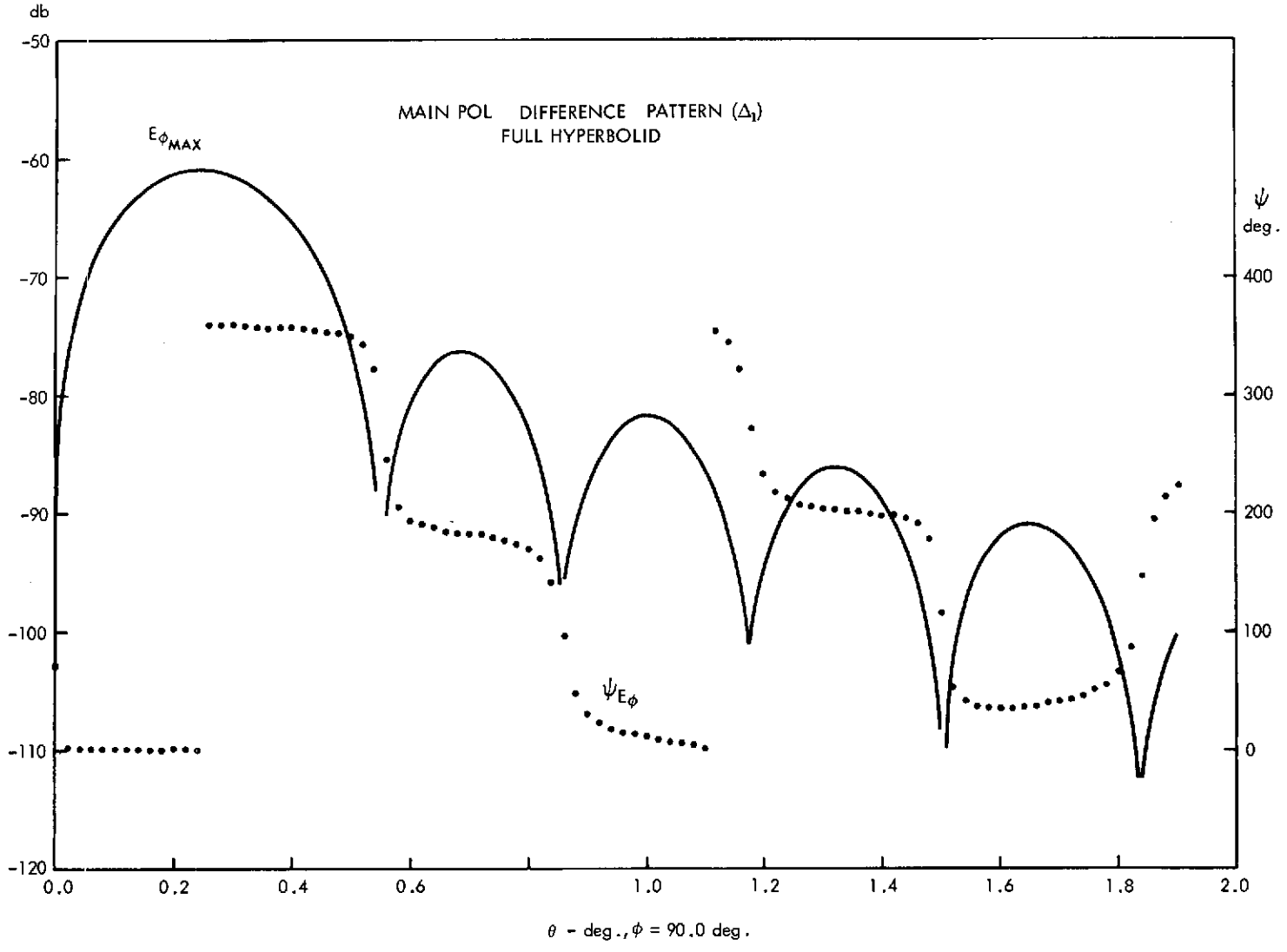

Figure 3. Tracking pattern, Δ-mode.

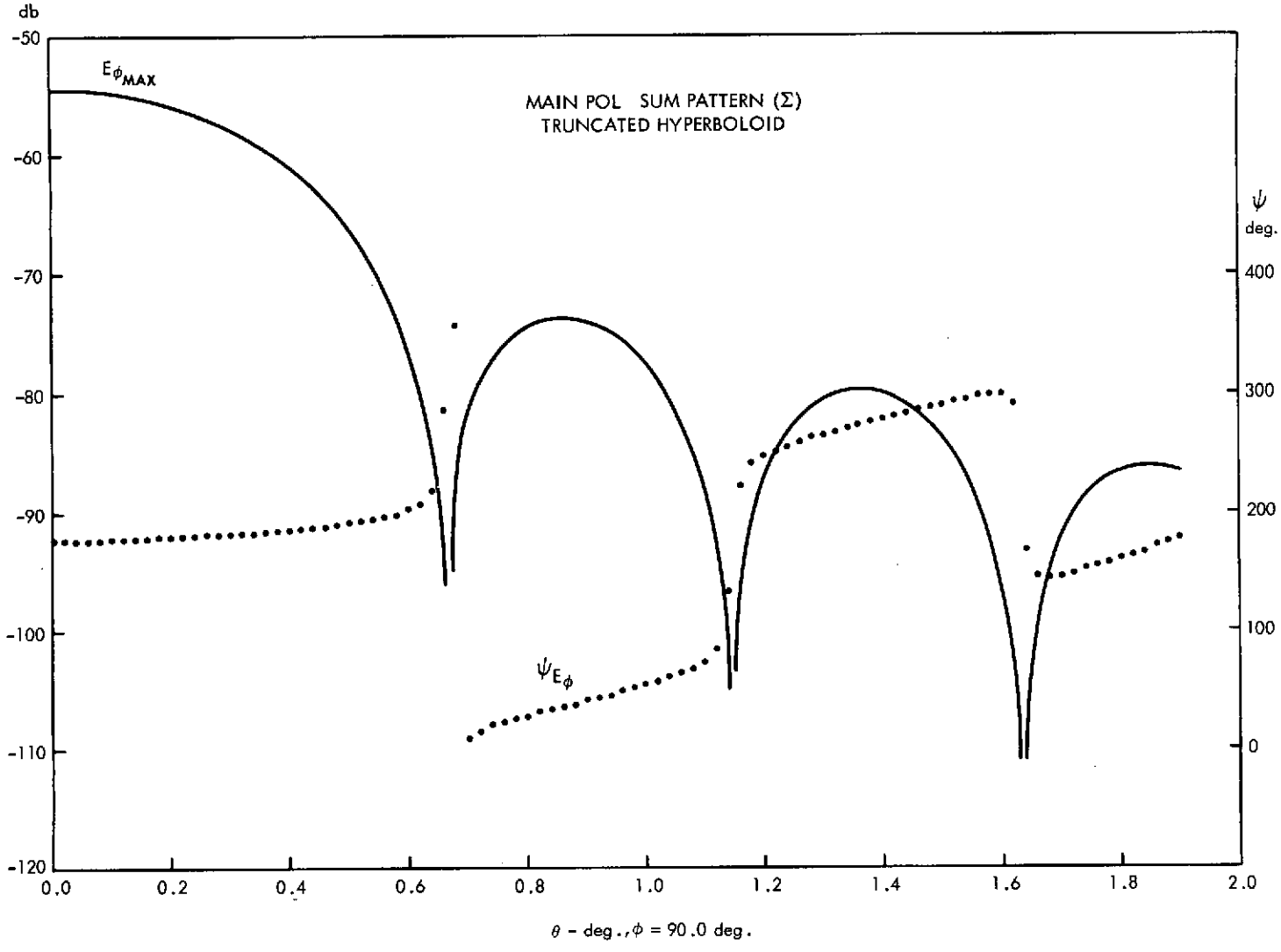

Figure 4. Acquisition pattern, Σ-mode, (truncated hyperboloidal annulus).

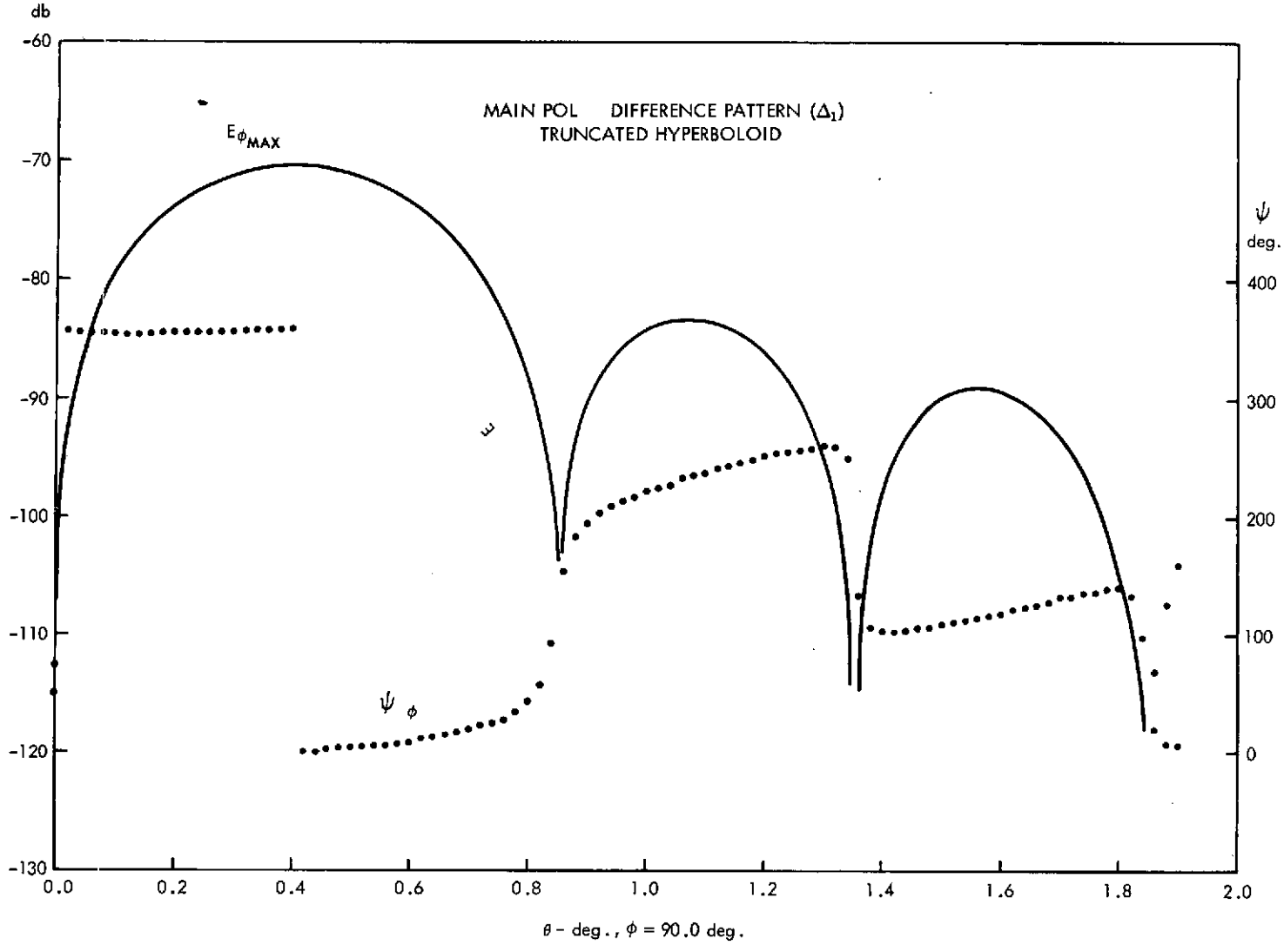

Figure 5. Acquisition pattern, Δ-mode, (truncated hyperboloidal annulus).

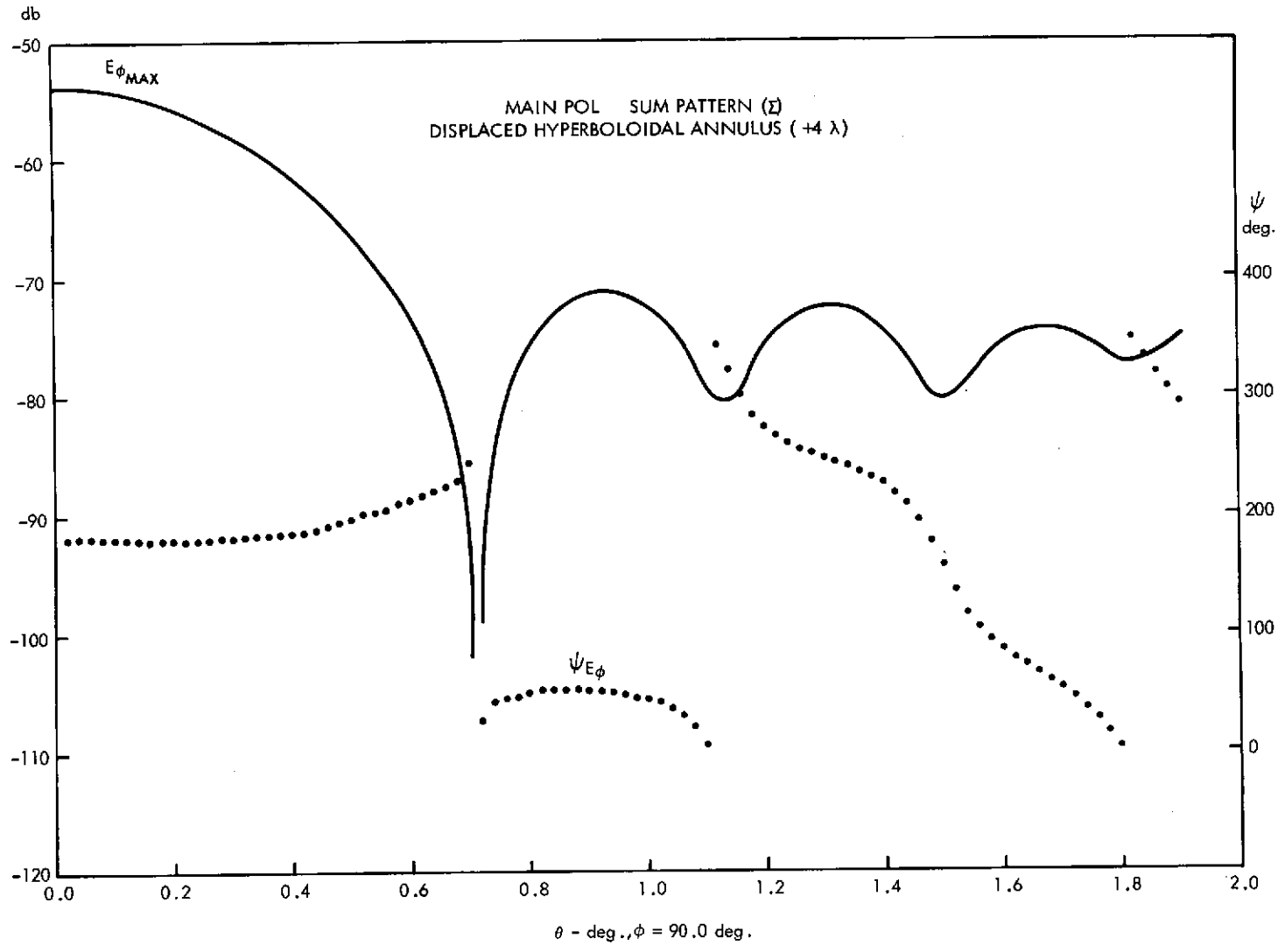

Figure 6. Acquisition pattern, Σ -mode, ($\delta = +4\lambda$ displaced hyperboloidal annulus).

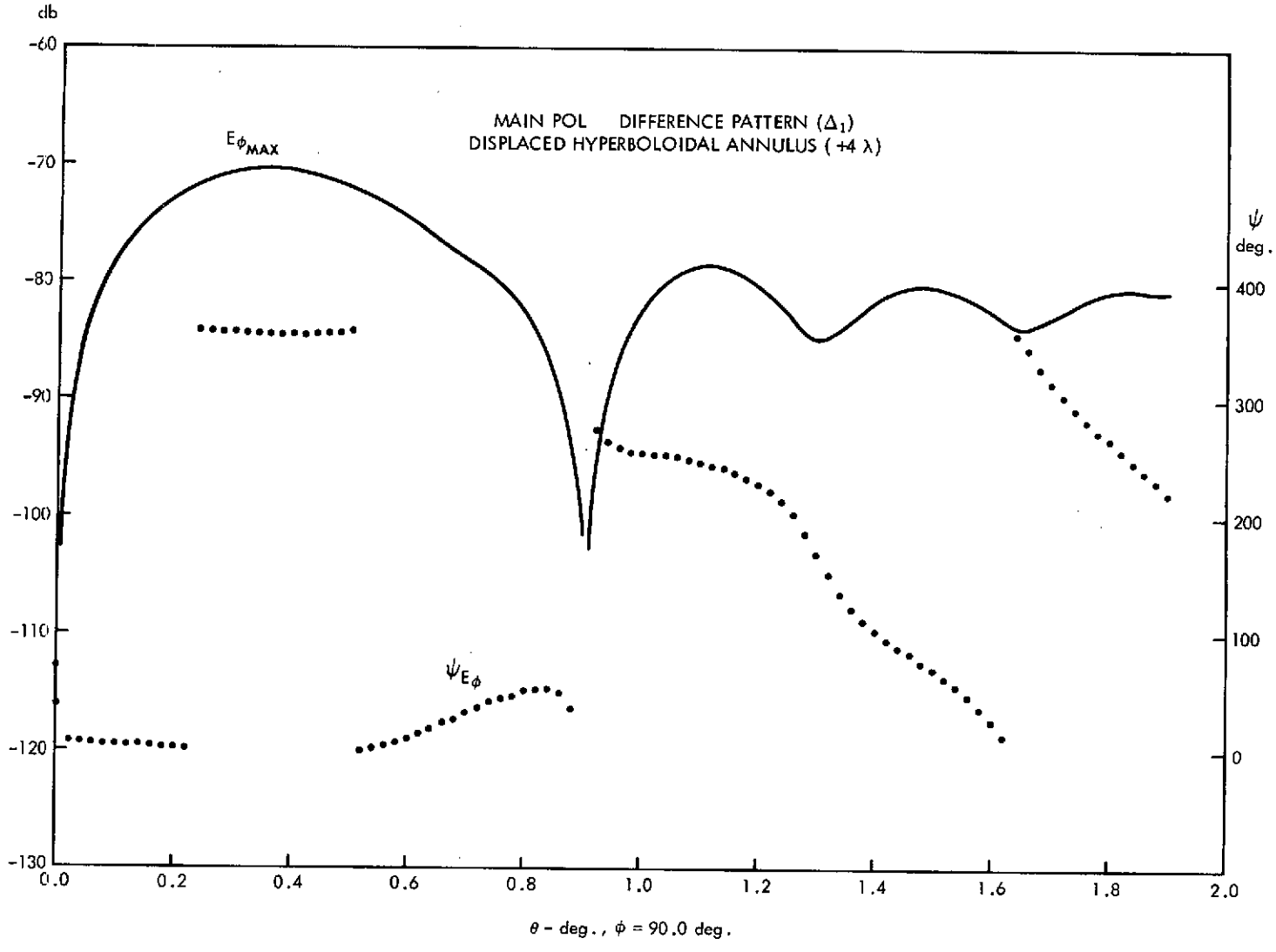

Figure 7. Acquisition pattern, Δ-mode, (δ = +4λ displaced hyperboloidal annulus).

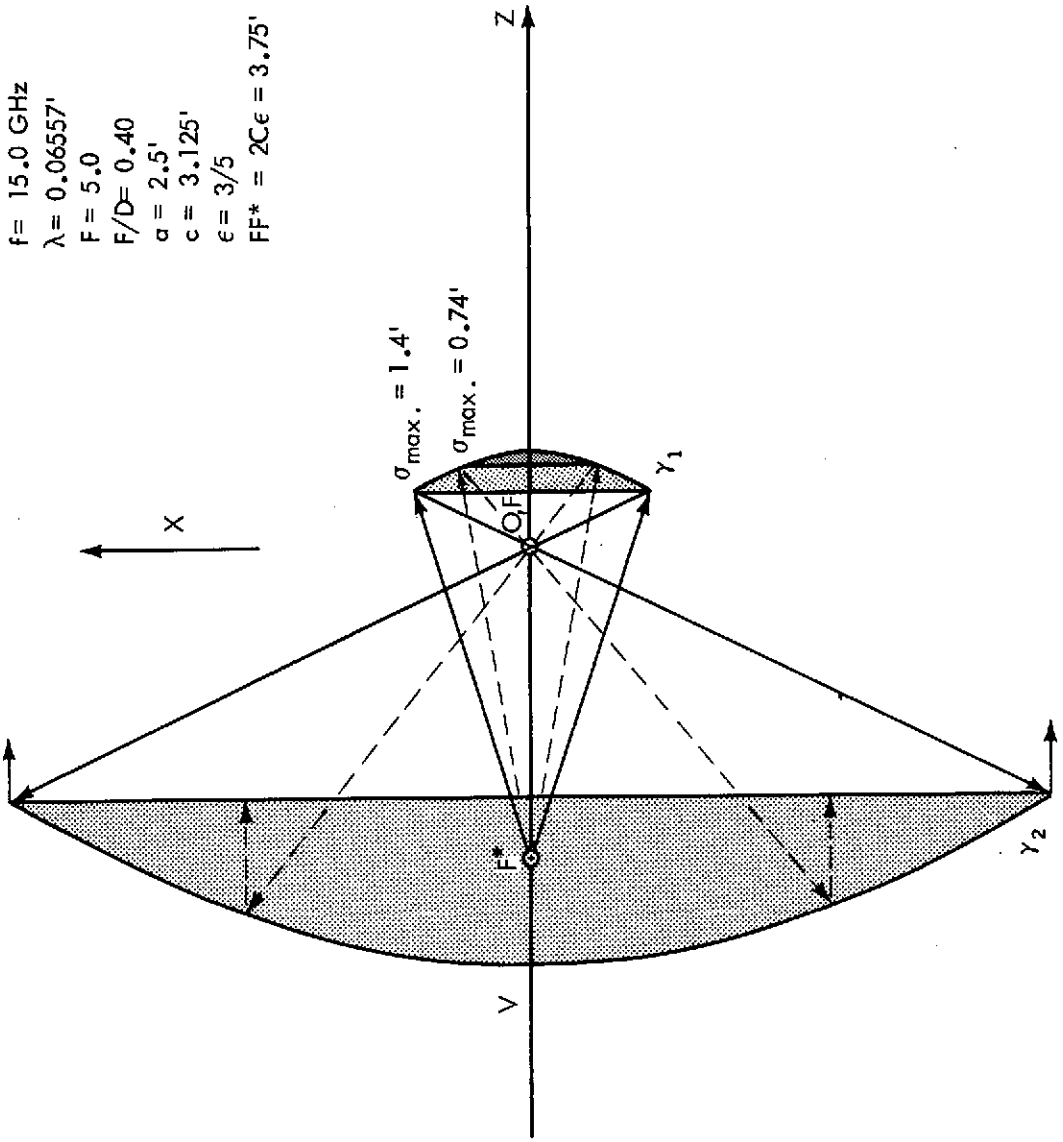

Figure 8. Gregorian geometry with truncated ellipsoidal annulus.

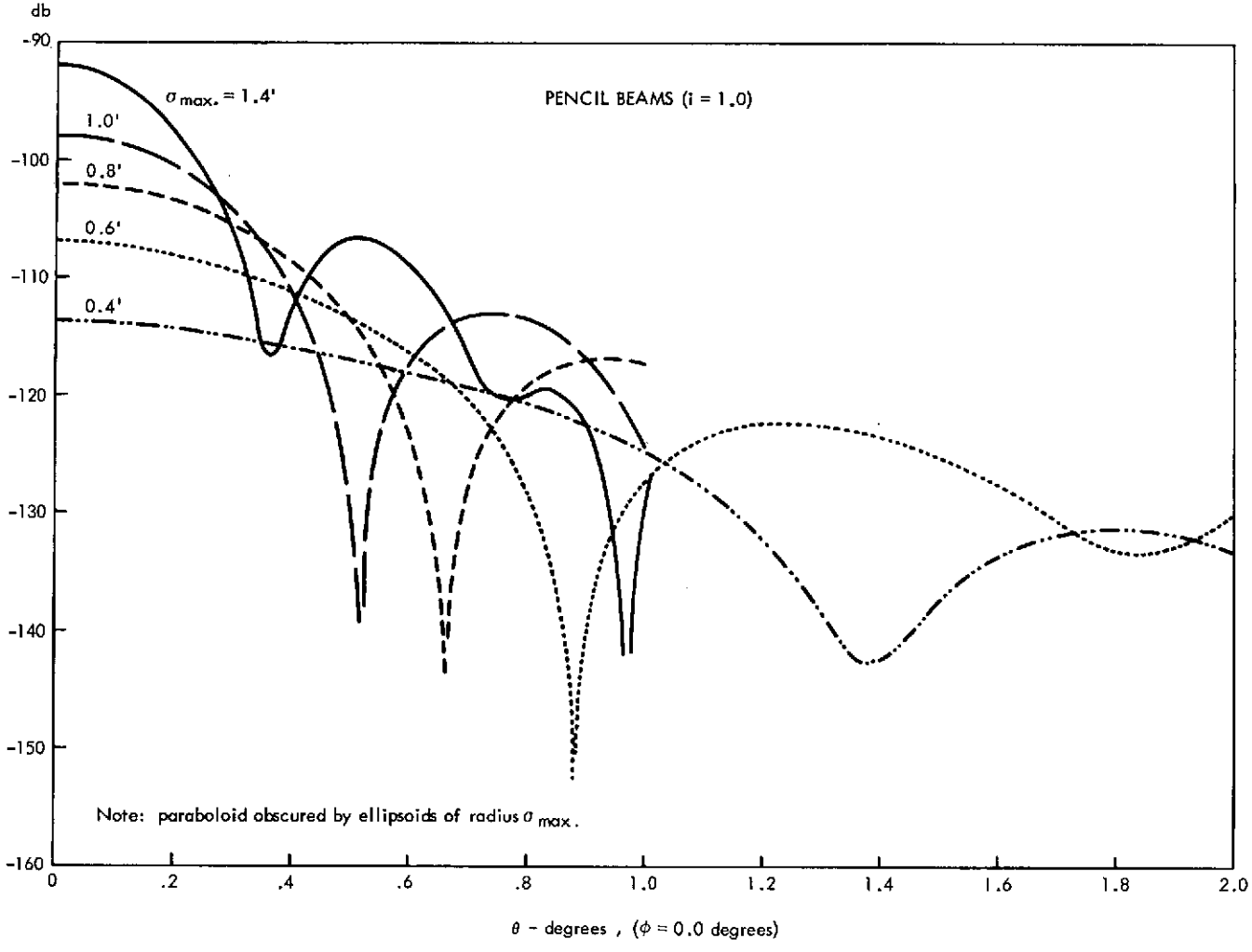

Figure 9. Beamwidth versus subreflector diameter for modified Gregorian system.

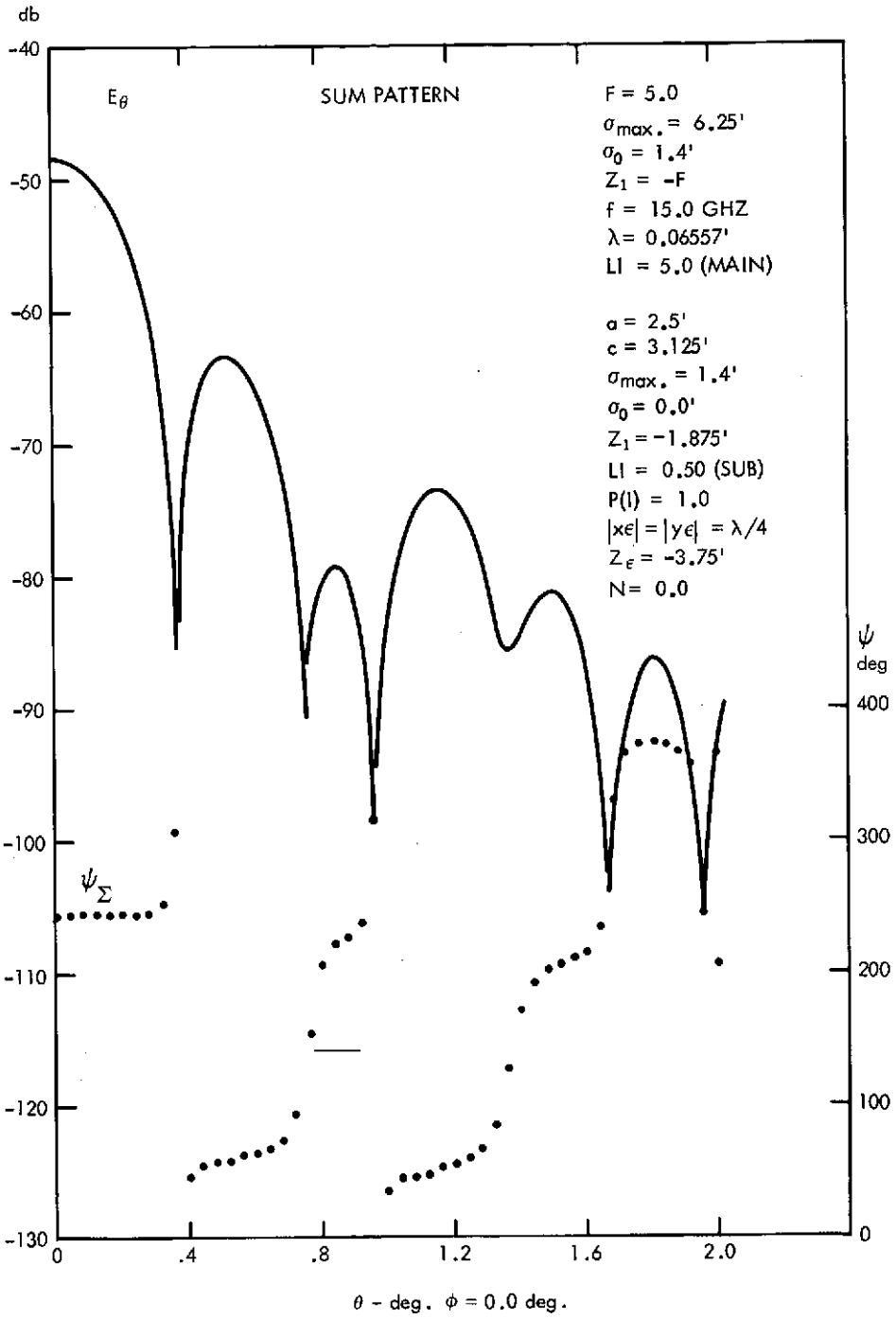

Figure 10. Tracking pattern, Σ-mode.

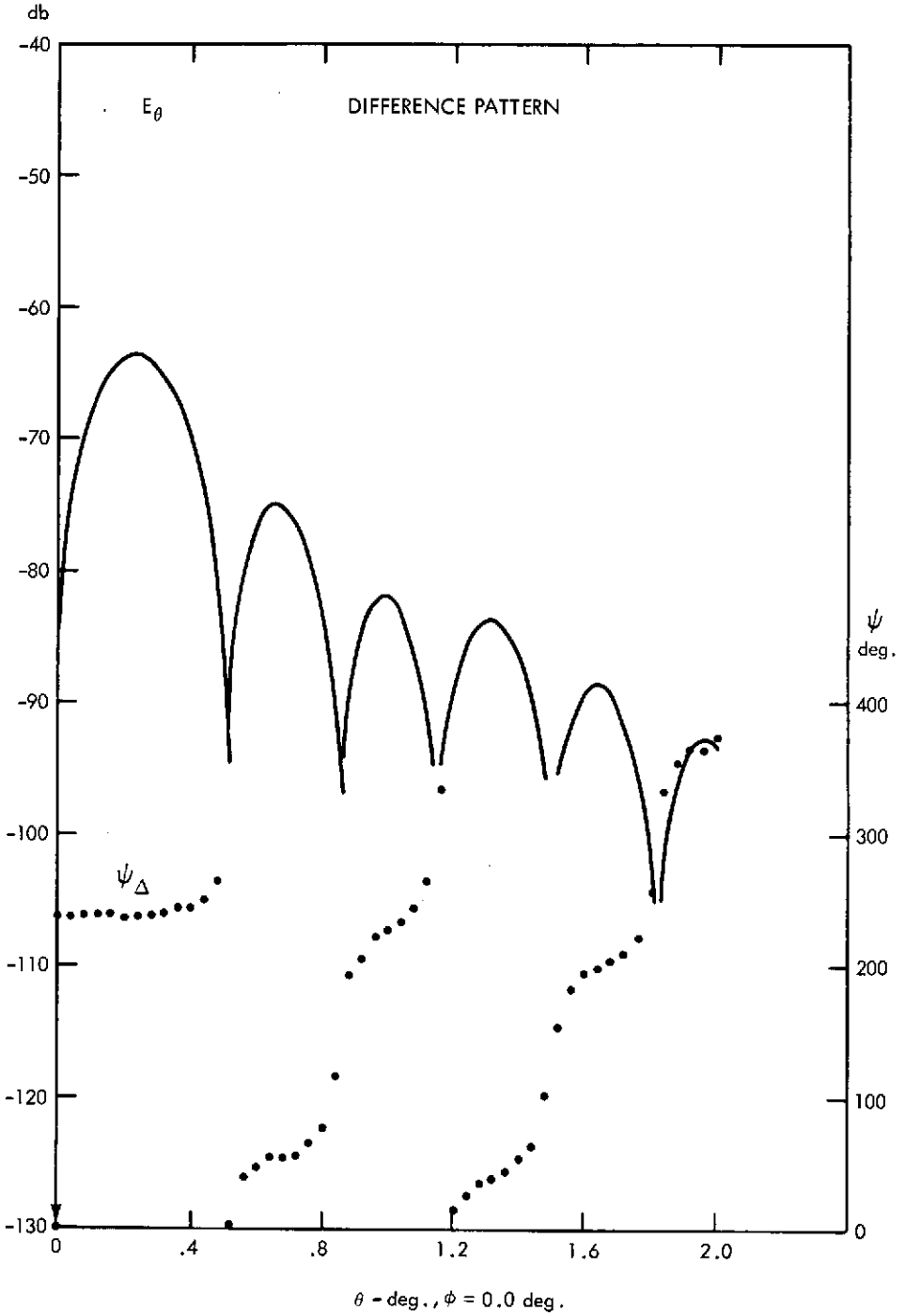

Figure 11. Tracking pattern, Δ-mode.

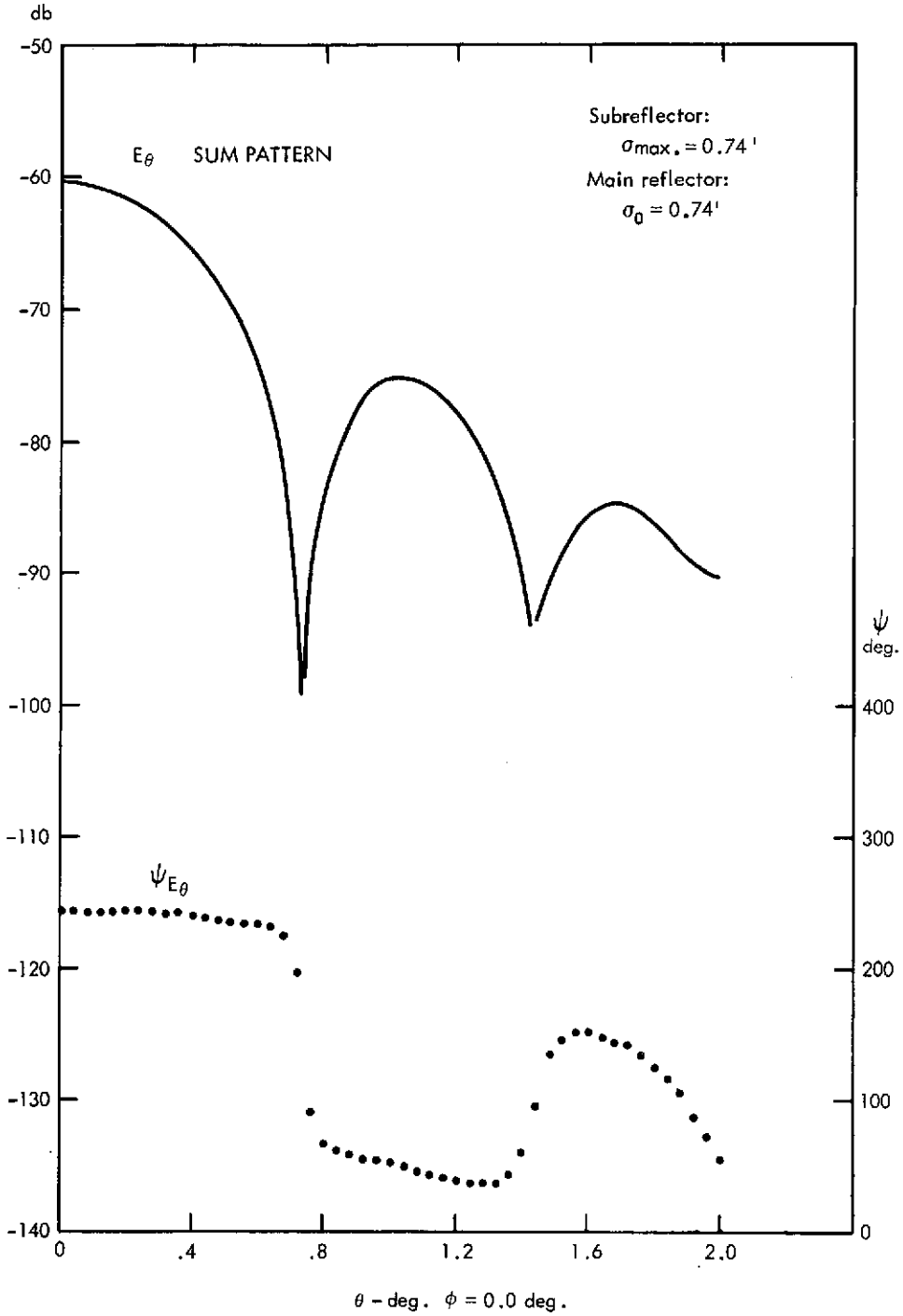

Figure 12. Acquisition pattern, Σ -mode.

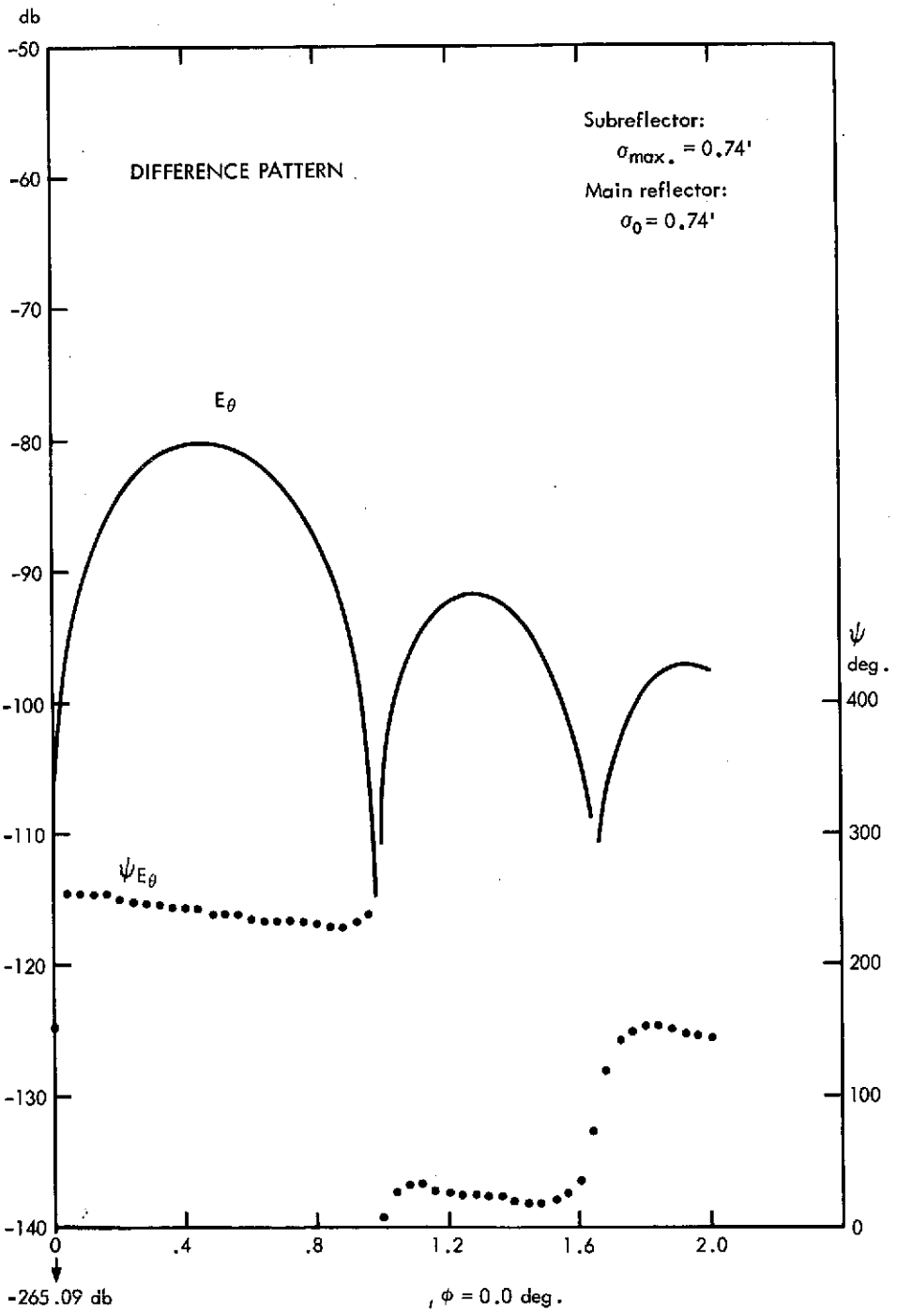

Figure 13. Acquisition pattern, Δ-mode.

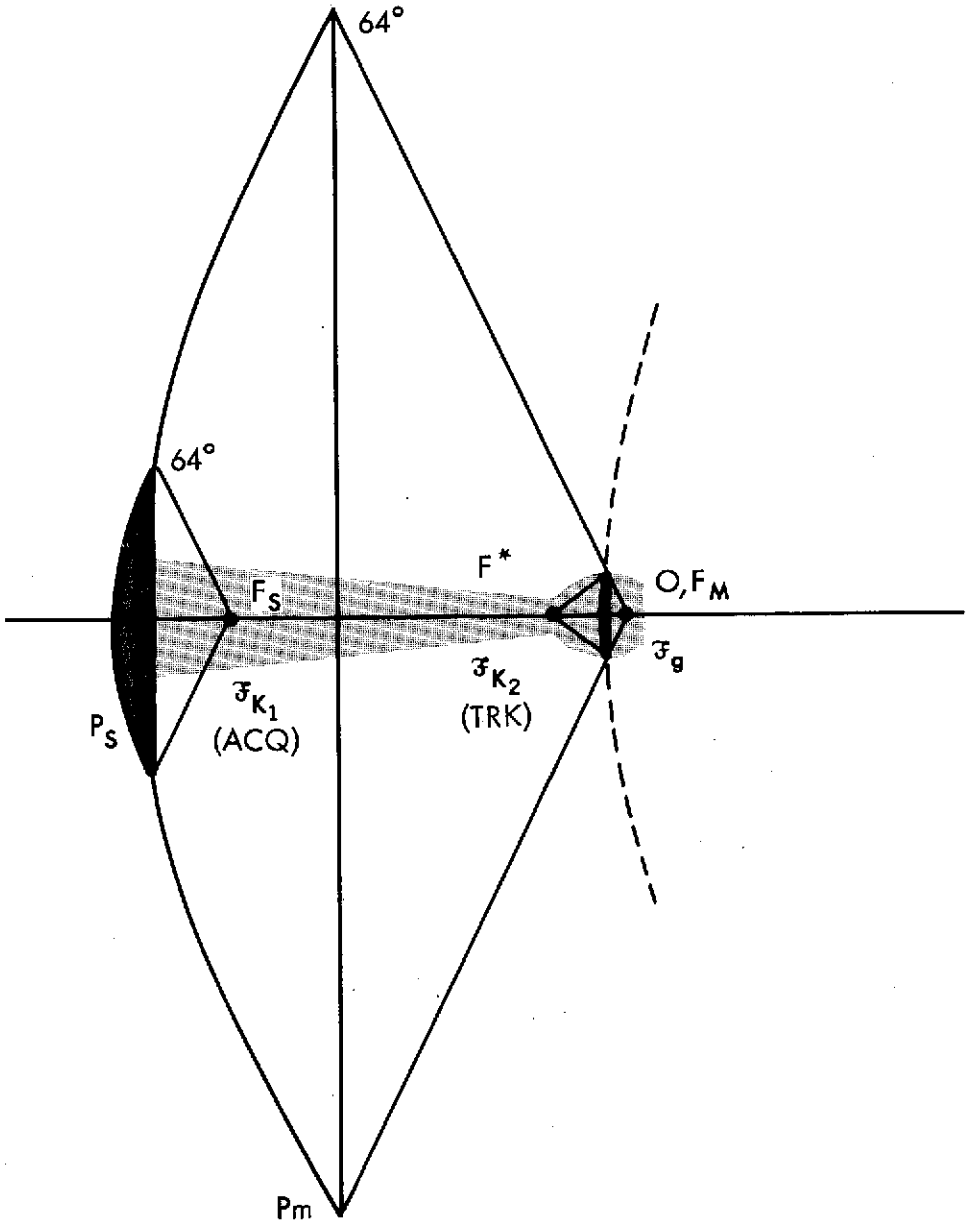

Figure 14. Nested Paraboloid Geometry.

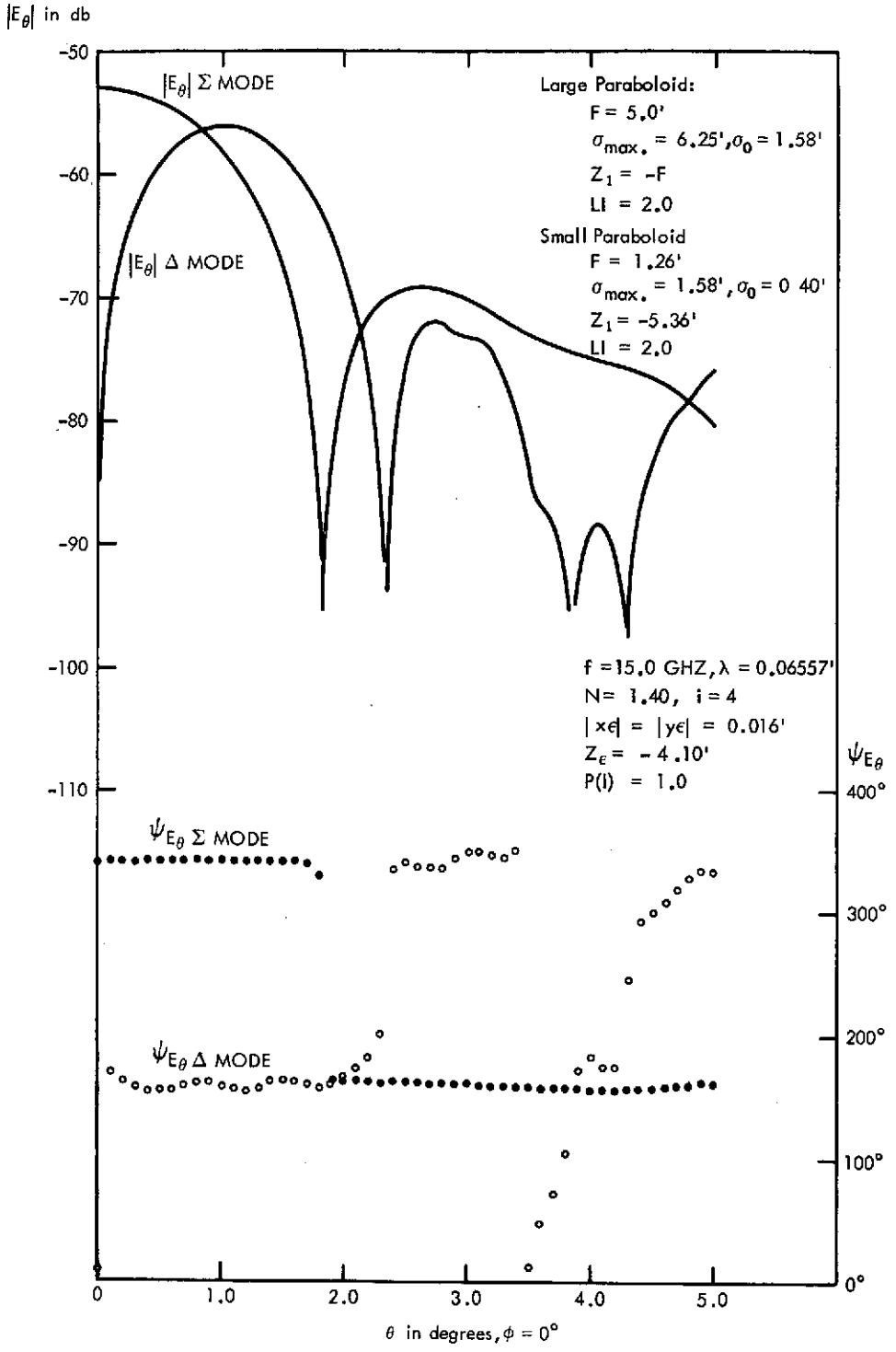

Figure 15. Acquisition patterns, Σ and Δ modes with main paraboloid.

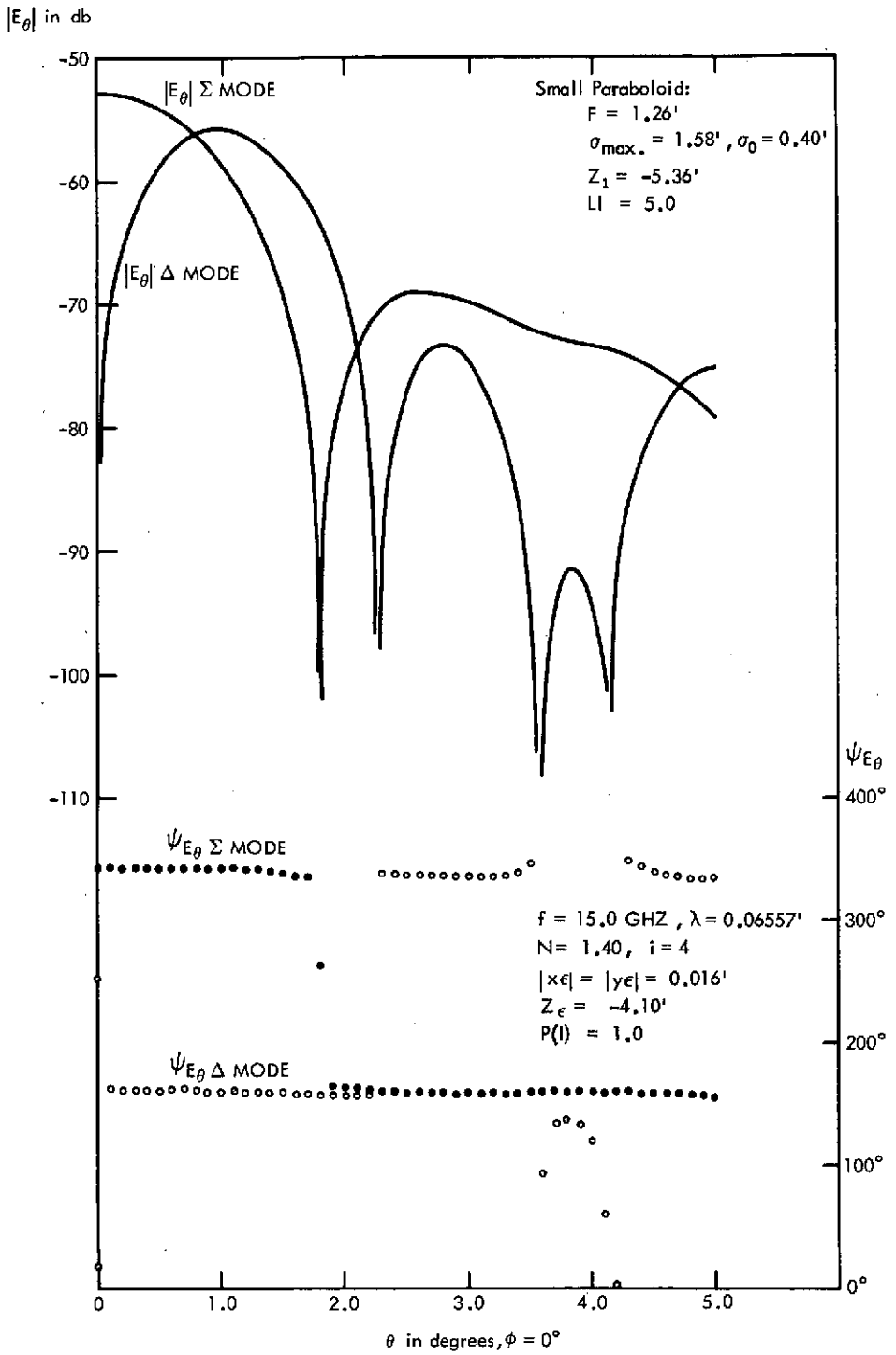

Figure 16. Acquisition patterns, Σ and Δ modes without main paraboloid.

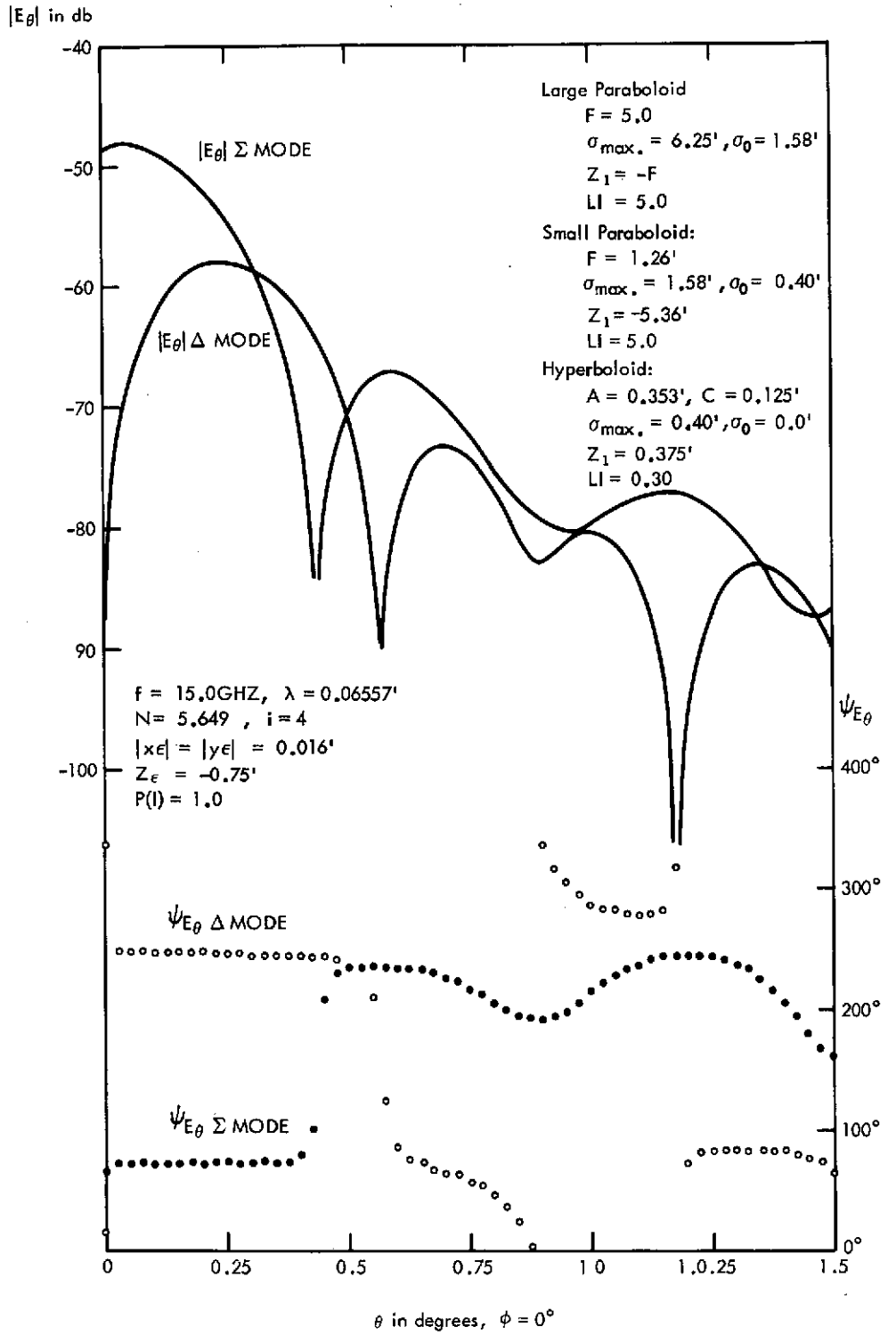

Figure 17. Tracking patterns, Σ and Δ modes with acquisition paraboloid.

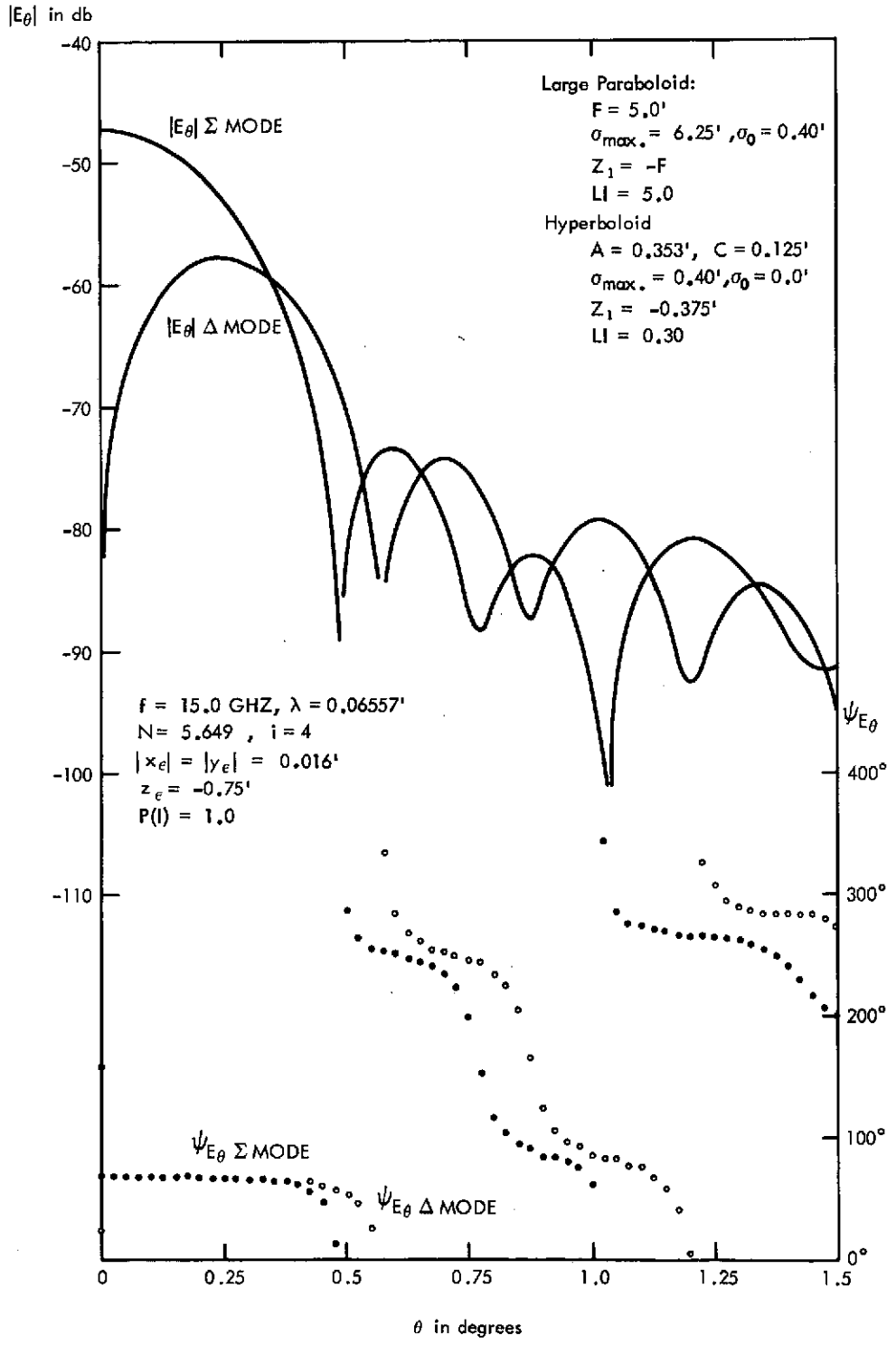

Figure 18. Tracking patterns, Σ and Δ modes without acquisition paraboloid.

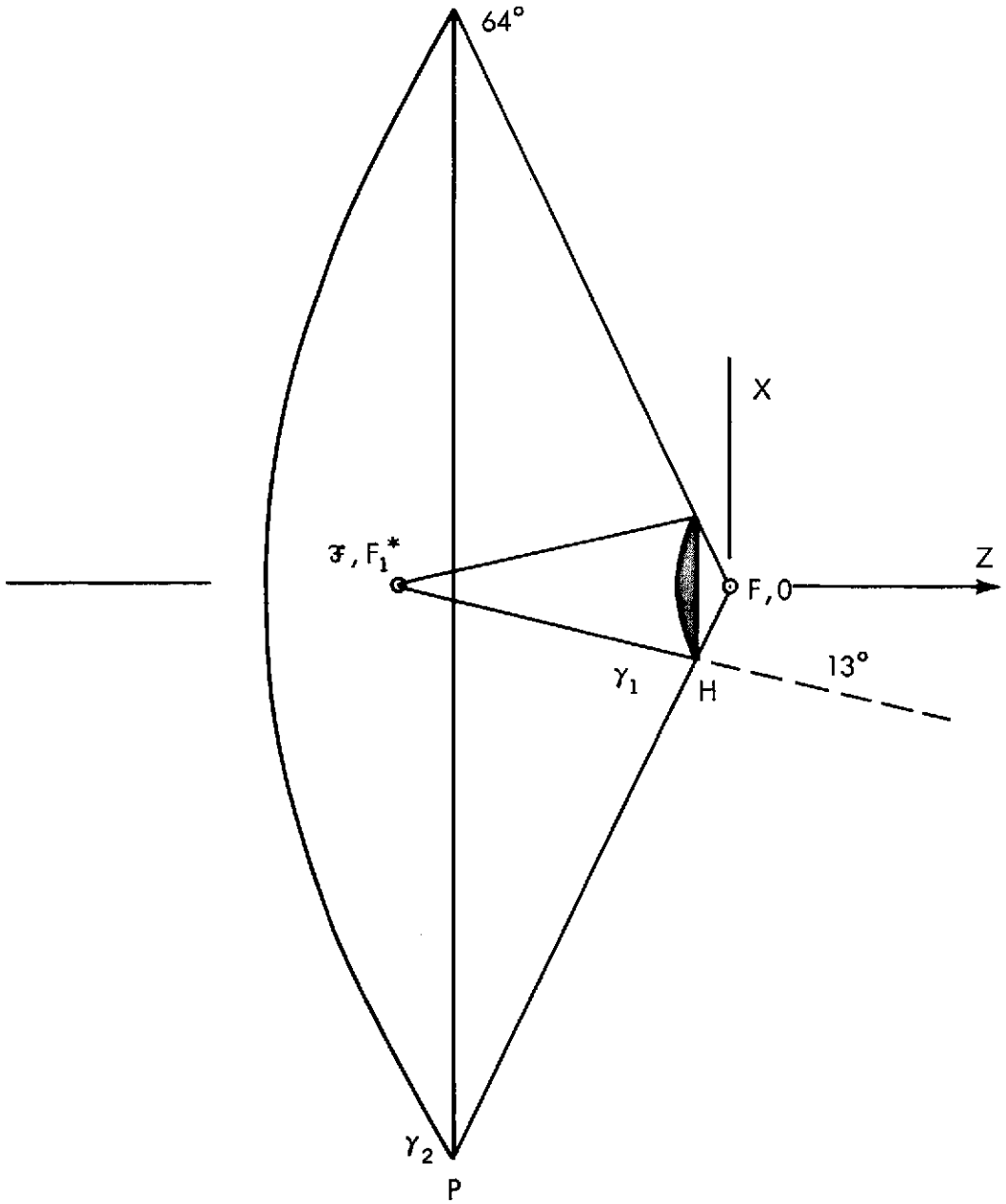

Figure 19. Cassegrain geometry with defocussed hyperboloid.

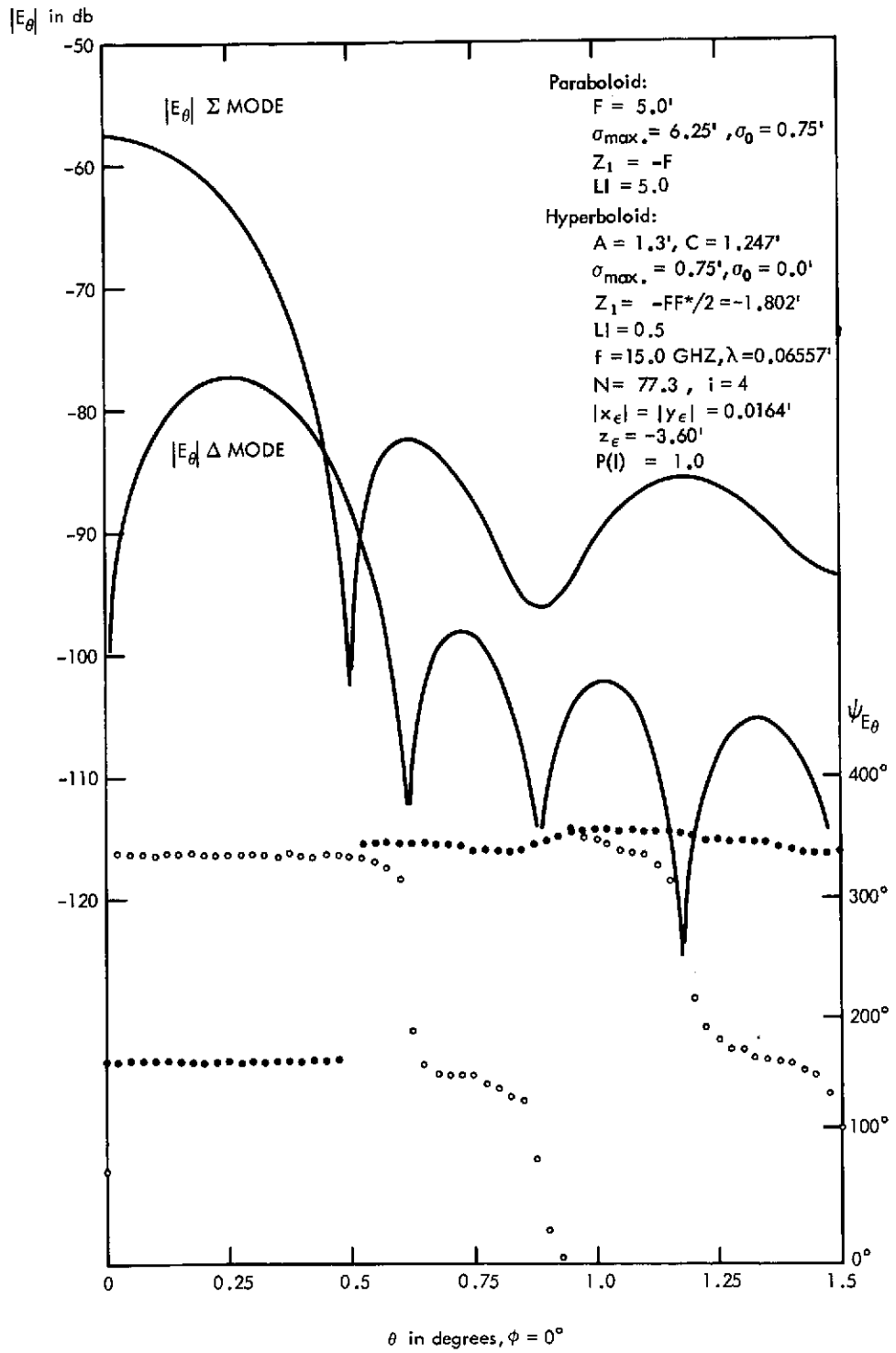

Figure 20. Tracking patterns, Σ and Δ modes (N = 77.3).

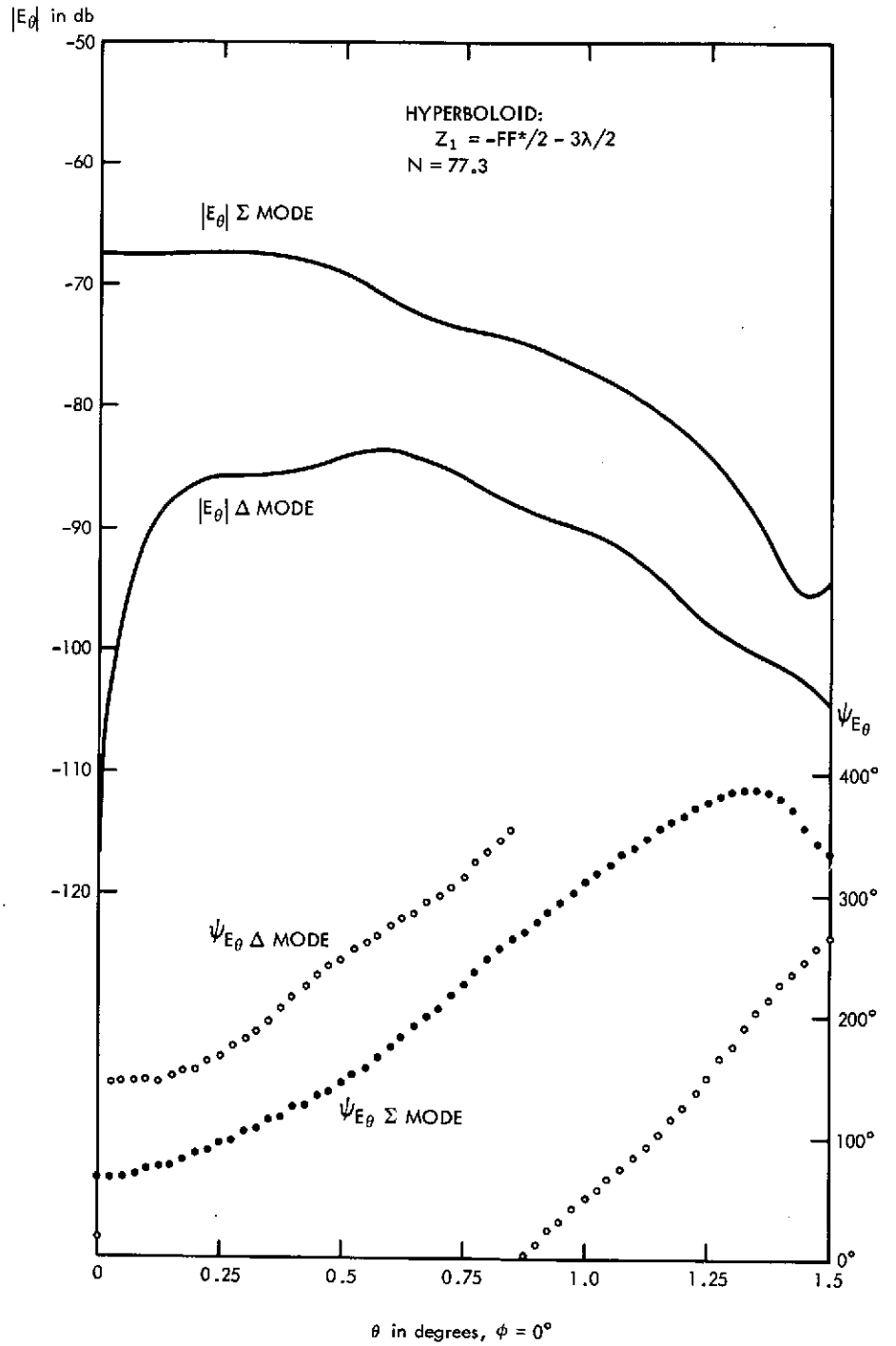

Figure 21. Acquisition patterns, Σ and Δ modes (N = 77.3) for $\Delta Z = -3\lambda/2$ of hyperboloid.

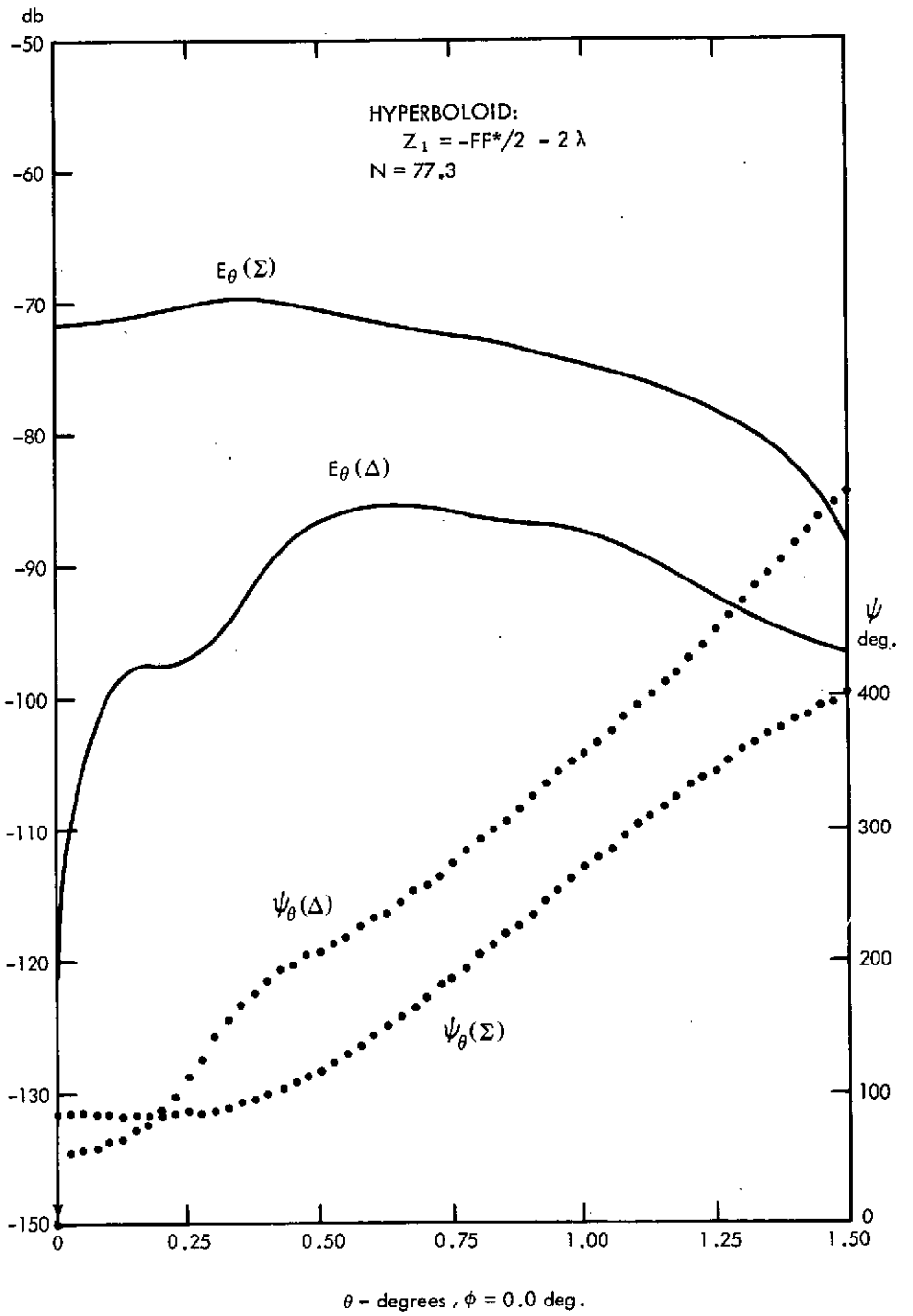

Figure 22. Acquisition patterns, Σ and Δ modes (N = 77.3) for $\Delta Z = -2\lambda$ of hyperboloid.

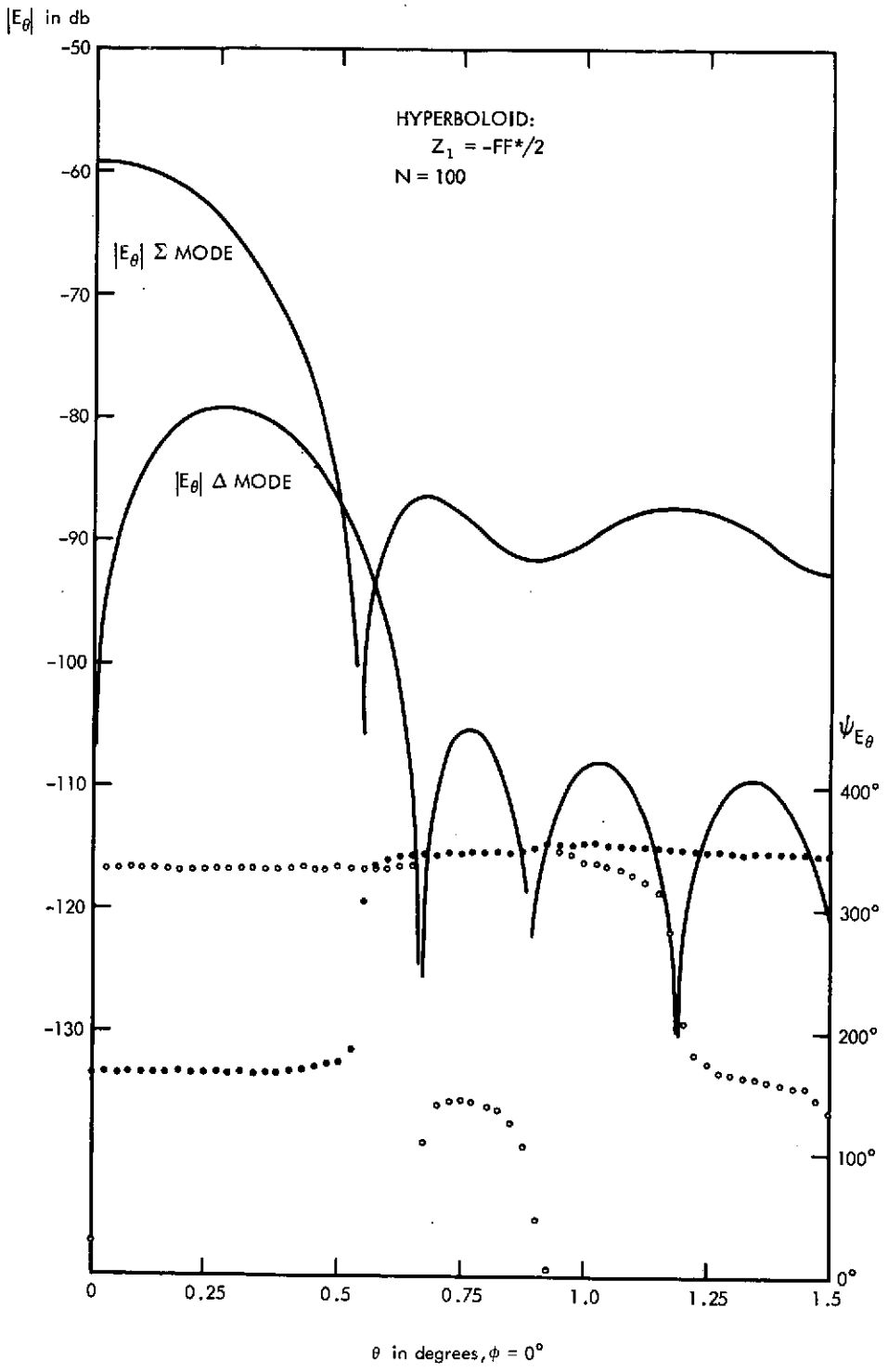

Figure 23. Tracking patterns, Σ and Δ modes (N = 100).

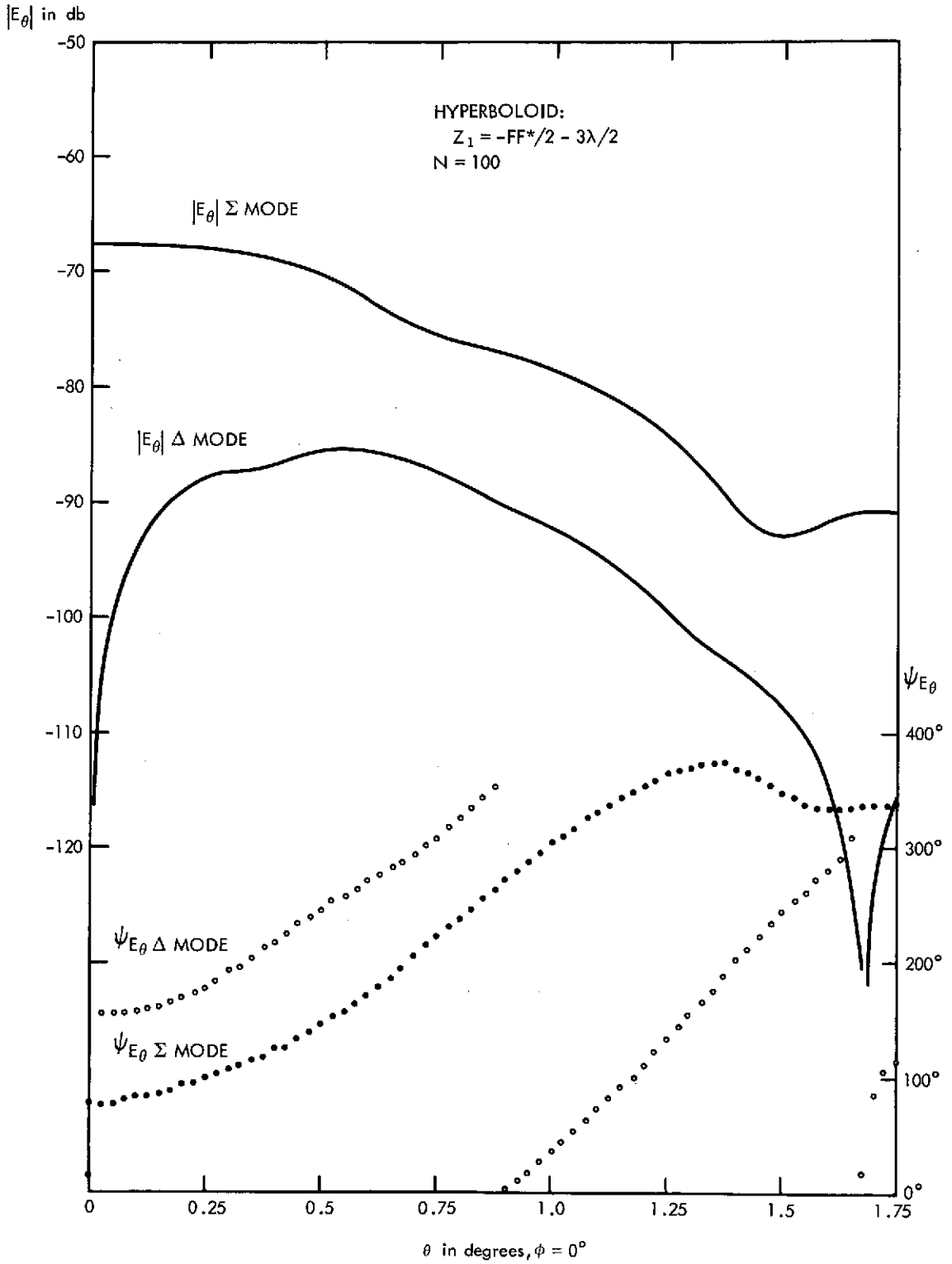

Figure 24. Acquisition patterns, Σ and Δ modes (N = 100) for $\Delta Z = -3\lambda/2$.

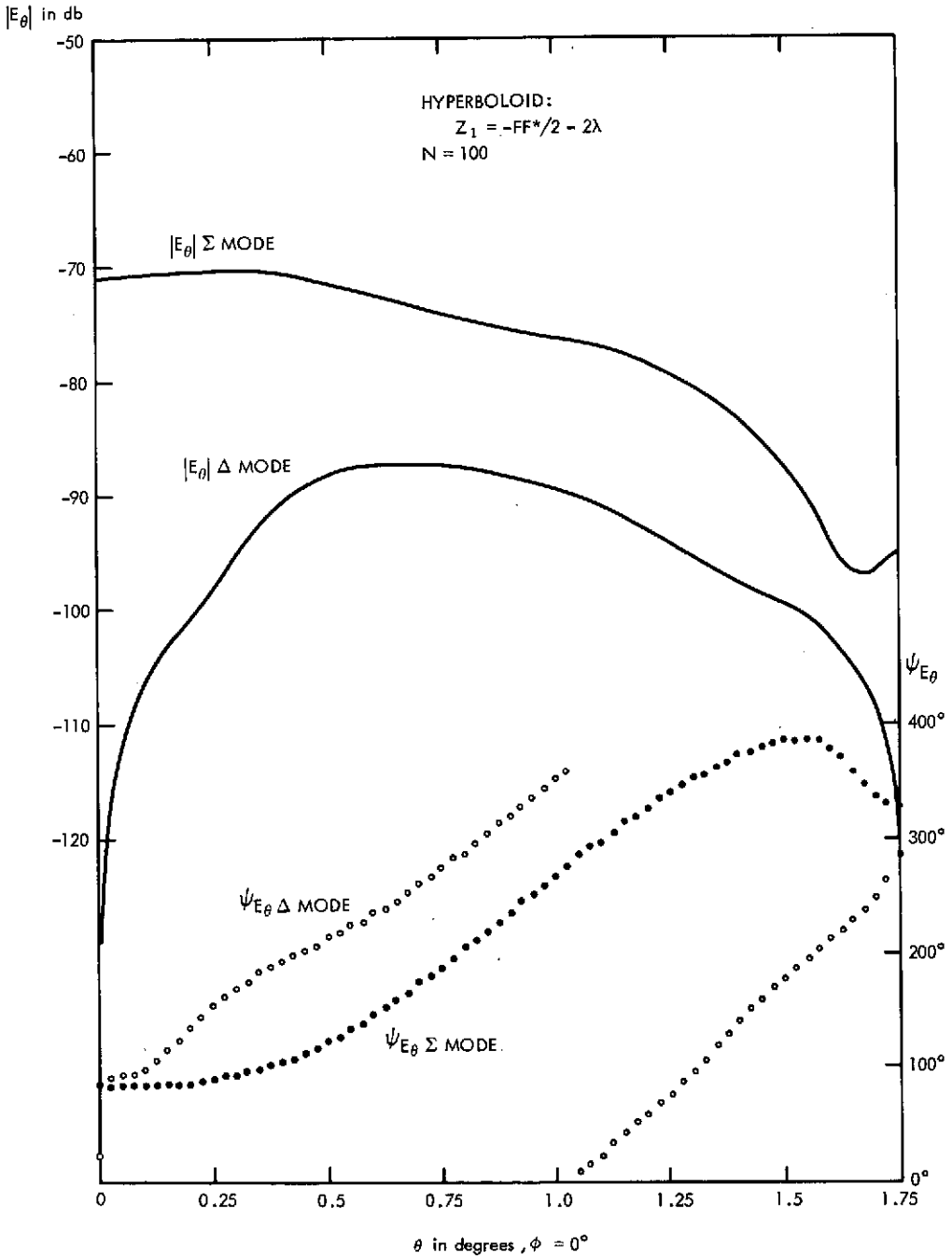

Figure 25. Acquisition patterns, Σ and Δ modes (N = 100) for $\Delta Z = -2\lambda$.

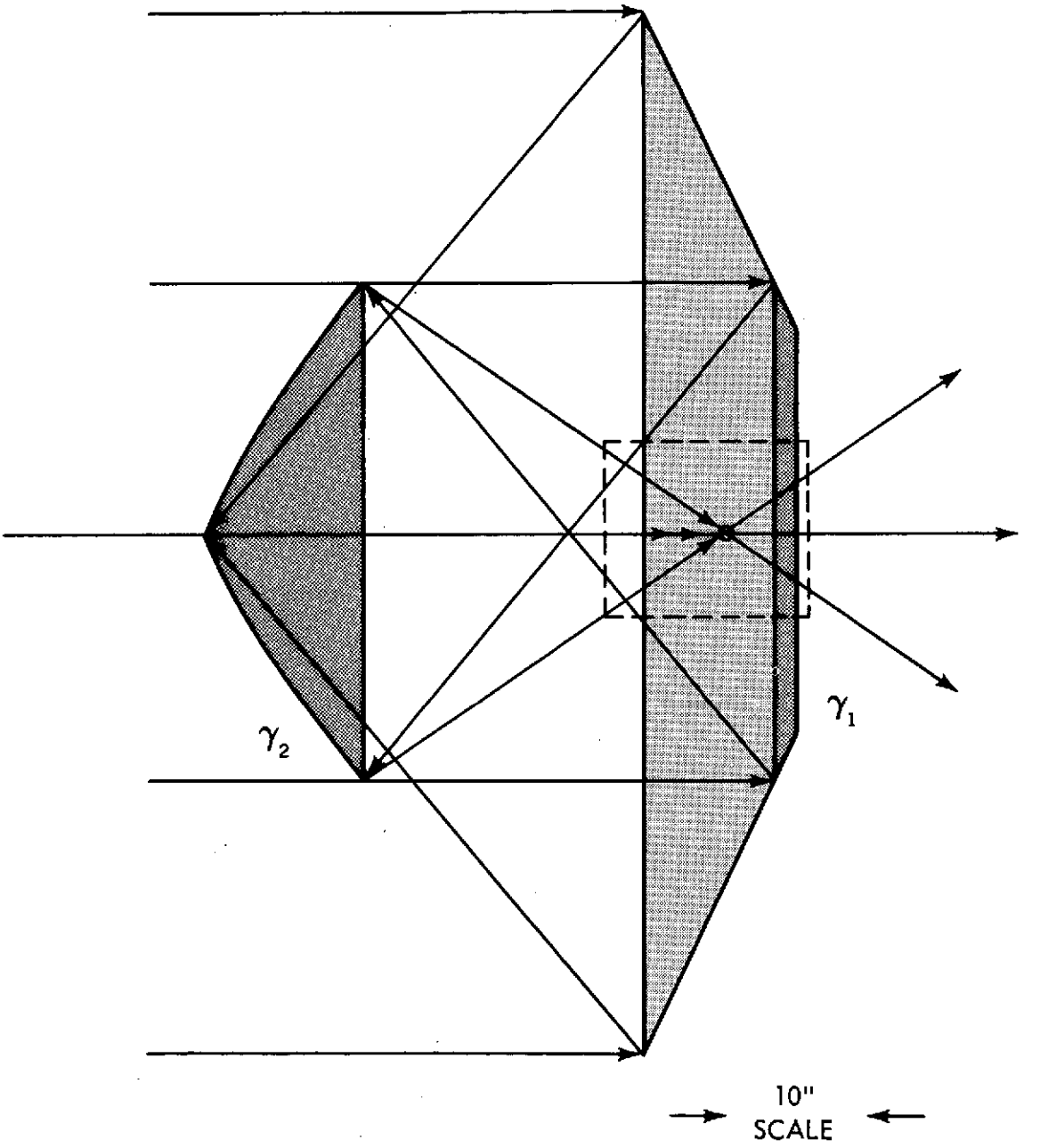

Figure 26. Conical-Gregorian geometry with spiral antenna feed.

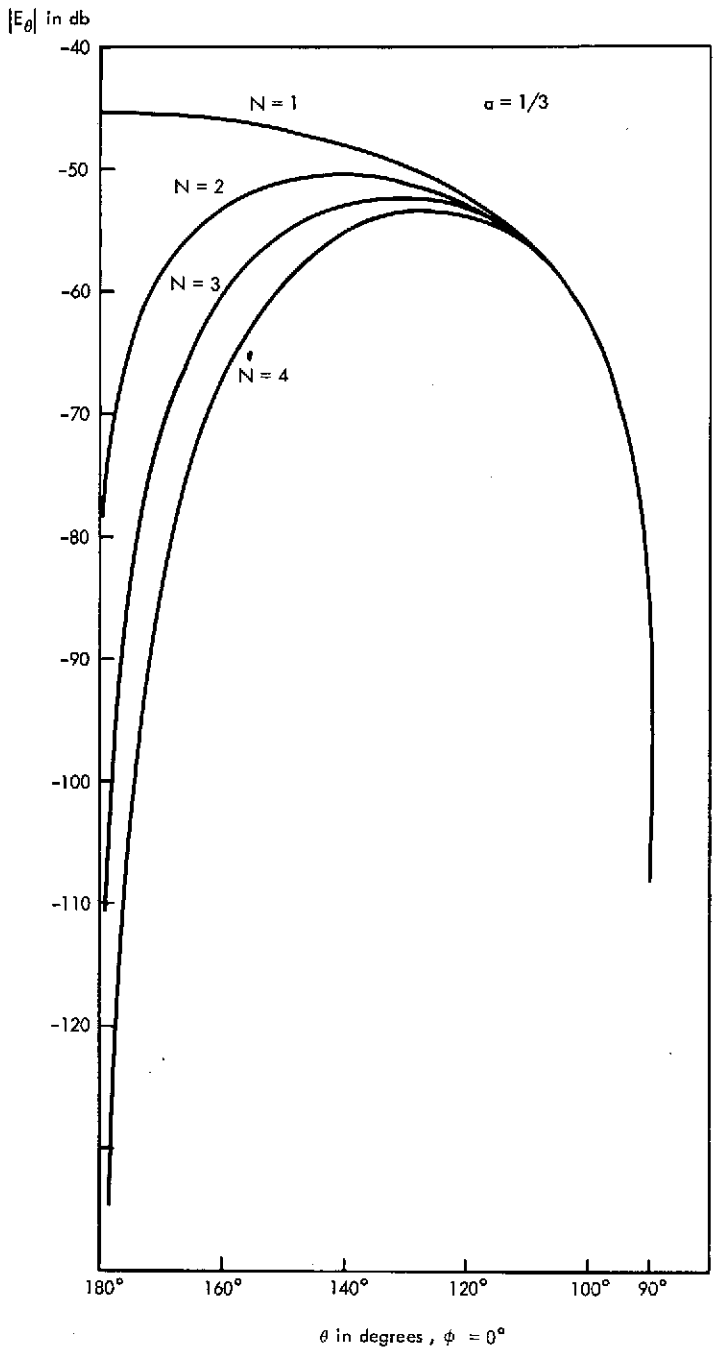

Figure 27. Primary radiation patterns of spiral antenna (a = 1/3, n = 1, 2, 3, 4).

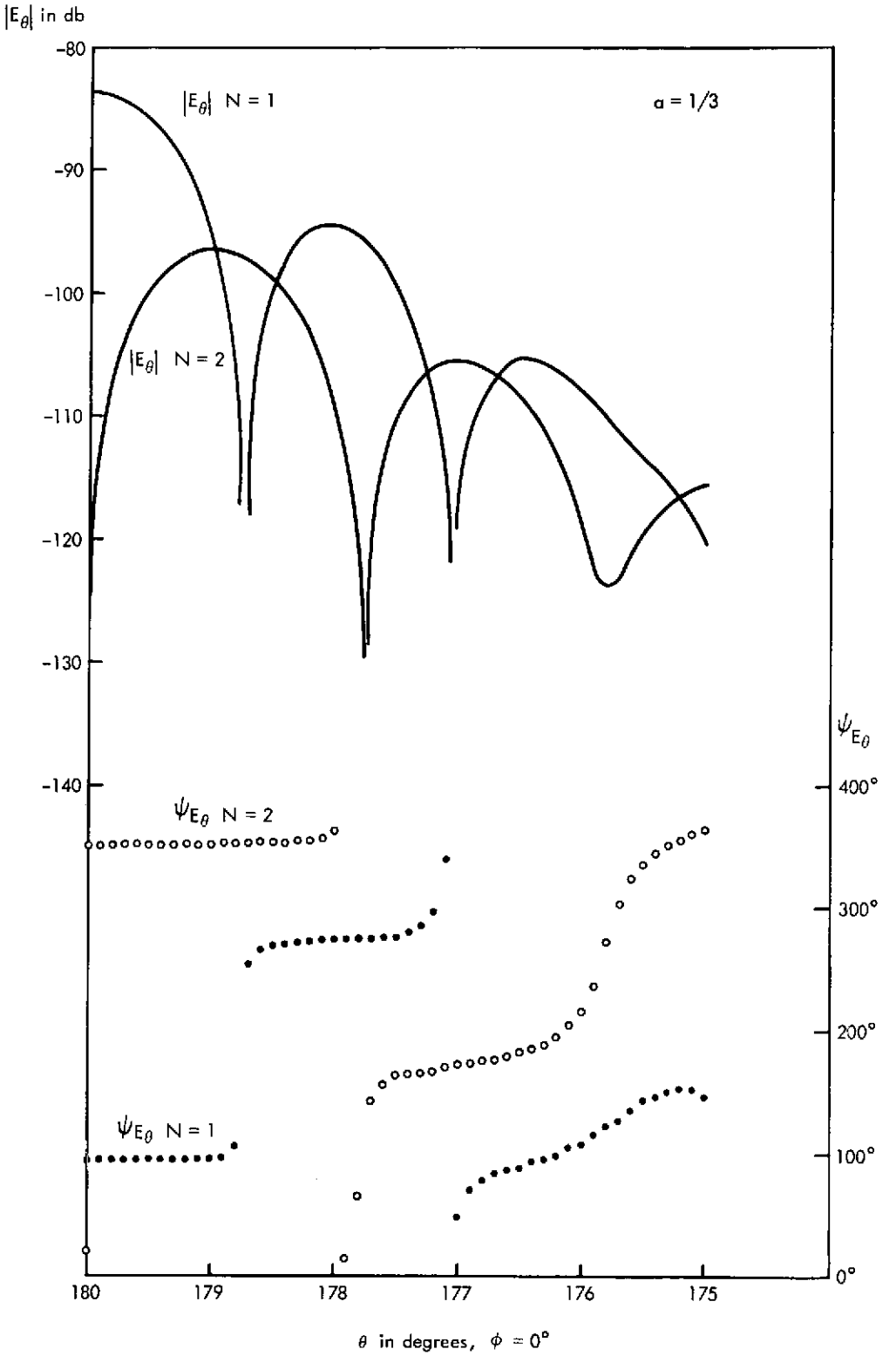

Figure 28. Tracking patterns, Σ and Δ modes, of the Conical Gregorian System (a = 1/3, n = 1, 2).

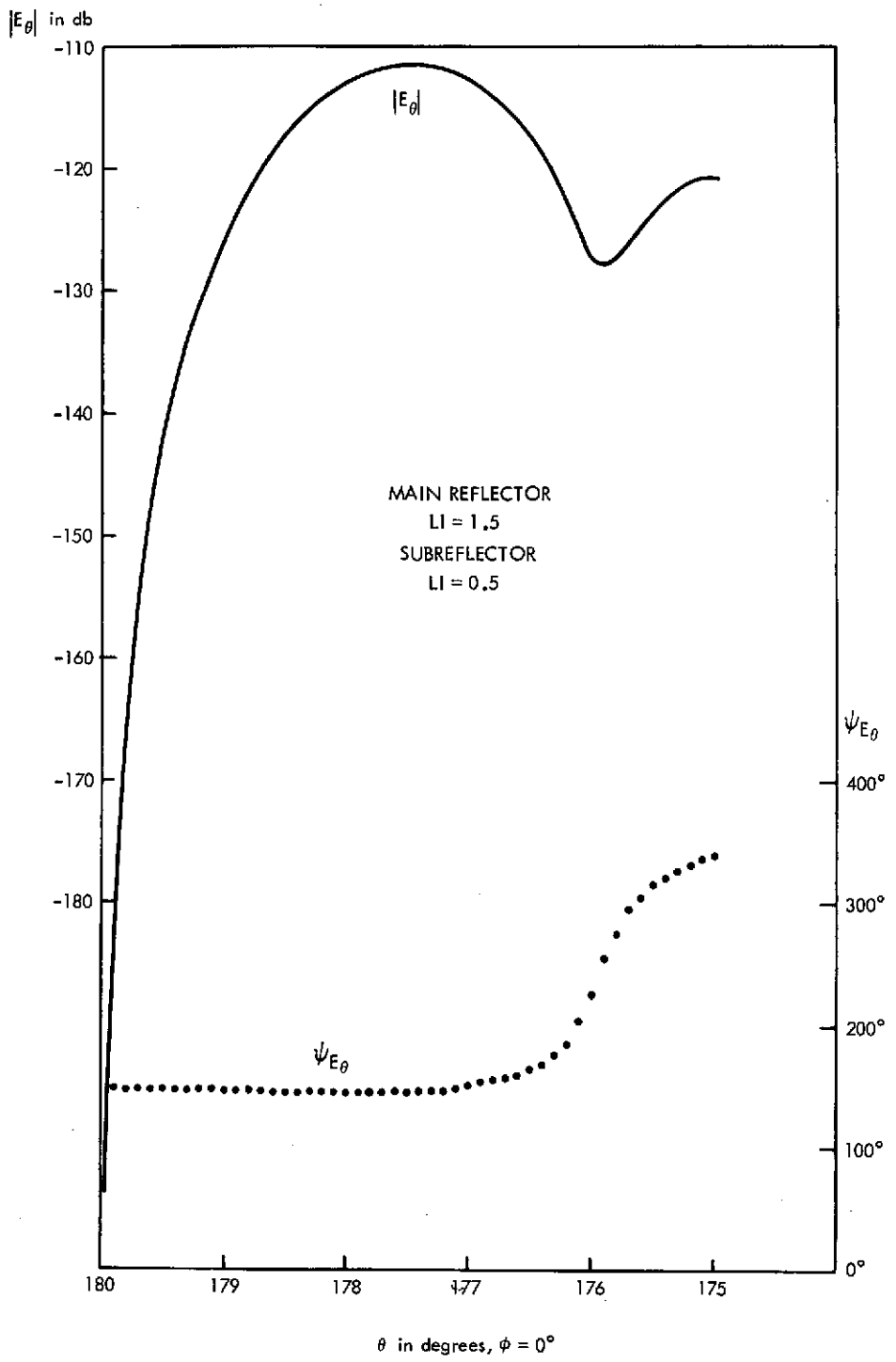

Figure 29. Acquisition pattern, Δ mode, of the Conical Gregorian System (a = 1/3, n = 4).

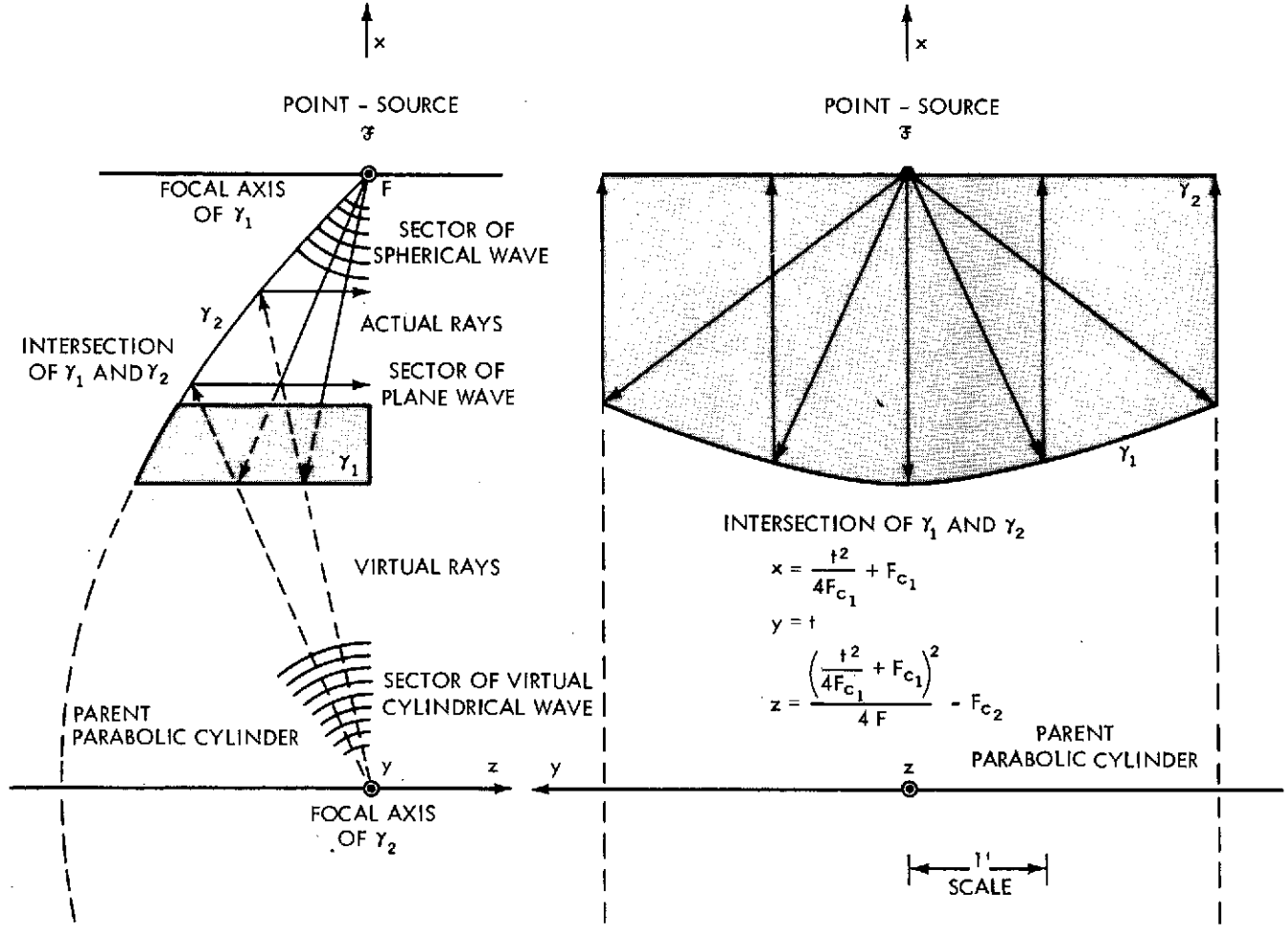

Figure 30. Dual parabolic cylinder geometry.

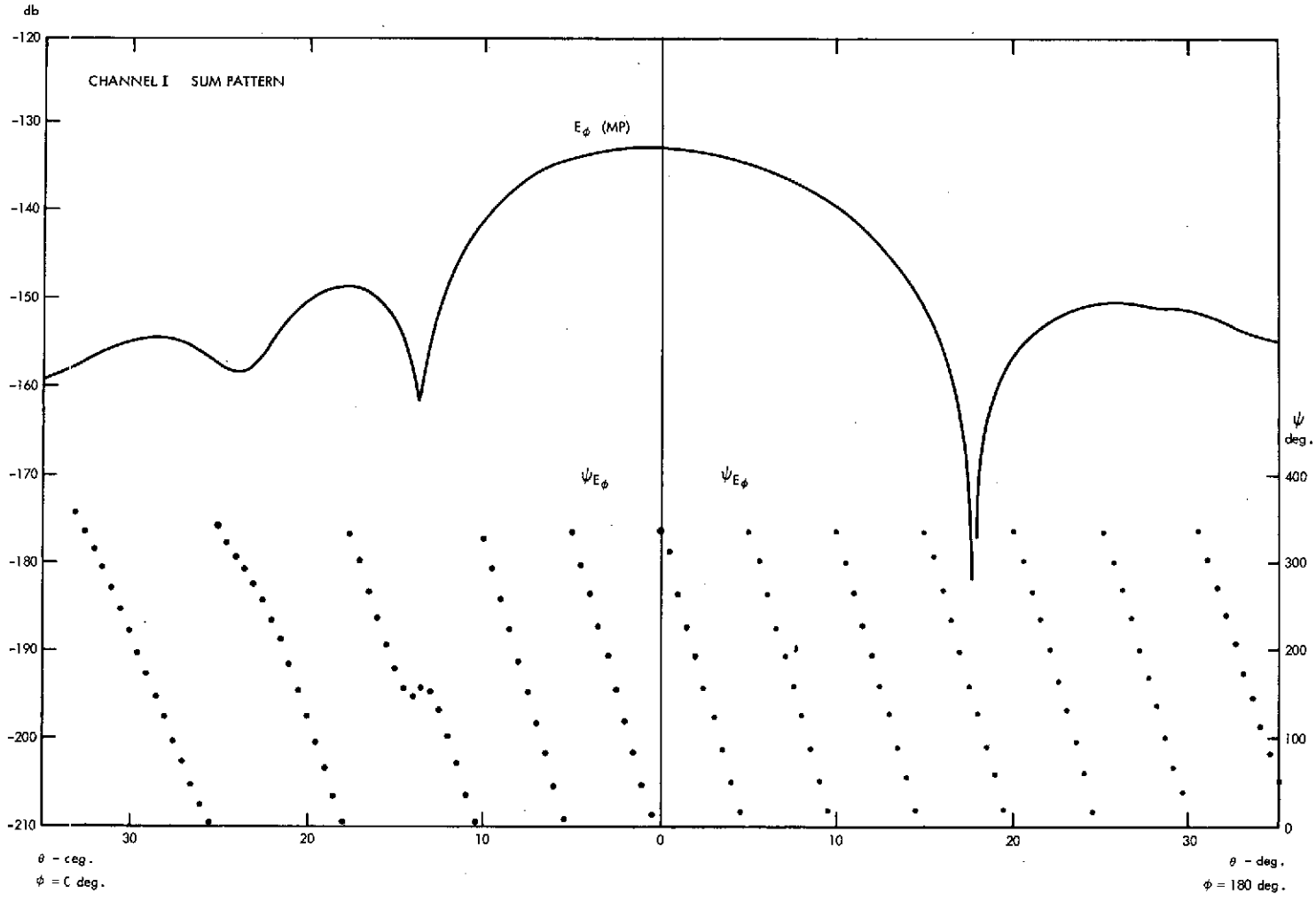

Figure 31. Acquisition pattern, Channel I (Σ).

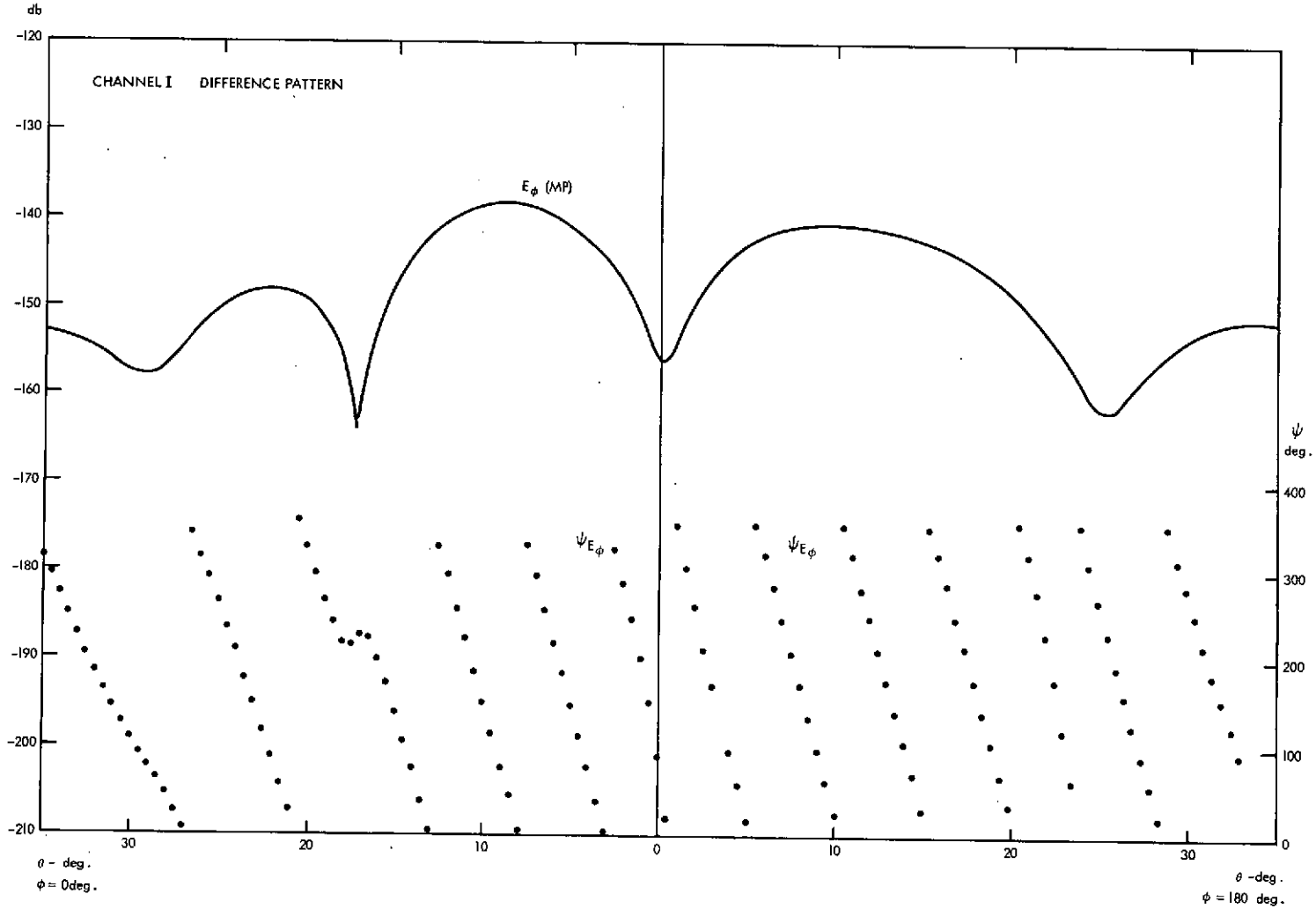

Figure 32. Acquisition pattern, Channel I (Δ).

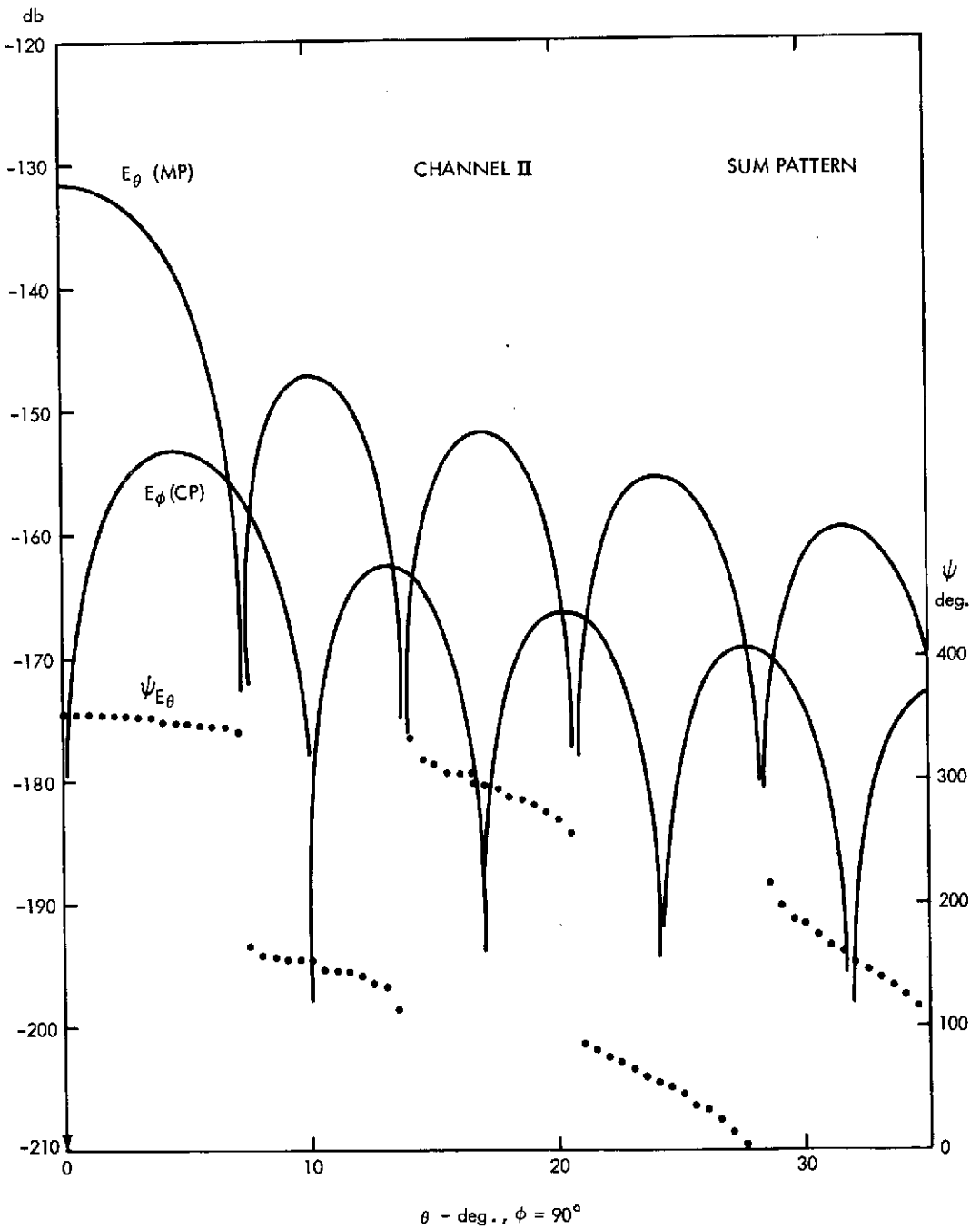

Figure 33. Acquisition pattern, Channel II (Σ).

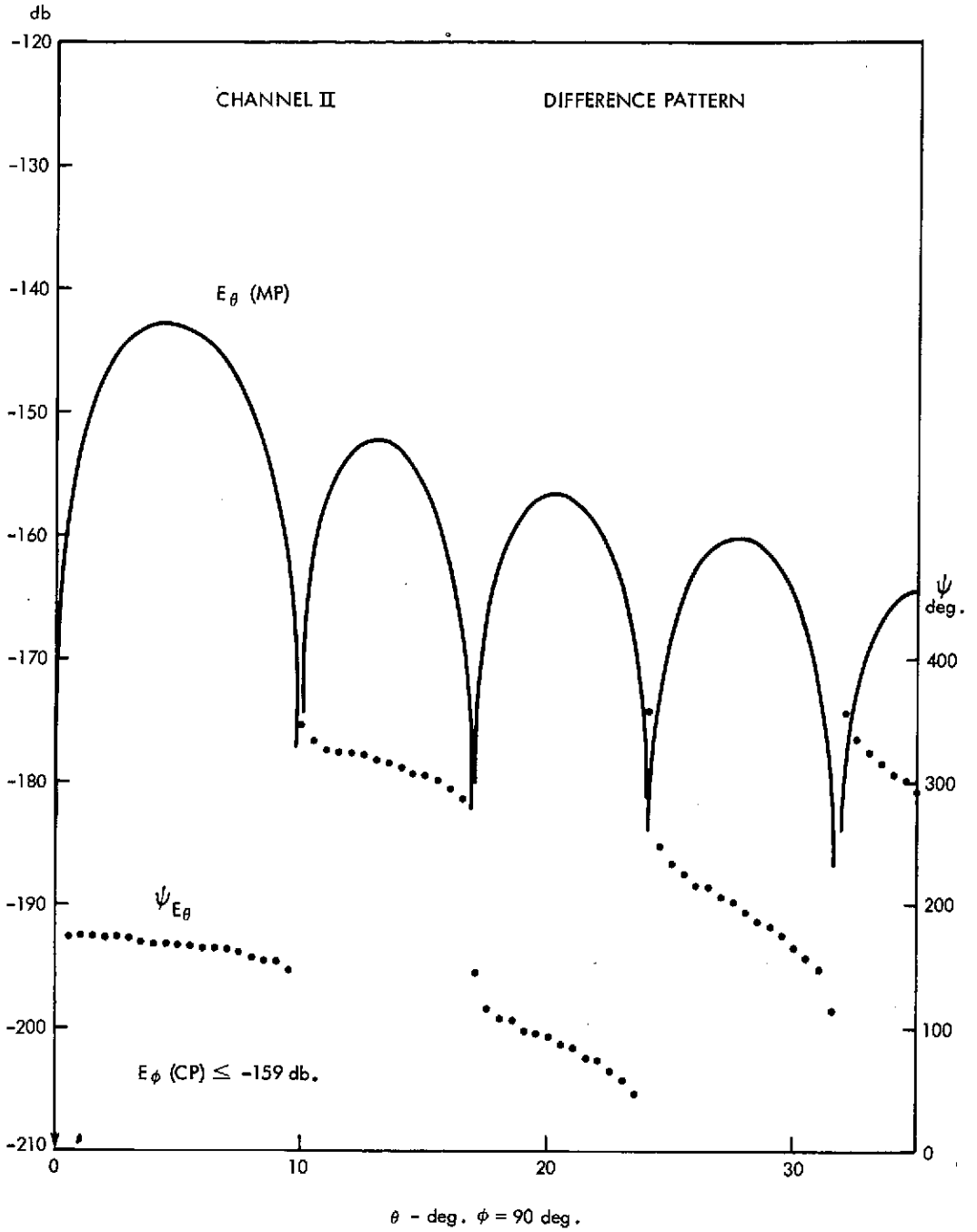

Figure 34. Acquisition pattern, Channel II (Δ).

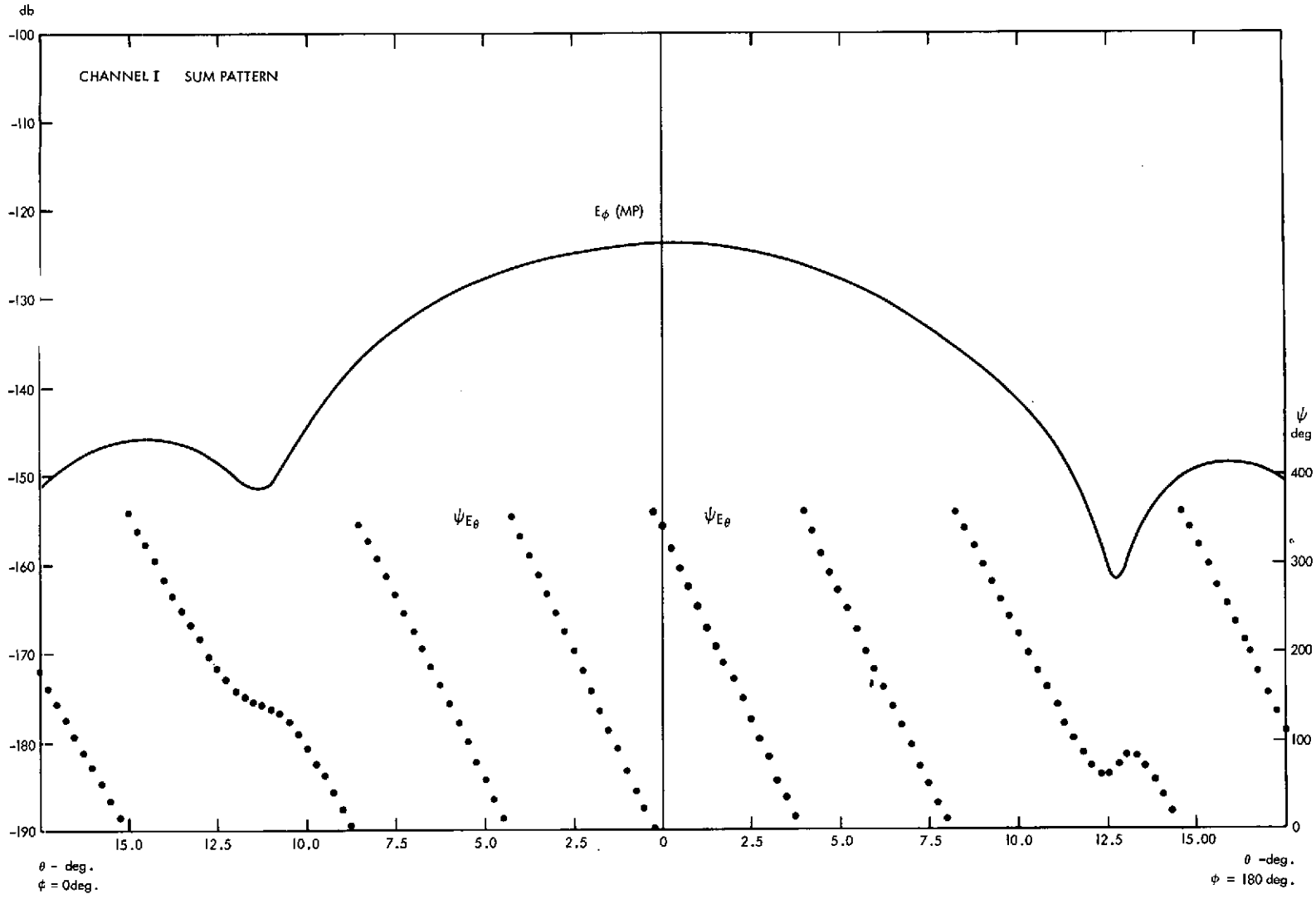

Figure 35. Tracking pattern, Channel I (Σ).

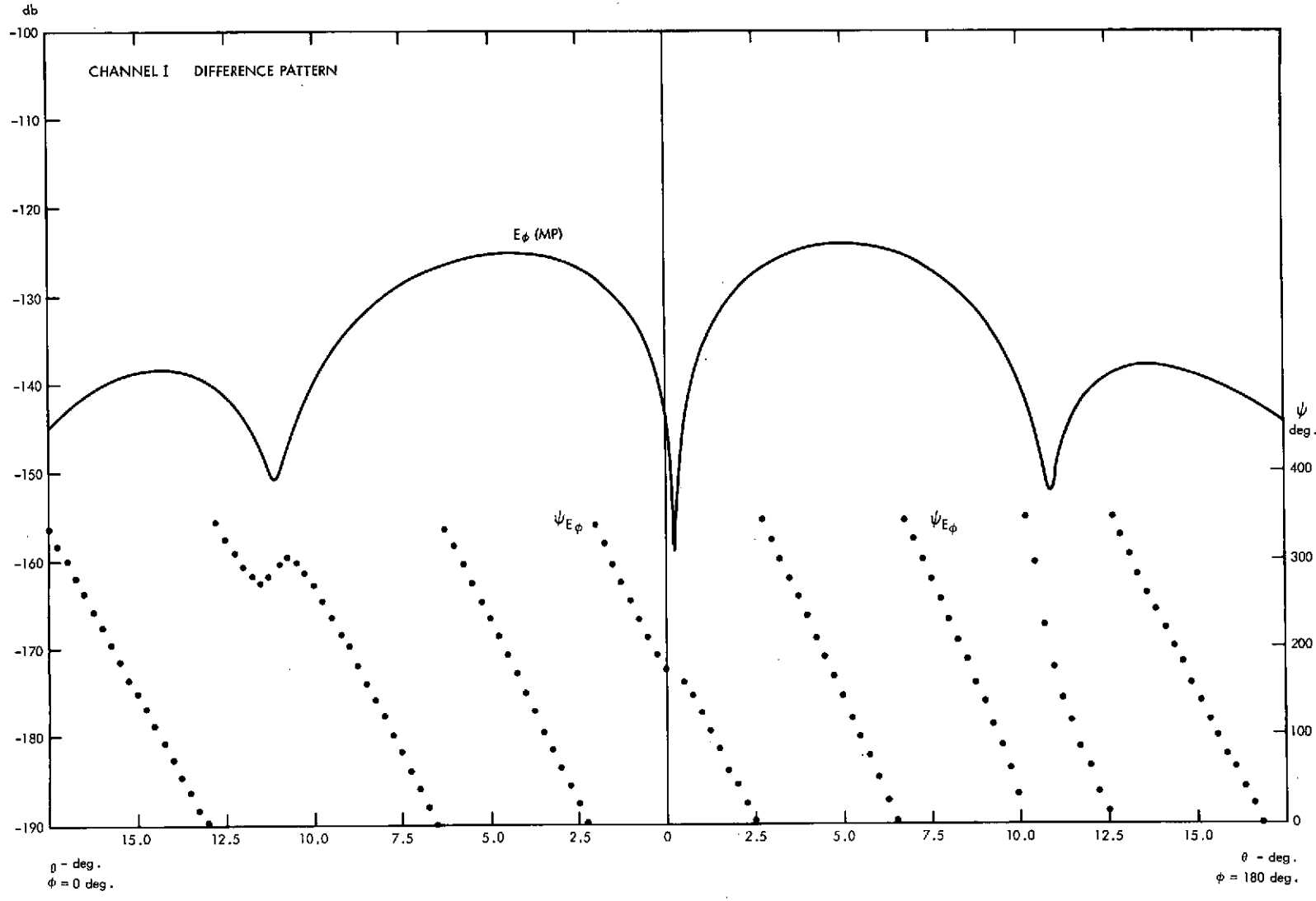

Figure 36. Tracking pattern, Channel I (Δ).

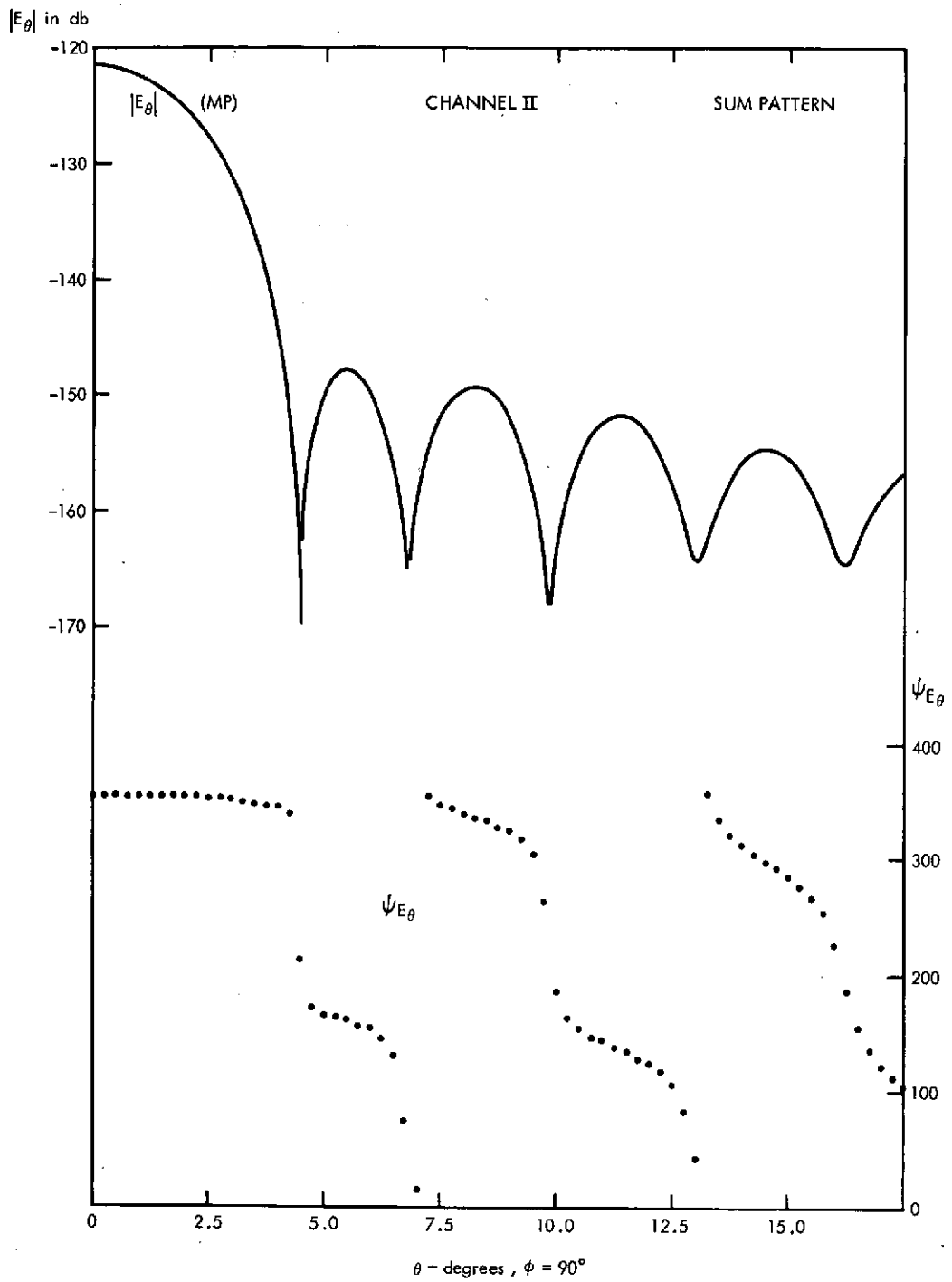

Figure 37. Tracking pattern, Channel II (Σ).

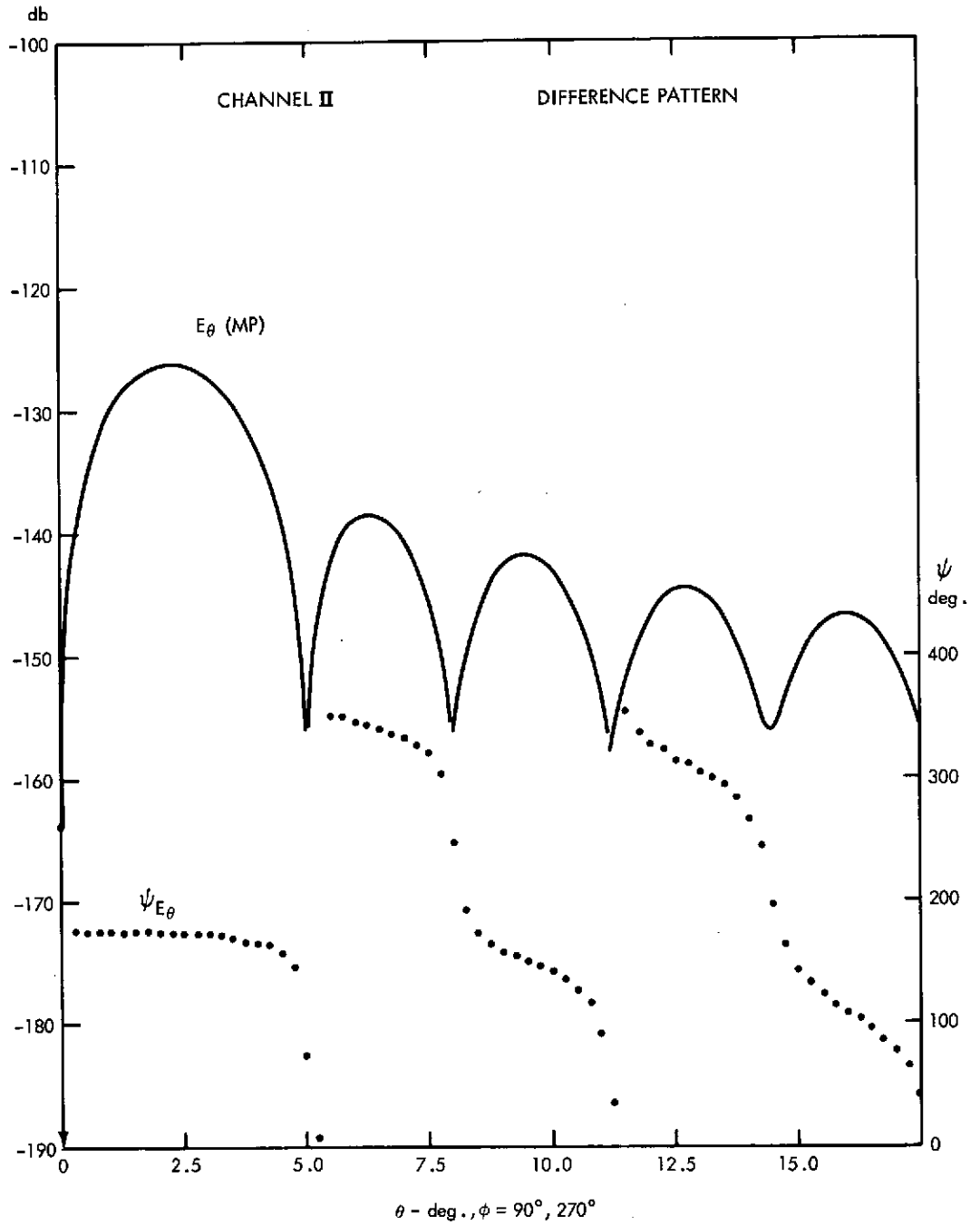

Figure 38. Tracking pattern, Channel II (Δ).

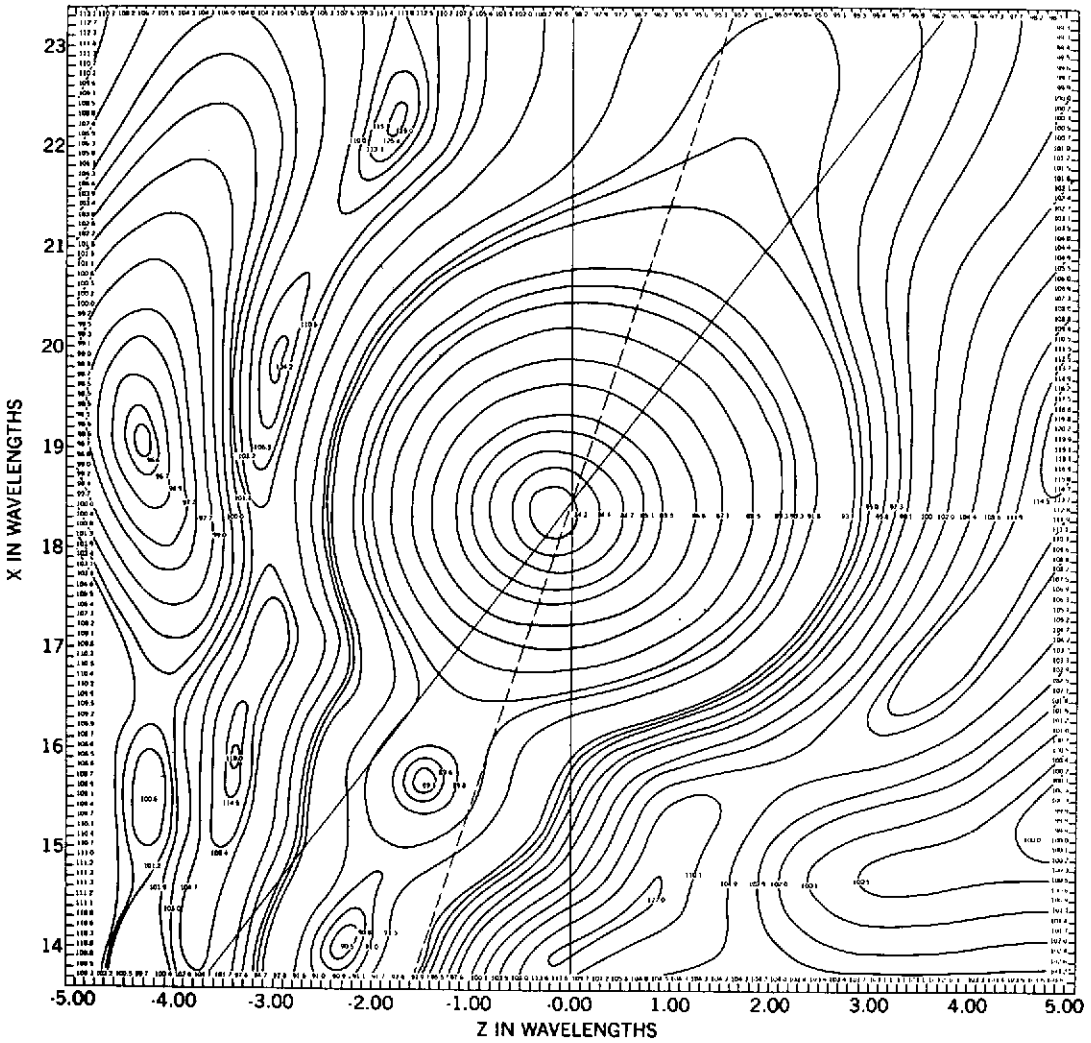

Figure 39. Electric-field distribution (ACQ).

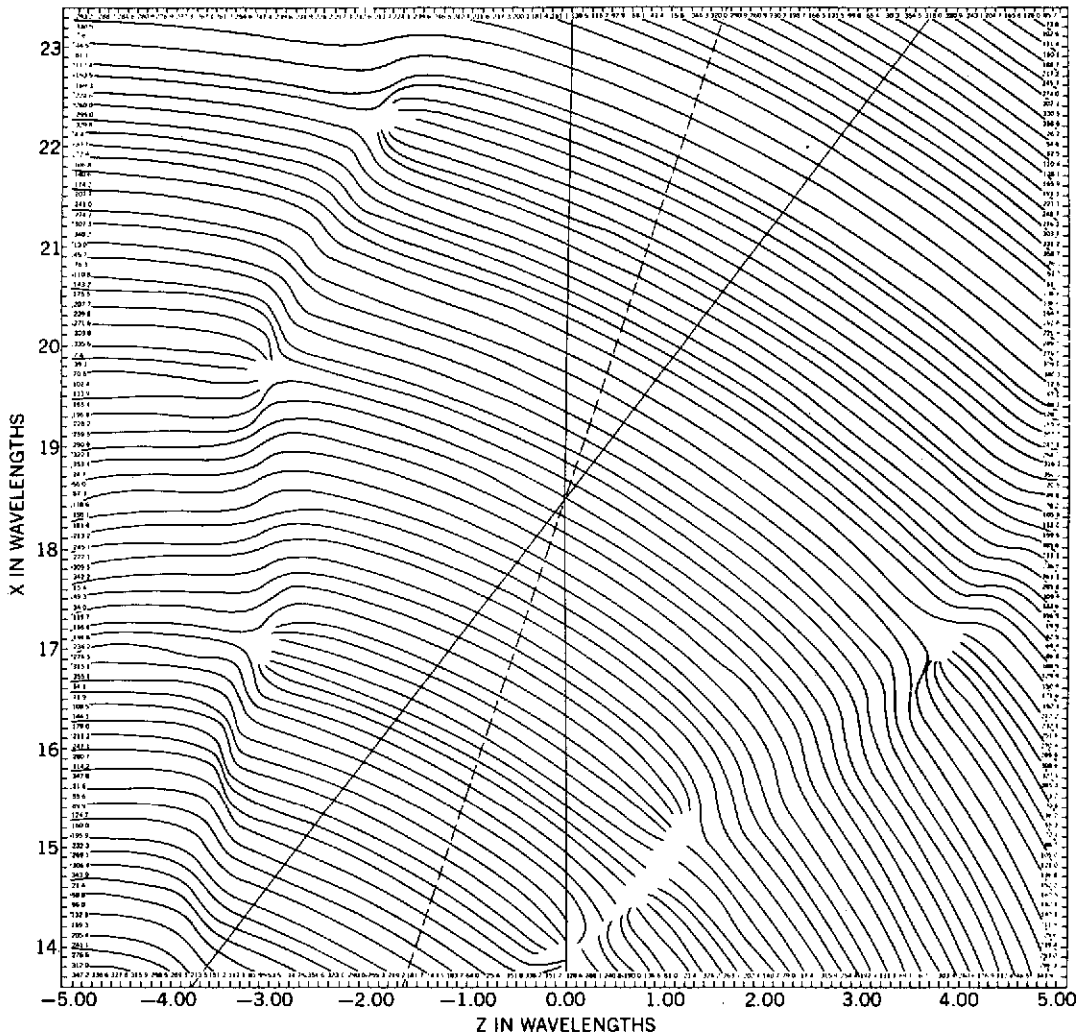

Figure 40. Wavefronts (ACQ).

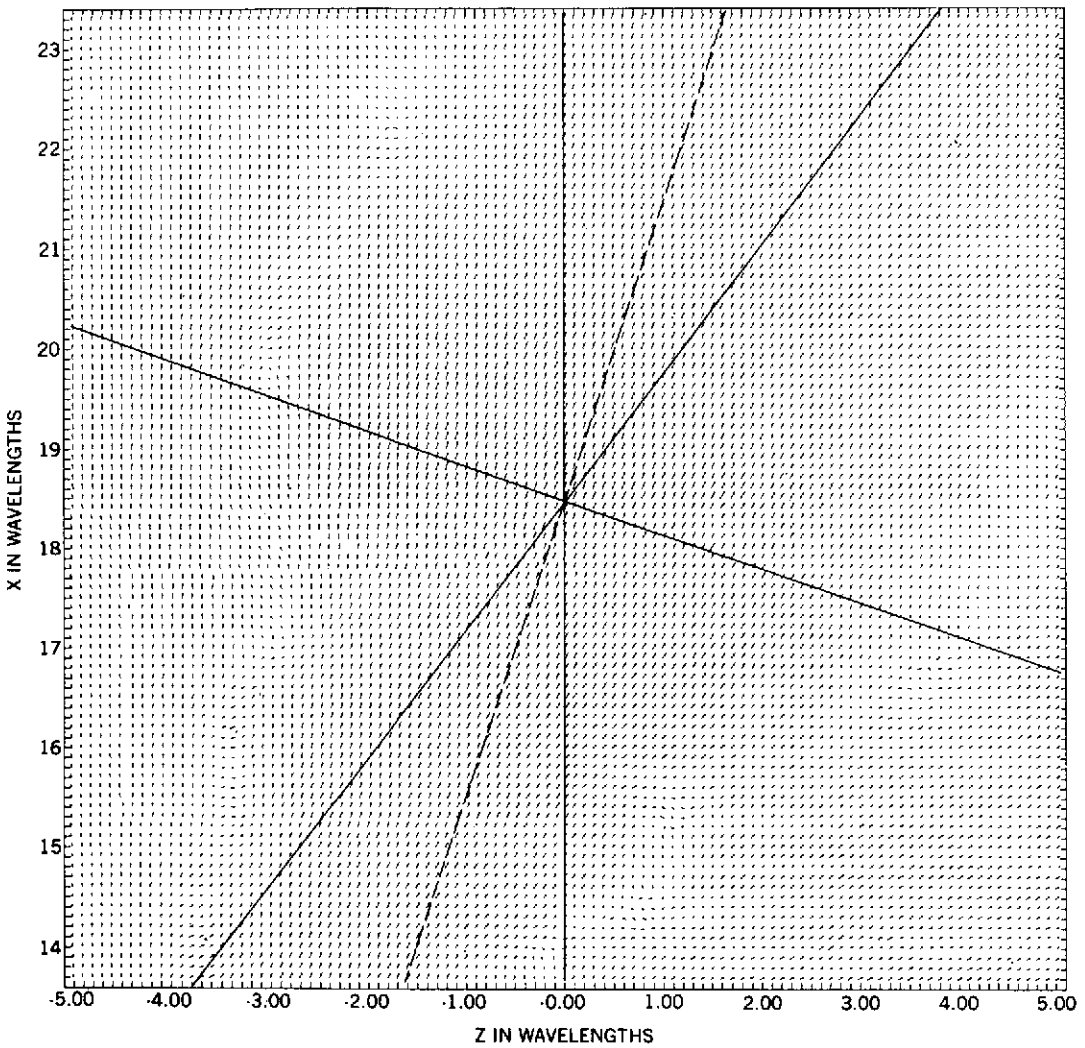

Figure 41. Time-average Poynting vectors (ACQ).

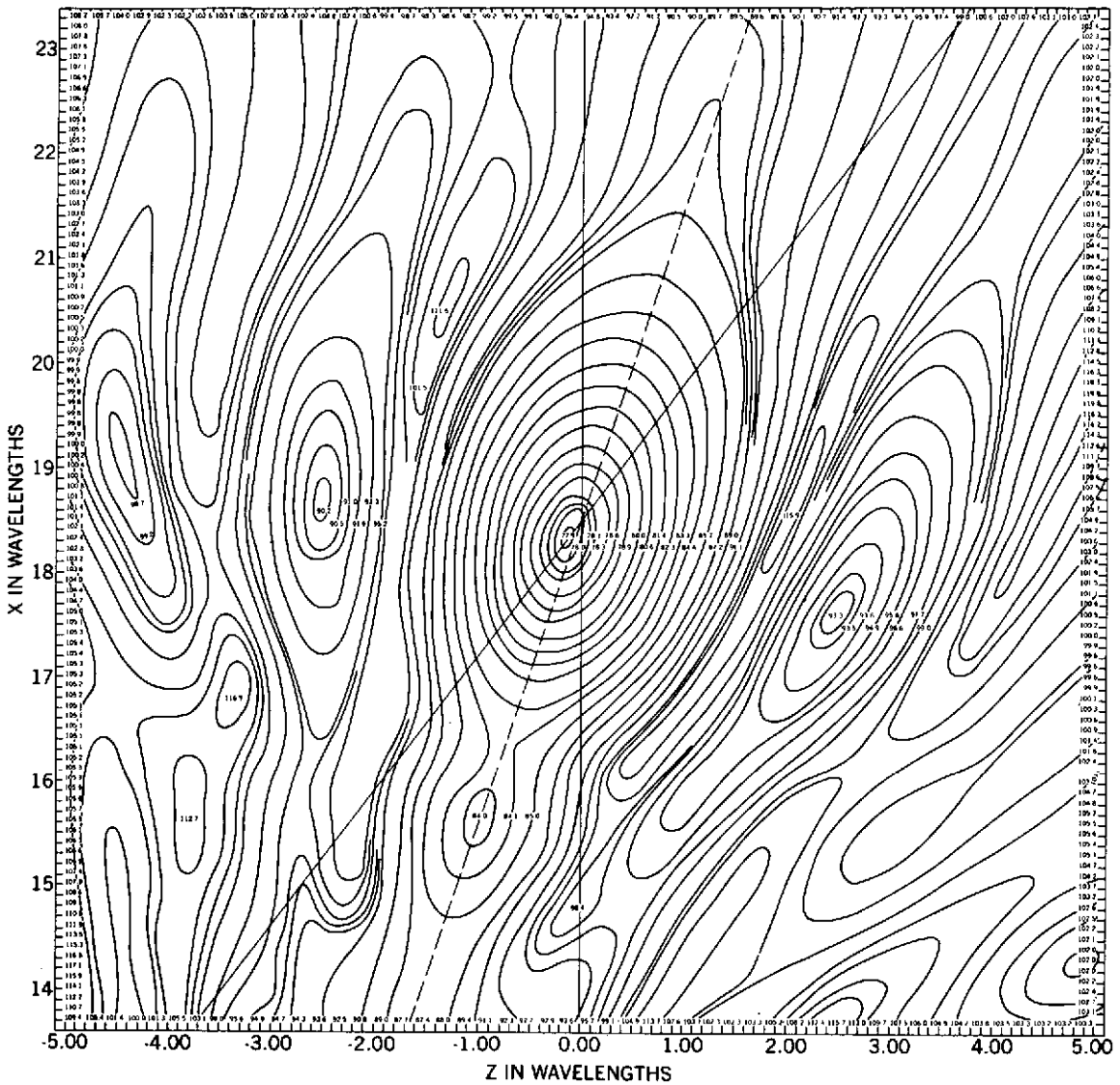

Figure 42. Electric-field distribution (TRK).

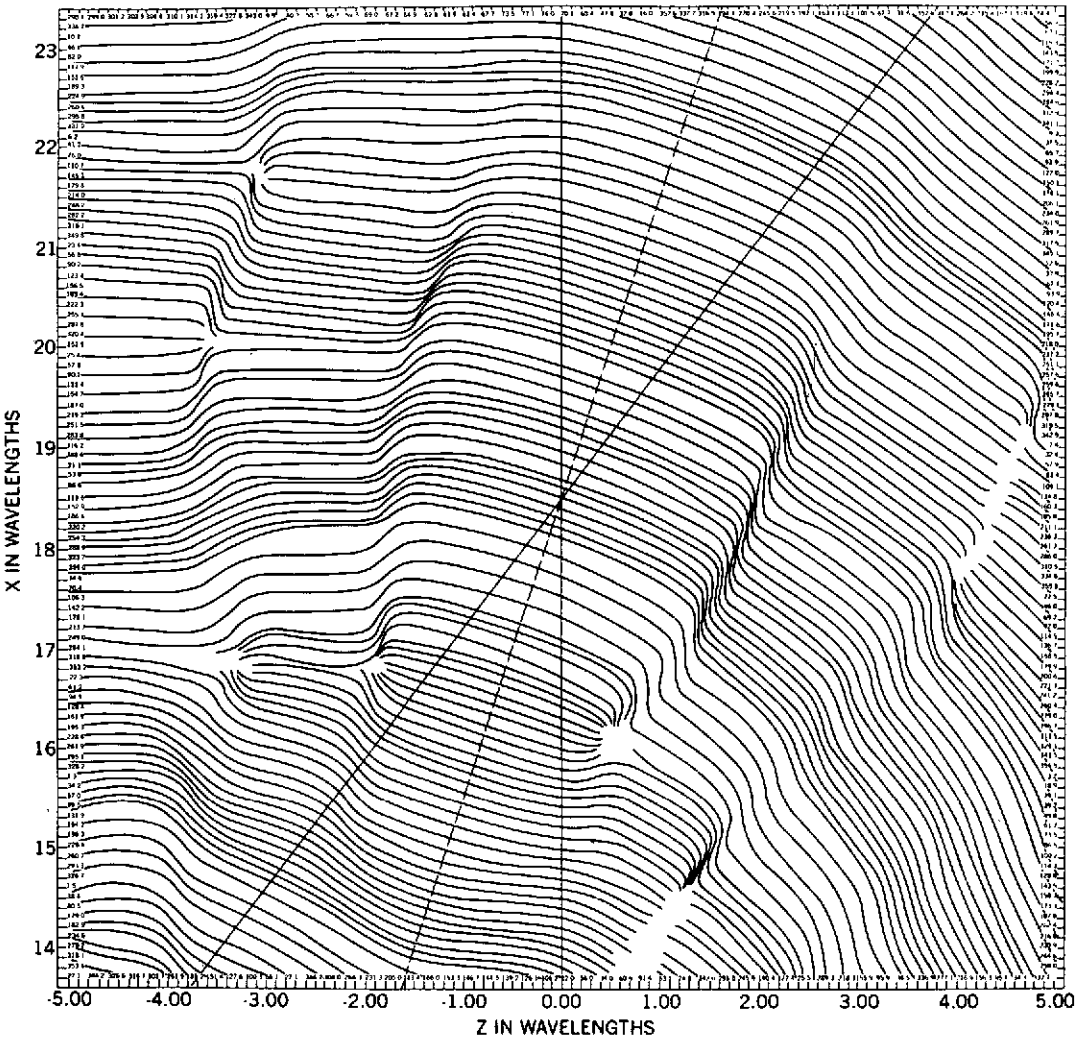

Figure 43. Wavefronts (TRK).

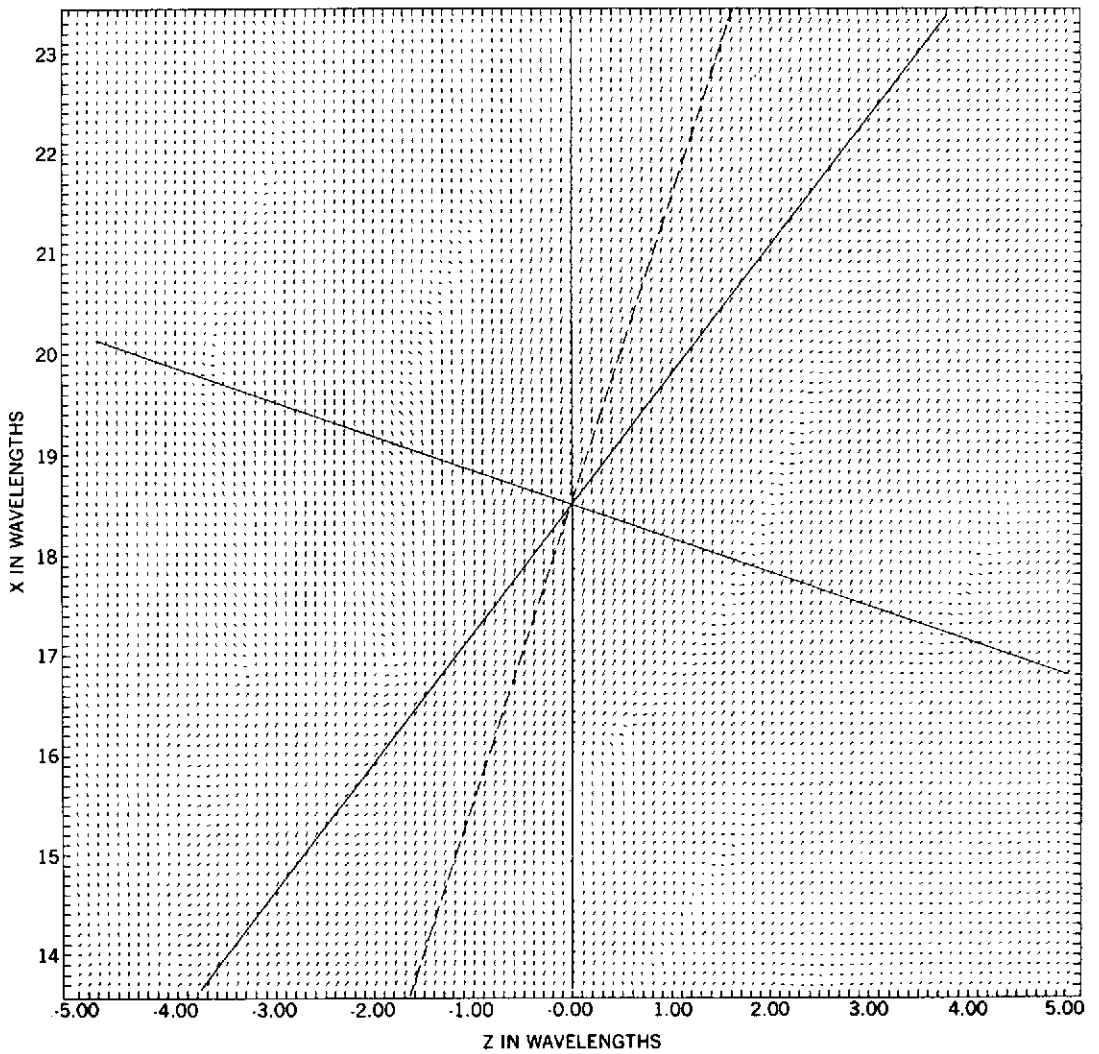

Figure 44. Time-average Poynting vectors (TRK).

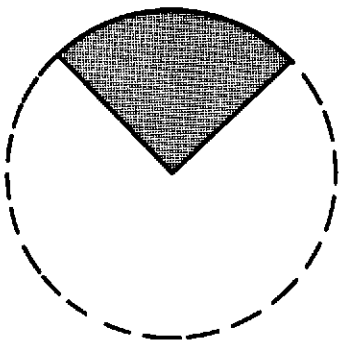

90° Sector

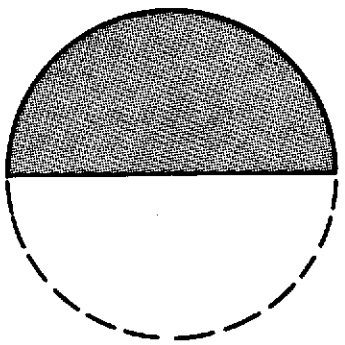

180° Sector

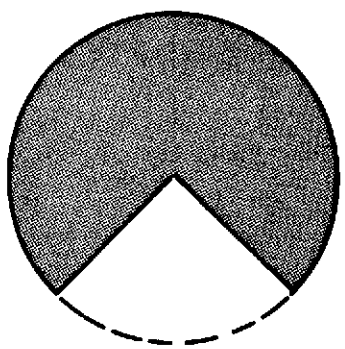

270° Sector

Figure 45. Telescoping-paraboloid geometry.

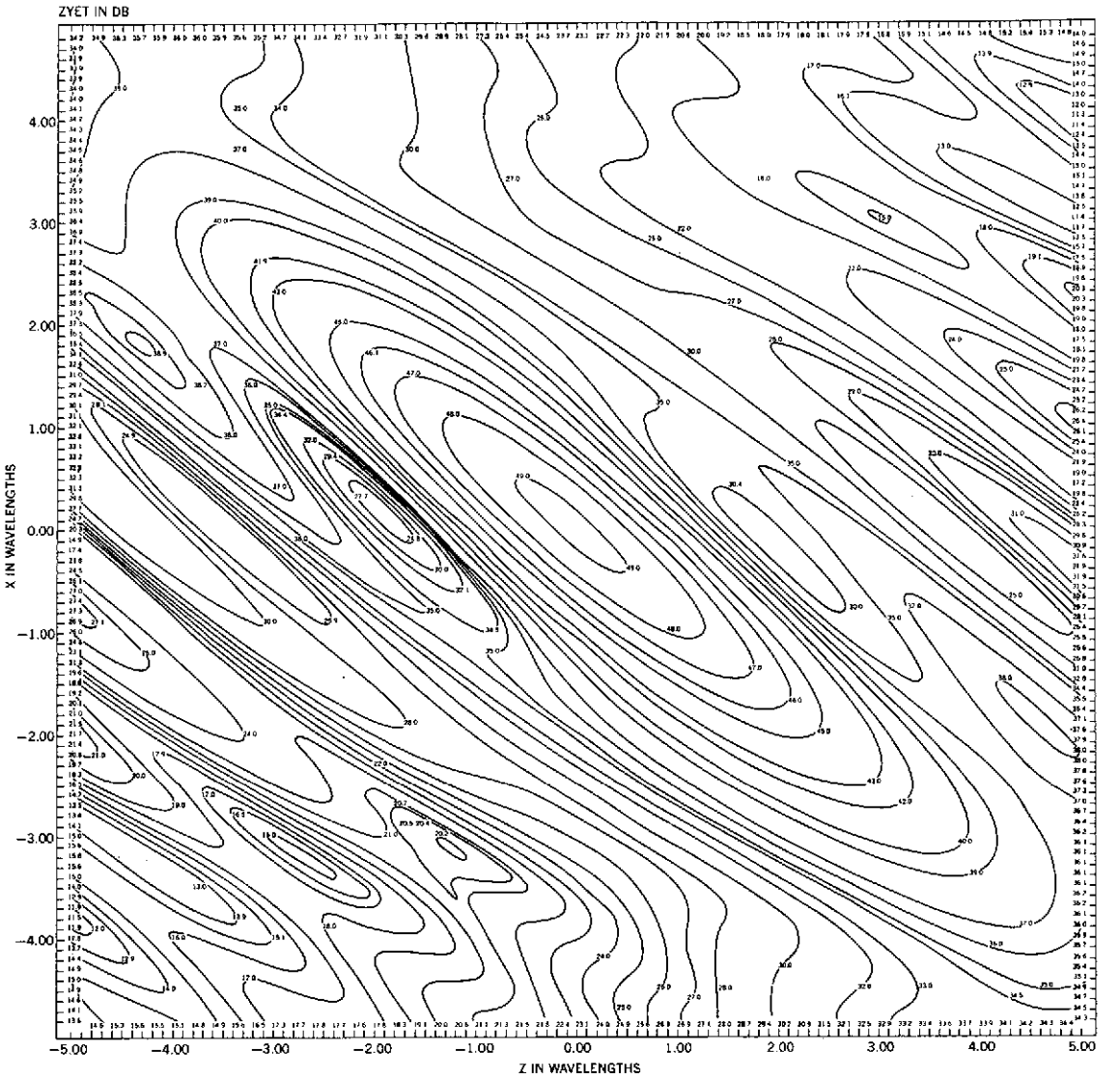

Figure 46. Electric-field distribution (ACQ).

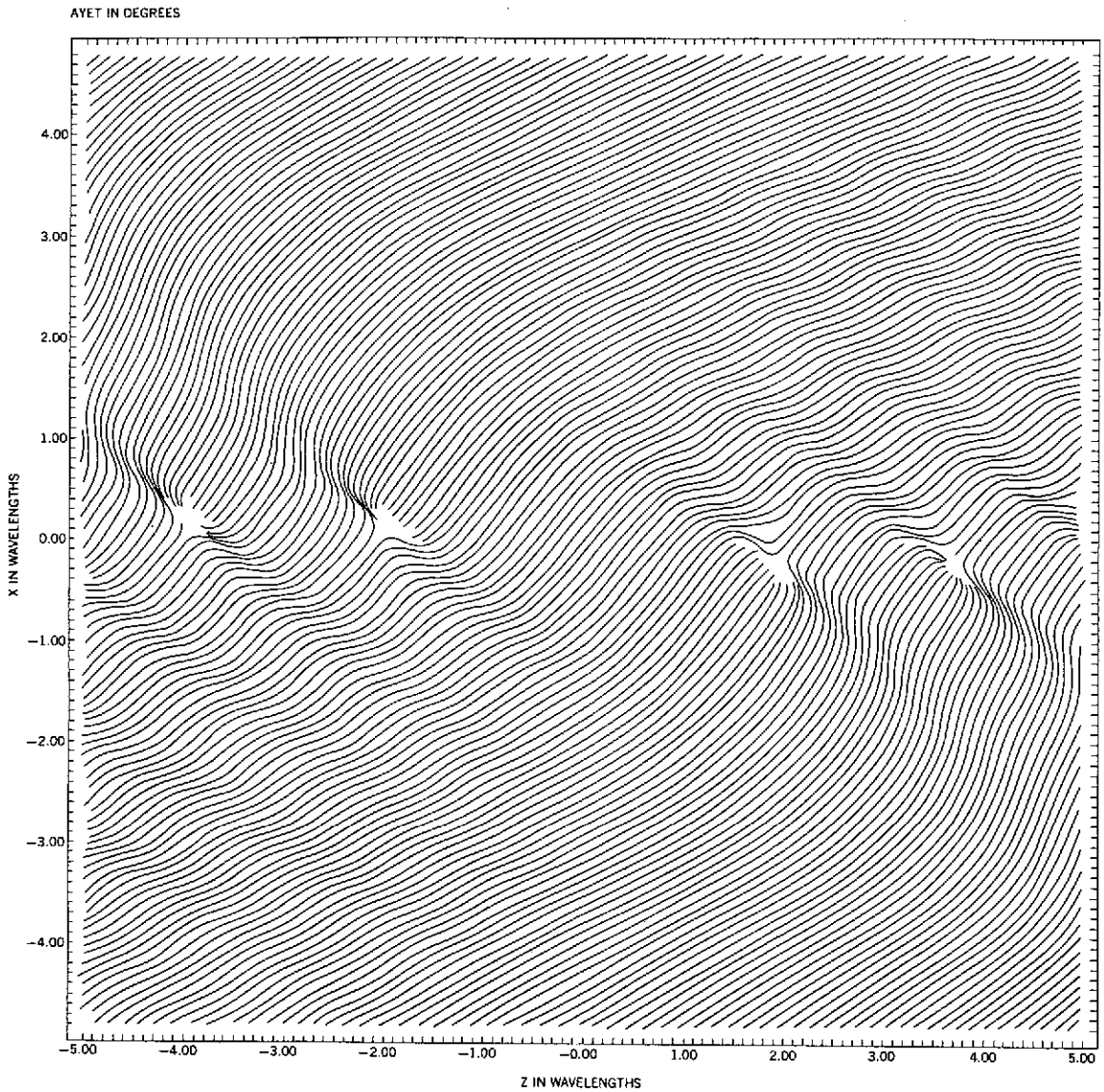

Figure 47. Wavefronts (ACQ).

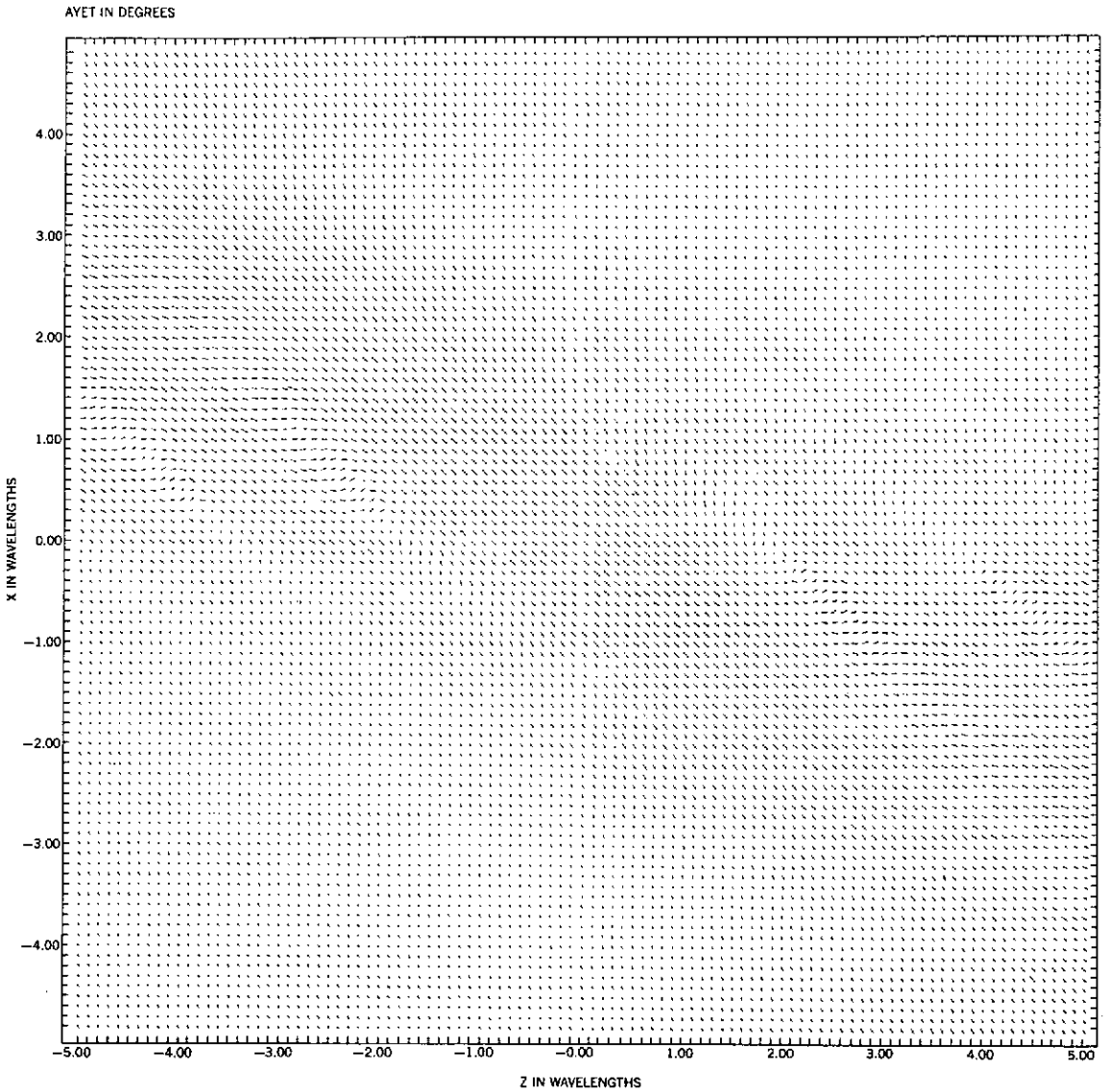

Figure 48. Time-average Poynting vectors (ACQ).

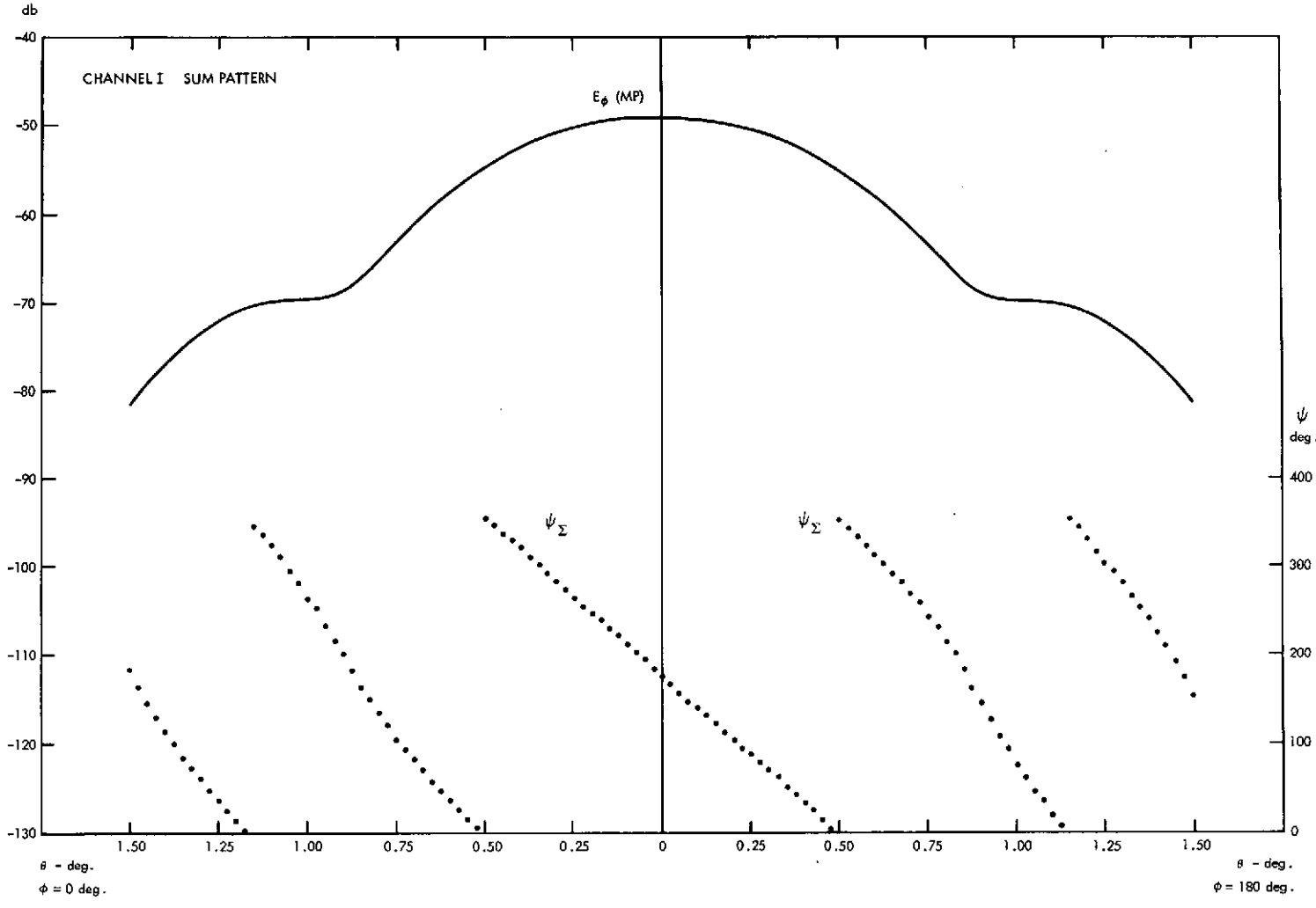

Figure 49. Acquisition pattern, Channel I (Σ) ($\phi = 0°, 180°$).

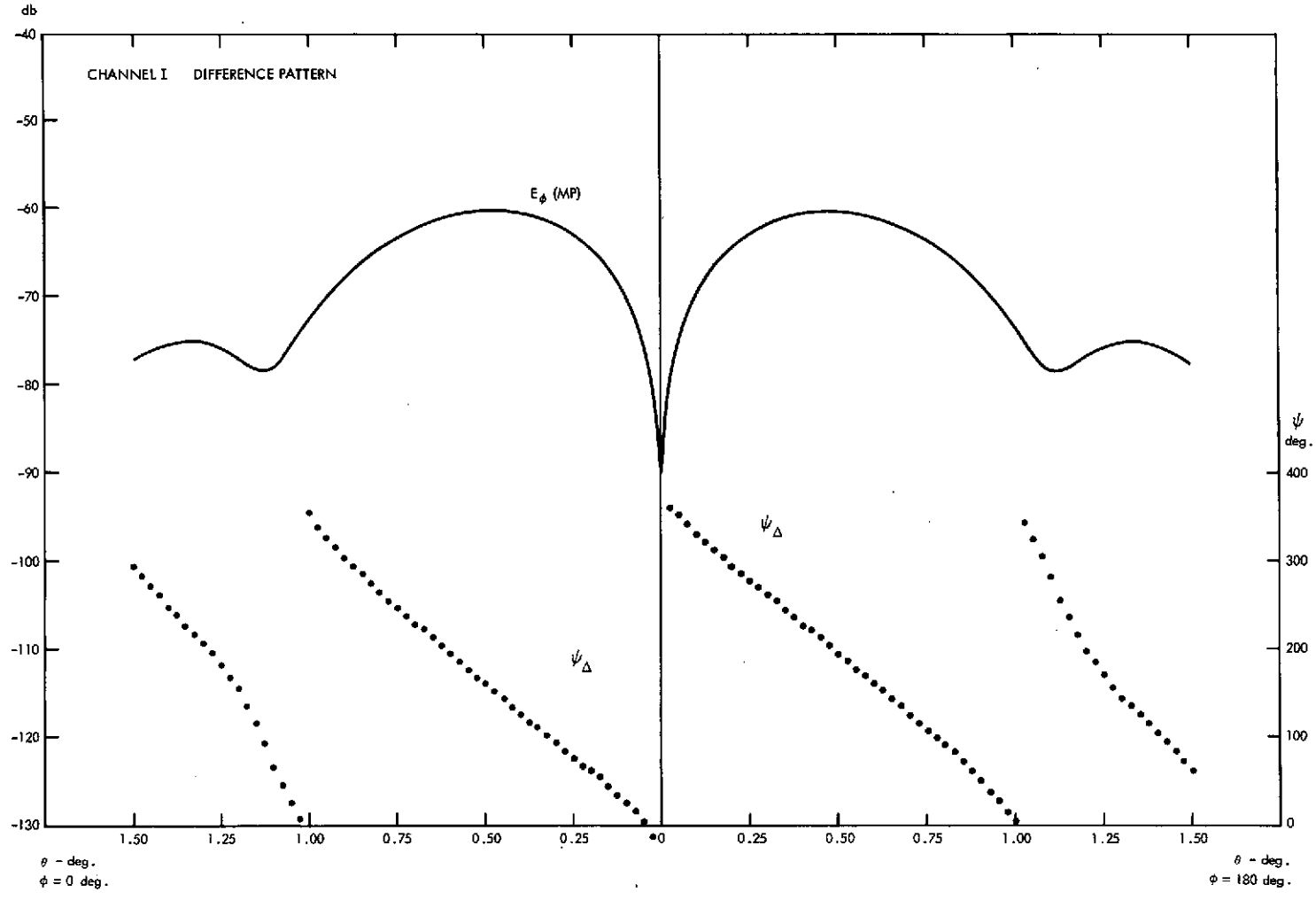

Figure 50. Acquisition pattern, Channel I (Δ) ($\phi = 0°, 180°$).

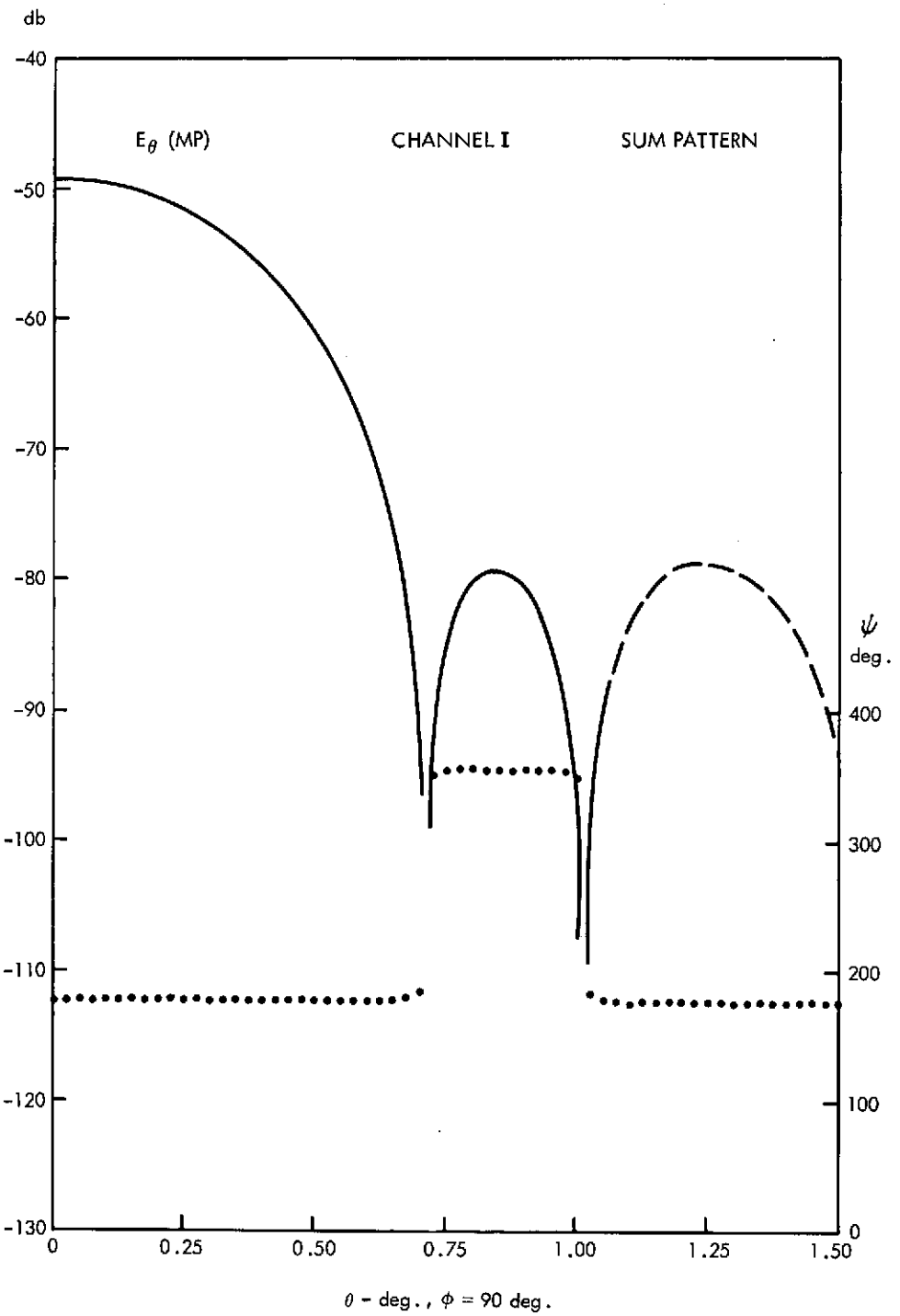

Figure 51. Acquisition pattern, Channel I (Σ) ($\phi = 90°$).

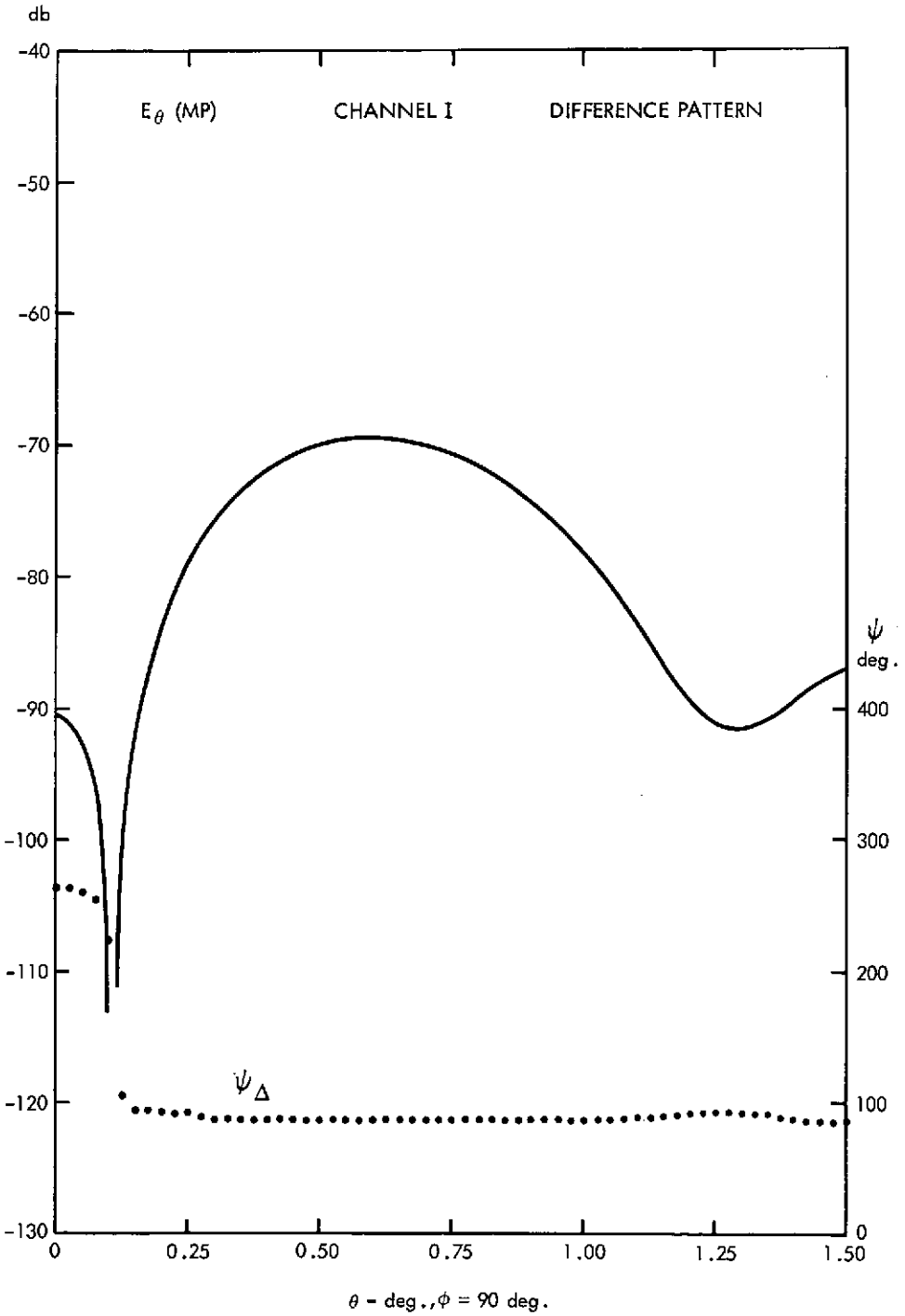

Figure 52. Acquisition pattern, Channel I (Δ) (ϕ = 90°).

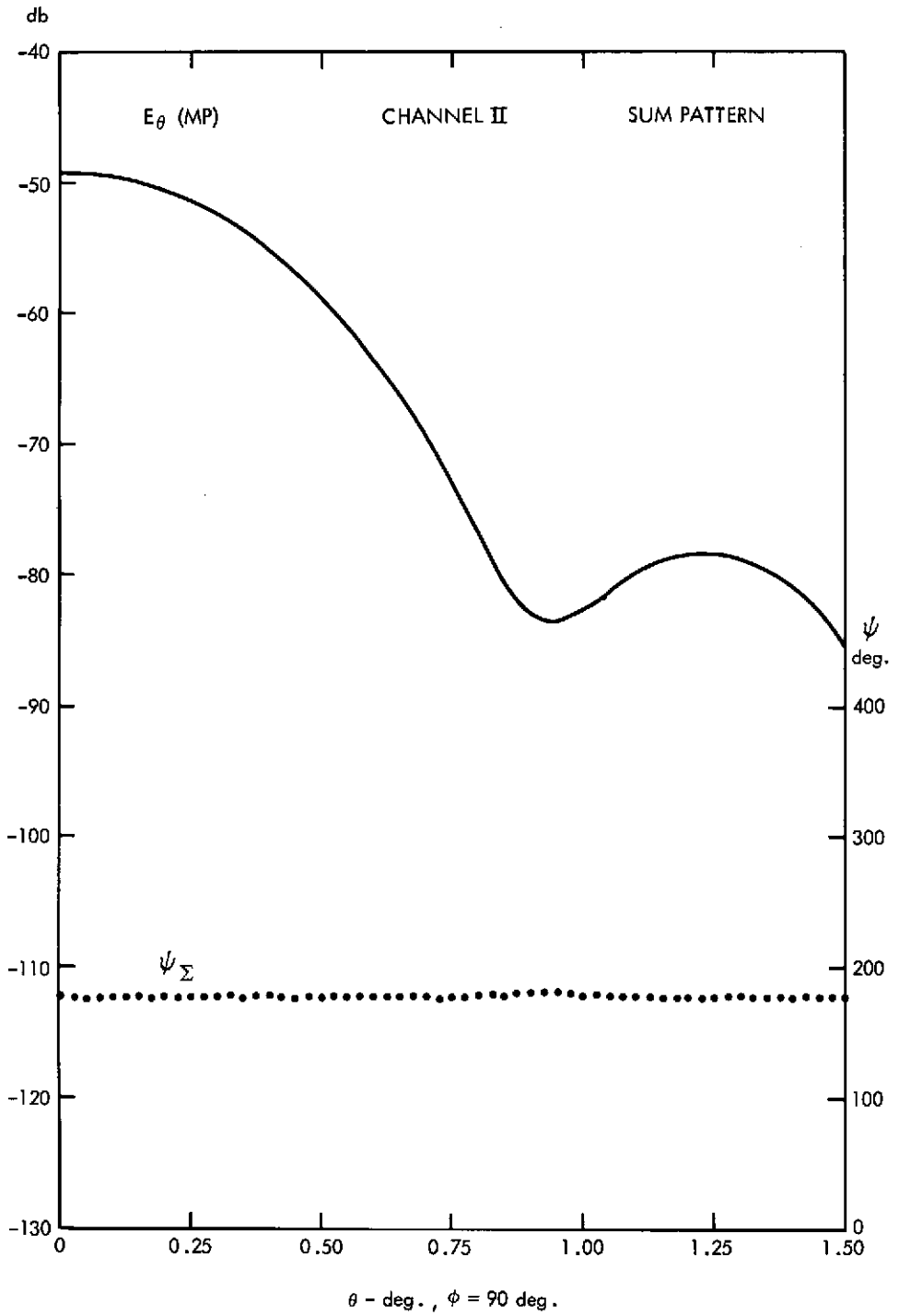

Figure 53. Acquisition pattern, Channel II (Σ) (ϕ = 90°).

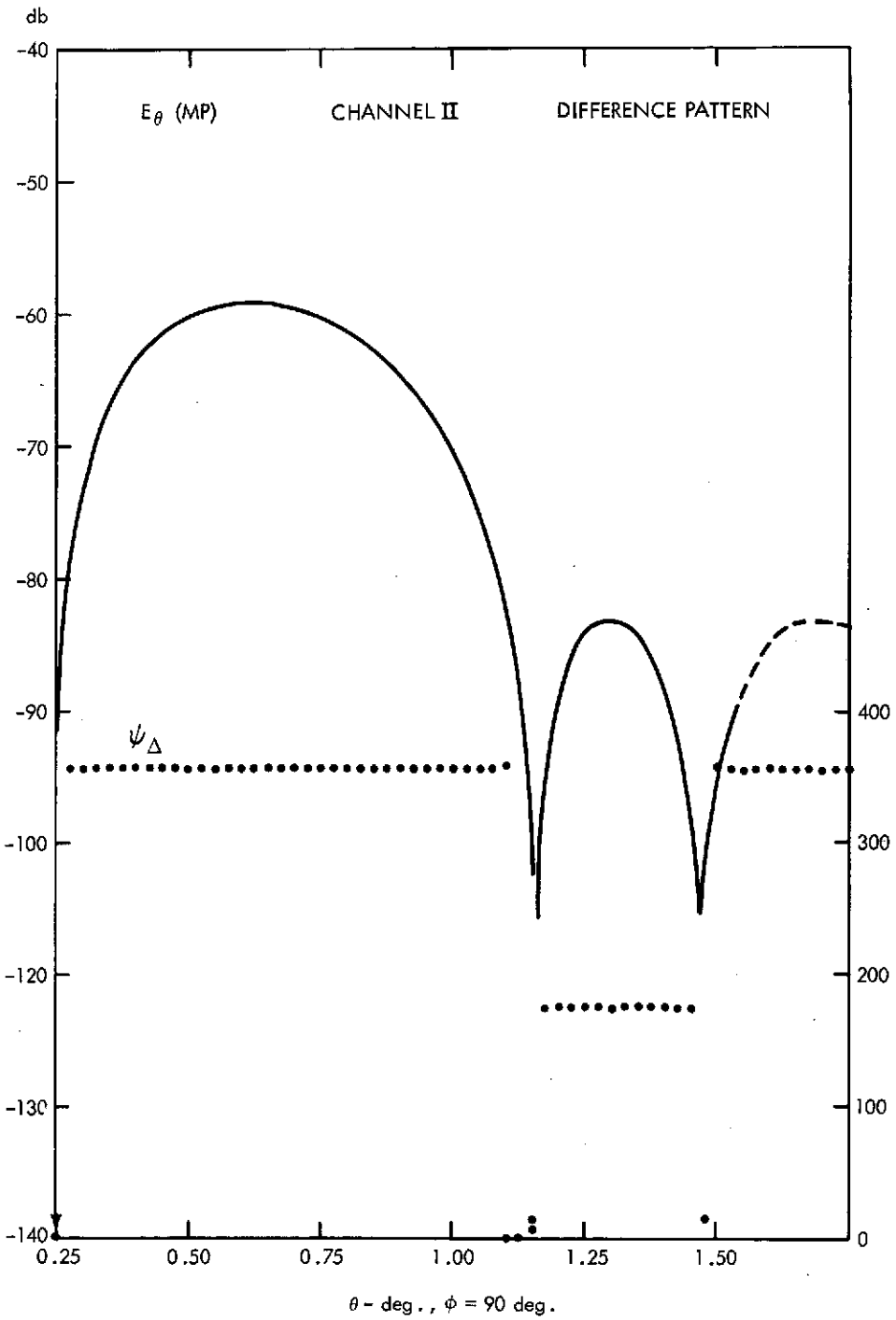

Figure 54. Acquisition pattern, Channel II (Δ) ($\phi = 90°$).

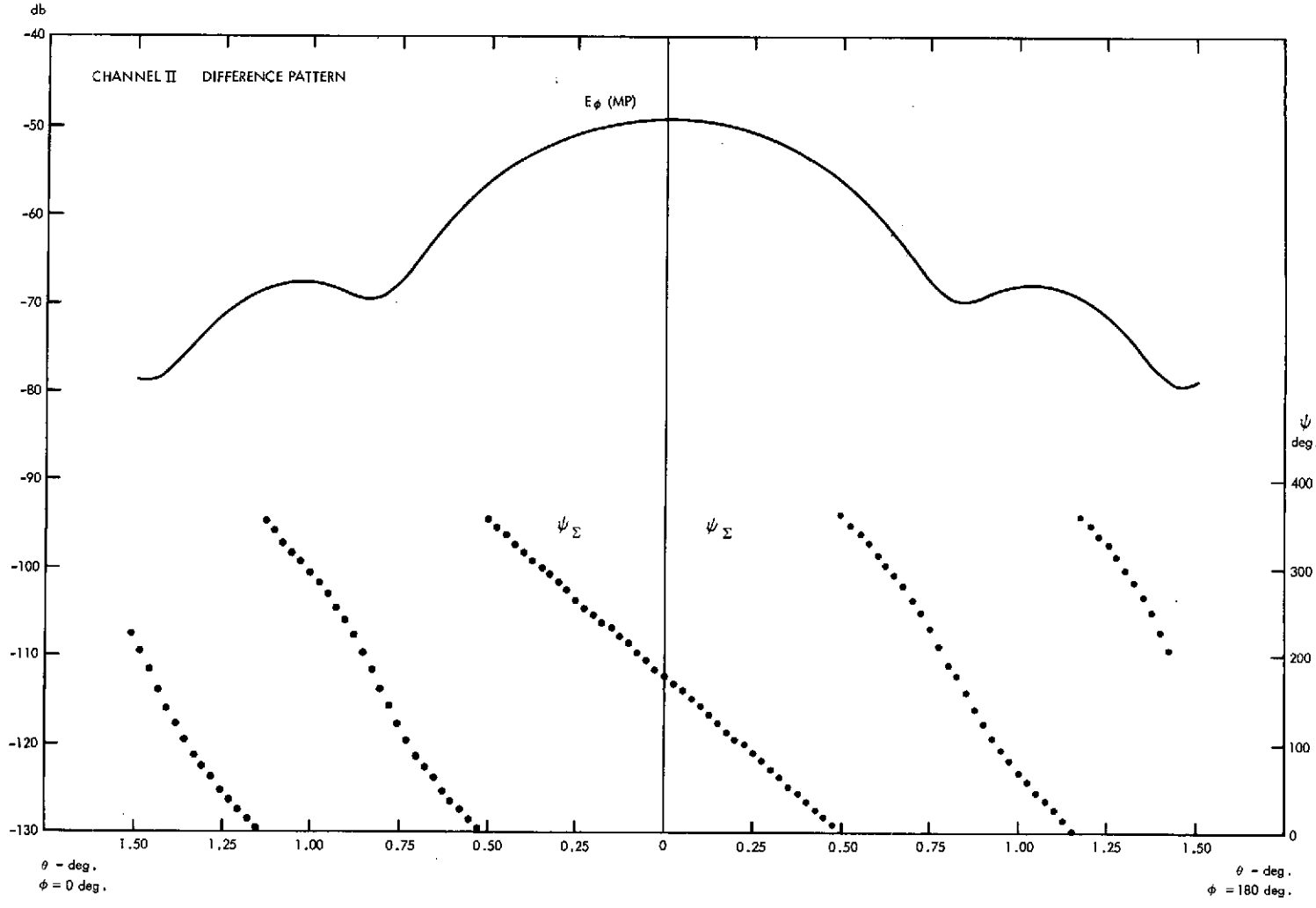

Figure 55. Acquisition pattern, Channel II (Σ) ($\phi = 0°, 180°$).

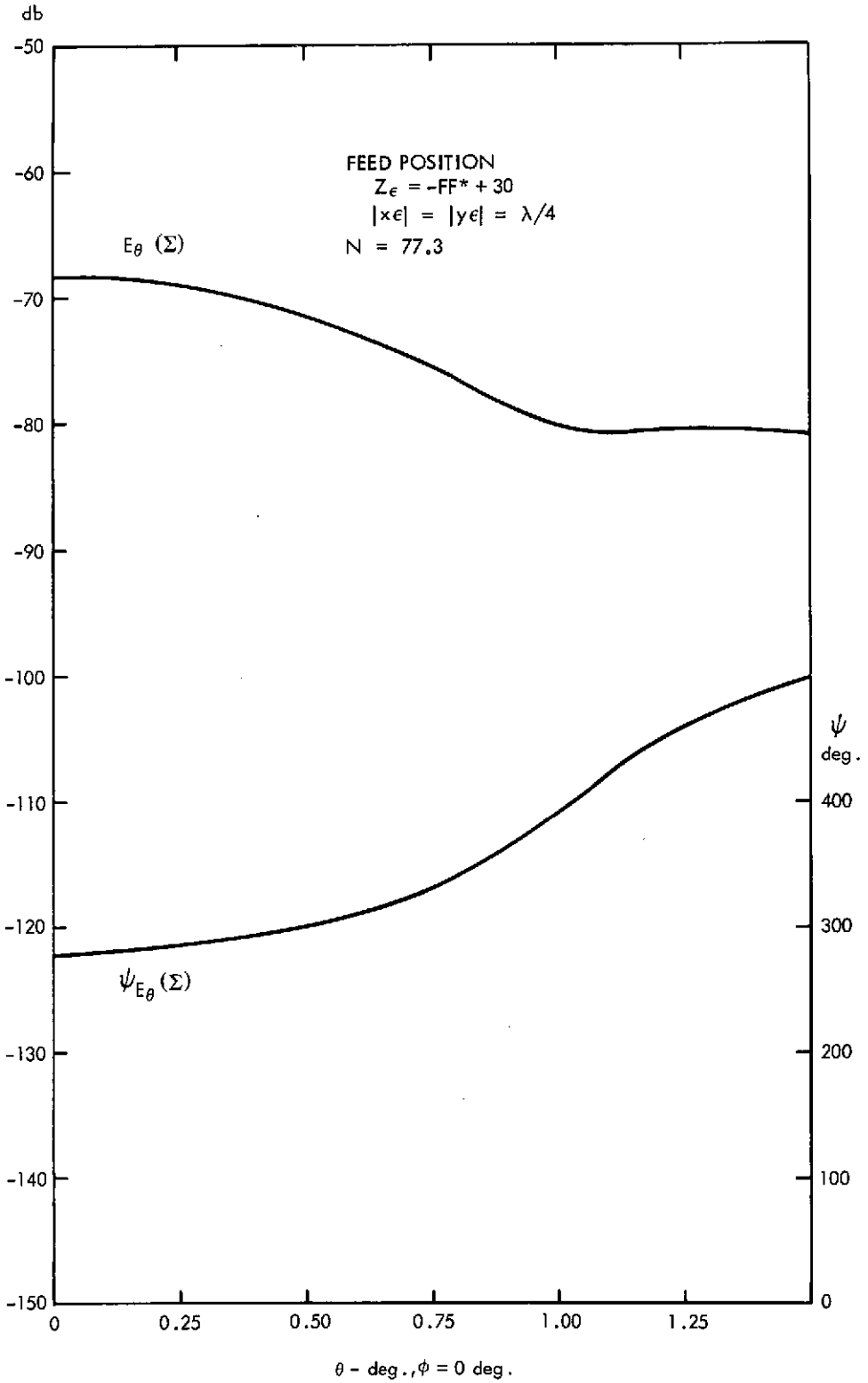

Figure 56. Acquisition pattern (Σ) of defocussed Cassegrain.

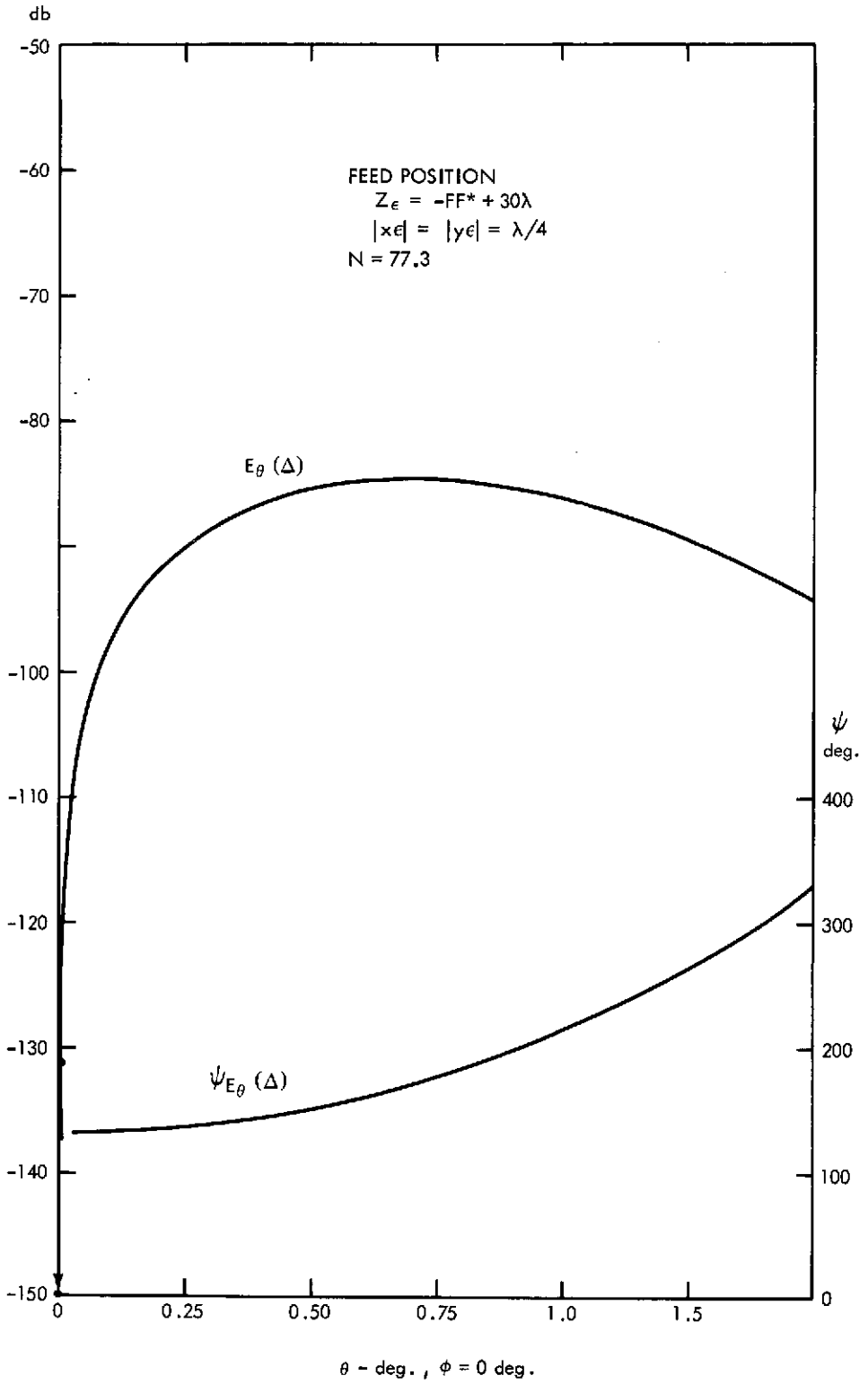

Figure 57. Acquisition pattern (Δ) of defocussed Cassegrain.

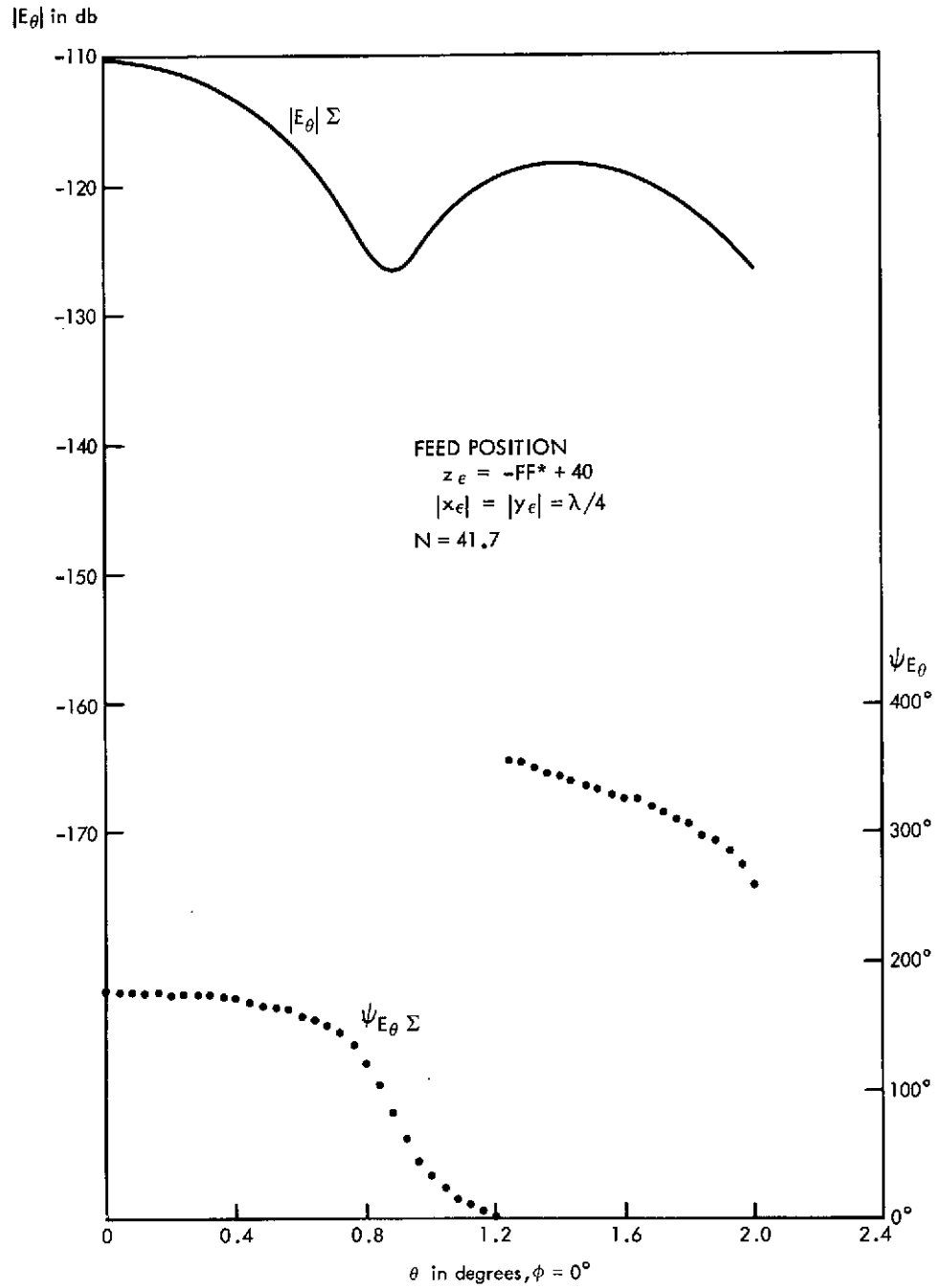

Figure 58. Acquisition pattern (Σ) of defocussed Gregorian.

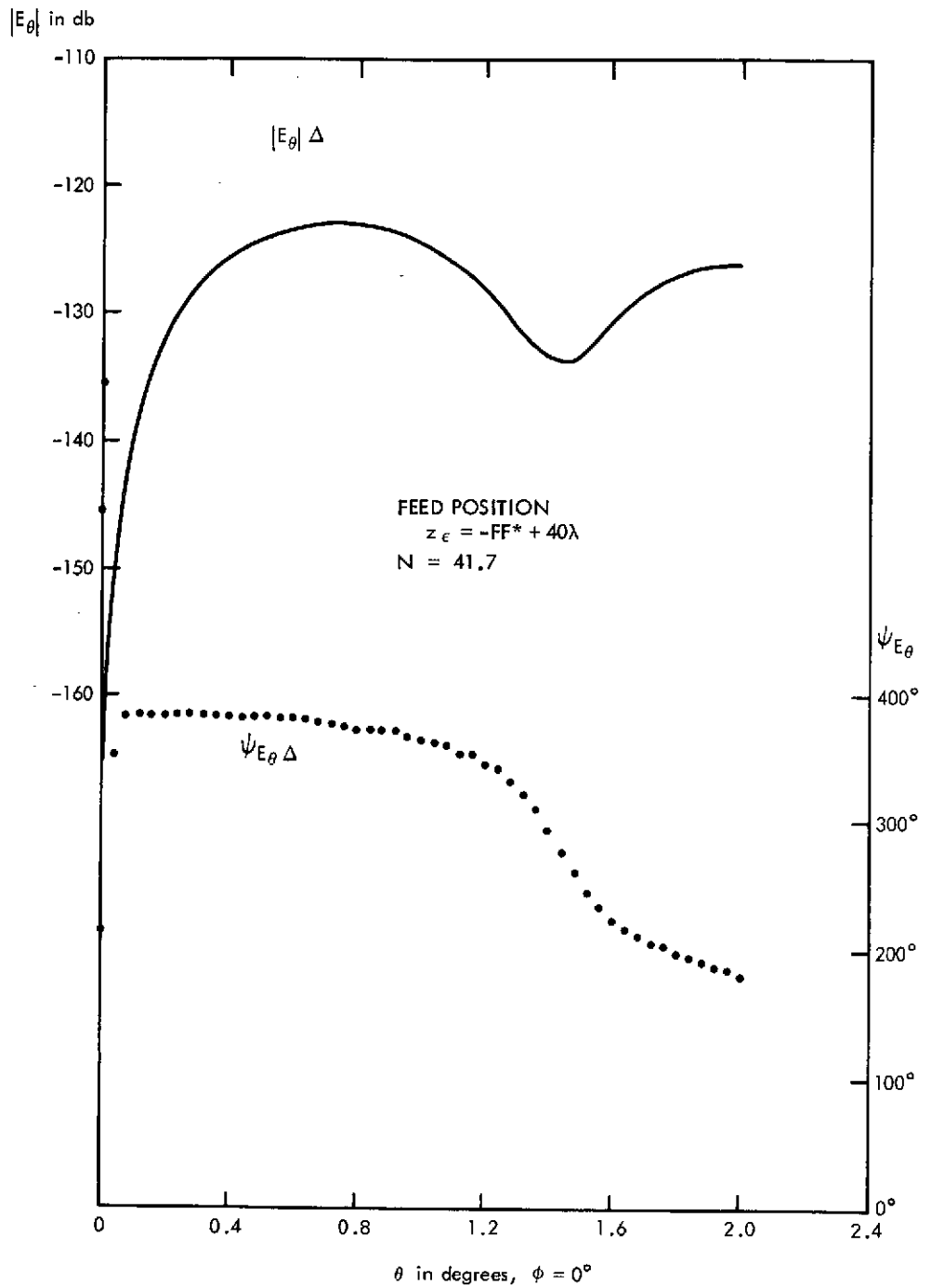

Figure 59. Acquisition pattern (Δ) of defocussed Gregorian.